DISS. ETH NO. 18145

PHOTOASSISTED ACTIVATION OF METHANE OVER SUPPORTED CATALYSTS WITH A XENON EXCIMER LAMP

A dissertation submitted to

ETH ZURICH

For the degree of

Doctor of Sciences

Presented by

François Loviat

Dipl. Chem.-Ing. ETH

born 31.05.1979

citizen of Charmoille, Jura

accepted on the recommandation of

Prof. Dr. A. Wokaun, examiner

Prof. Dr. W. J. Stark, co-examiner

Dr. J. Wambach, co-examiner

2009

Acknowledgements

The accomplishment of this work would not have been possible without the support of several people to whom I am very grateful.

First of all, I want to thank Prof. Alexander Wokaun and Dr. Jörg Wambach who accepted me as a PhD student, for their continuous help and advices during my thesis. Many thanks go to Prof. Wendelin J. Stark for his inspiring lectures and for being my co-referee.

I am also very grateful to PD Dr. Thomas Lippert for his essential support and for the numerous discussions, valuable advices, and friendly diners.

I would like to express all my gratitude to Dr. Ulrich Kogelschatz for visiting us at PSI and answering my questions about excimer lamps, Stefan Stutz for the technical support and especially for performing the HF cleaning of the lamp envelopes, Christian Dais for supervising the cleaning operations, and last but not least, Max Isler for "shaping" the raw Suprasil tubes into the lamp envelopes.

Many thanks go to Dr. Rüdiger Kötz for the spectroscopic ellipsometry measurements, Dr. Annette Foelske for introducing me to XPS, and Patrick Ruch for the AFM measurements.

I also would like to thank Prof. Christoph Renner and Dr. Henrik Rønnow for their fruitful collaboration concerning the perovskite paper.

Many thanks also go to Michael Horisberger who prepared the Al_2O_3/Si substrates, Dr. Patrick Farquet for the SEM analyses, Rolf Schelldorfer and Dr. Thomas Jung for introducing me to AFM and for their continuous support during the measurements.

I wish to thank Dr. Izabela Czekaj for the DFT calculations and Jean Wimmer, my former office mate, for having introduced me to infrared spectroscopy.

Contents

Summary

The direct and efficient conversion of methane into useful chemical products is often considered as the Holy Grail of catalytic science [1]. Methane, the principal component of natural gas, is an abundant and inexpensive resource which is a potentially interesting oil substitute. Due to its expensive and energy intensive transport and conversion, methane is at present mainly used for heating and power generation purposes. A direct gas to liquid process for the conversion of methane into valuable products would therefore be of high economical, environmental, and social importance.

A significant part of this work has been devoted to the design and characterization of tools for the study of the photoassisted activation of methane with a xenon excimer lamp over Ni-Pd/$\gamma - Al_2O_3/Si$ model catalysts. Excimer lamps are interesting for the generation of monochromatic radiation in industrial processes as they are cheap, robust, and can operate with efficiencies higher than 60%.

The catalyst substrates were prepared by depositing 10 nm of γ-Al_2O_3 on a silicon (100) wafer by magnetron sputtering. The conductivity and low surface roughness of these substrates allow the unlimited application of surface analyses techniques like AES, XPS, SE and AFM. It appeared that the interphase between Al_2O_3 and Si is not sharp but consists of 4-5 nanometers of a mixed Al/Si oxide layer. A mechanism for the formation of this oxide layer involving the diffusion of silicon atoms from the wafer into the alumina layer is discussed.

Different amounts of nickel and palladium were evaporated by physical vapor deposition at various temperatures and with different evaporation rates on the UHV cleaned substrates. The catalysts were then analyzed with AFM and XPS in order to determine experimental conditions allowing the formation of small and homogenous metallic clusters, which are

desirable for an optimum catalytic activity. A Stranski-Krastanov growth mode has been identified both for nickel and palladium over γ-Al$_2$O$_3$ within the chosen experimental conditions. Pd and Ni seem to form initially a 2 dimensional, one atom thick layer, until a critical coverage of about 0.5 average ML. Further metal deposition results in the creation of 3D clusters by surface diffusion or reconstruction processes.

A UHV xenon excimer lamp has been developed in order to investigate the effect of 172 nm photons on the activation of methane over Ni-Pd/$\gamma - Al_2O_3/Si$ model catalysts. Several issues connected to the limited space available, the high tension, and the lamp cooling had to be addressed. The lamp envelope is made of a high purity quartz called Suprasil$^®$, produced by flame-hydrolysis of SiCl$_4$. This material has the property to be transparent to VUV radiations down to 160 nm. The different operational parameters of the lamp, like the filling pressure, voltage, current frequency, and temperature have been optimized. The VUV output intensity of the lamp initially decreased during the first 6 hours of operation but remained afterwards stable at 65% of the original value. This decrease is thought to result from the formation of color centers in the quartz envelope. After this initial stabilization period, the VUV emission only needs about 2 minutes to reach a stable value upon starting of the lamp.

The final part of this work deals with the evaluation of the model catalysts reactivity and the influence of the lamp irradiation with regard to the activation of methane. Thermal programmed desorption experiments have been carried out between 300 and 773 K with CH$_4$, 95% CH$_4$/5% O$_2$, and 50% CH$_4$/50% CO$_2$ for a selection of catalyst compositions. Experiments, both with and without lamp irradiation of the catalysts surface during the temperature ramps were performed and are referred to as "bright" and "dark" experiments respectively. The carbon uptake of the catalysts surface during the reactions was measured by X-ray photoelectron spectroscopy and is considered as a reactivity indicator, as carbon originates from the decomposition of methane.

In the case of pure methane, the carbon concentration was systematically higher in the bright experiments and the difference between bright and dark increased with the nickel content of the Ni-Pd bimetallic catalysts. This experiment shows evidence of a photoassisted activation effect. It is remarkable that 172 nm photons can influence the activation of methane, which does not absorb significantly in the gas phase above 140 nm.

Auger electron spectroscopy analyses of the catalysts surface after the TPR experiments indicated a more intense Pd signal in the bimetallic samples than expected from their nominal composition. In addition, no significant difference of the nickel to palladium signal intensity ratio could be detected between samples on which palladium or nickel was deposited first. This phenomenon is interpreted to originate from the diffusion of palladium to the surface of the metal clusters resulting in the same surface structure, independent on the evaporation order of the two metals.

Contrary to experiments with pure methane, the carbon surface concentration with methane and oxygen was always lower in bright than in dark experiments. The formation of oxygen radicals resulting from the homolytic photodissociation of oxygen molecules by the VUV radiation is suggested to account for the oxidation of the carbon formed on the catalysts surface.

A very low reactivity was observed with methane and carbon dioxide. The reason for this behavior could not be identified precisely. The catalysts surface was not oxidized during these experiments and no traces of carbonate formation which could block the active sites was detected.

The formation of reaction products was followed during the temperature ramps with a mass spectrometer operated in multiple ion detection mode (MID). The main species produced from pure methane were hydrogen, C2 and C3 hydrocarbons. The intensity of the QMS signals corresponding to these products was systematically higher for the bright experiments but the large error bars involved in these measurements must be considered in the interpretation of the results.

In the case of methane and oxygen, the main products detected were CO, CO_2, H_2O, H_2, and C2 hydrocarbons. The relative signal intensity and oxidation level of nickel and palladium after the TPR experiments support the suggested diffusion of palladium to the surface of the metal particles. In addition, the palladium rich "shell" surrounding the metal clusters seems to protect the particles against total oxidation.

Version abrégée

La recherche d'un procédé direct à rendement élevé permettant de convertir du méthane en hydrocarbures liquides sans passer par l'intermédiaire du gaz de synthèse est souvent considérée comme le Graal de la catalyse moderne [1]. Le gaz naturel, constitué de 80% à 90% de méthane, est une ressource abondante et bon marché qui représente une alternative au pétrole potentiellement intéressante. Cependant, le transport du gaz naturel engendre de massive émissions de gaz à effet de serre, sous forme de dioxyde de carbone mais également de méthane qui possède un potentiel de réchauffement 20-25 fois supérieur à celui du CO_2. De plus, en raison du coût énergétique et financier considérable que représente la conversion du méthane en d'autres produits chimiques par l'intermédiaire du gaz de synthèse, le gaz naturel n'est actuellement utilisé qu'en tant que combustible de chauffage ou pour la production d'énergie. Un procédé en une étape permettant de transformer le méthane en hydrocarbures supérieurs aurait par conséquent un impact économique, environnemental et social conséquent.

Une partie importante de cette thèse est dédiée à la conception ainsi qu'à la caractérisation d'instruments et de techniques permettant l'étude de l'activation photoassistée du méthane au moyen d'une lampe à excimères au xénon sur des catalyseurs bimétalliques modèles de type Ni-Pd/$\gamma - Al_2O_3/Si$. Les lampes à excimères constituent une source de rayonnement monochromatique attractive dans les procédés industriels du fait de leur faible coût, de leur robustesse ainsi que de leur rendement pouvant dépasser 60%.

Les substrats servant de base pour la préparation des catalyseurs utilisés dans ce travail ont été élaborés par pulvérisation cathodique magnétron de 10 nm d'alumine gamma sur des tranches de silicium d'orientation cristalline (100). La surface de ces substrats a ensuite été nettoyée par bombardement ionique d'argon et recuit thermique sous oxygène

dans une chambre à ultra haut vide (UHV). La conductivité électrique ainsi que la très faible rugosité de la suface de ces substrats permettent l'application illimitée de techniques d'analyse de surface comme la spectroscopie des électrons Auger (AES), la spectroscopie de photoélectrons X (XPS), l'ellipsométrie spectroscopique (SE) ainsi que la microscopie à force atomique (AFM). Ces differentes techniques ont permis de révéler que l'interface entre la couche d'alumine et la tranche de silicium n'est pas clairement délimitée mais diffuse et constituée d'une zone de 4-5 nm d'épaisseur d'un oxyde mixte à base de silicate et d'alumine. Un mécanisme expliquant la formation de cette couche d'oxyde mixte basé sur la diffusion d'atomes de silicium dans l'alumine est décrit dans ce travail.

Des quantités variables de nickel et de palladium ont été déposées sur d'alumine gamma par dépôt physique en phase vapeur à différentes températures et vitesses de déposition. Les catalyseurs ainsi préparés ont ensuite été analysés par AFM et XPS, de manière à identifier des conditions expérimentales propices à la formation de nano-clusters métalliques homogènes, gages d'une activité catalytiques optimale. Ces analyses ont permis de mettre en évidence un mode de croissance de type "Stranski-Krastanov" aussi bien dans le cas du palladium que du nickel sur de l'alumine gamma dans les conditions expérimentales sélectionnées. Ni et Pd semblent initialement former une structure bidimensionnelle d'épaisseur monoatomique jusqu'à un recouvrement critique du substrat d'environ 0.5 ML, après quoi on assiste à la création de clusters tridimensionnels résultant de phénomènes de diffusion ou d'une reconstruction de la surface du catalyseur.

Une lampe à excimères au xénon compatible avec une utilisation sous ultra haut vide a été conçue dans le cadre de ce travail dans le but d'étudier l'influence de photons ayant une longueur d'onde de 172 nm face à l'activation du méthane sur des catalyseurs modèles Ni-Pd/$\gamma - Al_2O_3/Si$. Des solutions techniques liées à l'utilisation de hautes tensions (1000-10'000 volts) ainsi qu'à la nécessité d'un refroidissement efficace dans un espace très restreint et sous vide ont été développées. L'enveloppe de la lampe à excimères contenant le xénon est constituée d'un quartz de haute pureté commercialisé sous l'appellation Suprasil®et obtenu à partir de l'hydrolyse à la flamme de tétrachlorure de silicium ($SiCl_4$). Ce matériau est caractérisé par une longueur d'onde de coupure située à 160 nm.

Les paramètres opérationnels de la lampe comme la pression de remplissage de l'enveloppe de quartz, la tension, la fréquence du courant ainsi que la température d'utilisation ont été optimisés.

Dans un premier temps, l'intensité du rayonnement émis a diminué durant les 6 premières heures d'utilisation mais s'est stabilisée par la suite à 65% de la valeur nominale. Ce déclin est supposé provenir de la formation de centres colorés dans l'enveloppe de quartz, absorbant une partie des radiations émises. Après cette période initiale de stabilisation, l'intensité du rayonnement émis se stabilise dans les 2 minutes suivant l'allumage de la lampe.

La partie finale de cette thèse traite l'évaluation de l'activité des catalyseurs bimétalliques préparés ainsi que l'influence des radiations produites par la lampe à excimères sur l'activation du méthane. Pour cela, des réactions en température programmée ont été conduites sur des catalyseurs de compositions différentes dans le cas de trois mélanges gazeux distincts: 100% CH_4, 95% CH_4/5% O_2 et 50% CH_4/50% CO_2. Les rampes de température ont été effectuées dans un premier temps sans irradiation de la surface des catalyseurs par la lampe à excimères et dans un deuxième temps avec exposition aux rayonnements VUV. La quantité de carbone accumulée par le catalyseur durant les réactions à été déterminée par spectroscopie de photoélectrons X et considérée comme un indicateur de réactivité puisque le carbone formé résulte de la décomposition de méthane.

L'accumulation de carbone dans le cas des réactions avec du méthane pure s'est révélée être systématiquement supérieure lors de l'irradiation de la surface des catalyseurs par la lampe à excimères. Cette observation suggère l'existence d'un mécanisme d'activation photoassisté. Il est remarquable que des photons de 172 nm puissent influencer l'activation du méthane puisque ce dernier n'absorbe pas de manière significative les rayonnements supérieurs à 140 nm en phase gazeuse.

L'analyse post réactionnelle par spectroscopie d'électrons Auger de la surface des catalyseurs bimétalliques à révélée une concentration apparente de palladium supérieure à la composition nominale des catalyseurs. De plus, aucune différence significative de concentration entre les catalyseurs de même composition mais se différenciant par l'ordre de déposition des différents métaux n'a pu être mise en évidence. Ce phénomène est interprété comme résultant de la ségrégation du palladium à la surface des clusters métalliques formant ainsi

en une composition de surface indépendante de l'ordre de déposition des différents métaux. A l'inverse des expériences impliquant du méthane pure, l'accumulation de carbone à la surface des catalyseurs dans le cas du mélange gazeux 95% CH_4/5% O_2 est apparue clairement inférieure lors de l'utilisation de la lampe à excimères. La génération de radicaux provenant de la dissociation homolytique des molécules d'oxygènes induite par le rayonnement émis par la lampe est soupçonnée être à l'origine de l'oxydation des dépôts de carbone formés à la surface des catalyseurs.

Une réactivité quasi nulle à été observée dans le cas du mélange 50% CH_4/50% CO_2 sans que la cause ne puisse être clairement identifiée. Aucune trace d'oxydation du catalyseur ni de formation de carbonate susceptible de bloquer les sites actifs n'ont pu être mis en évidence.

La formation de produits de réaction à été détectée au moyen d'un spectromètre de masse quadripolaire (QMS) en mode de détection d'ions multiples (MID). Les principales espèces détectées dans le cas du méthane sont de l'hydrogène et des hydrocarbures C2 et C3. Les intensités des signaux correspondants à ces produits sont apparues systématiquement supérieures lors des expériences incluant l'utilisation de la lampe à excimères. Cependant, les mesures effectuées comportent des marges d'erreurs importantes dues à une faible reproductibilité des expériences.

Dans le cas du méthane et de l'oxygène, les principaux produits détectés sont du monoxyde et dioxyde de carbone, de l'eau, de l'hydrogène ainsi que des hydrocarbures de type C2. L'analyse post réactionnelle du niveau d'oxydation ainsi que de l'intensité relative du nickel et du palladium dans les catalyseurs bimétalliques soutient l'hypothèse d'une diffusion du palladium à la surface des particules métalliques. De plus, la coquille riche en palladium entourant les clusters constituant le catalyseur semble prévenir une oxydation totale durant les réactions.

Chapter 1

Introduction

1.1 Methane as a source of energy

Ever since our distant ancestors managed to light fire for their daily life requirements, the development of mankind has always been tightly bound to the utilization of energy. Initially devoted to survival purposes, the energy needs have been limited for a long time. When some 200 years ago man understood how to actuate machines by chemical energy and the benefits he could draw from that, the beginning of a dramatic revolution was initiated. Due to its higher energy density, coal supplanted wood and was very fast followed by oil and gas. Since then, the whole society has thrived using energy resources which are not renewable on the human time scale. These resources, called fossil fuels are remnants from millions of years of organic materials accumulation, settled in large quantities in the sea bottom under anoxic conditions. The tremendous increase of the thirst for energy which is necessary for the growth of our society, connected to the depletion of non-renewable energy sources has led to an unpreceded rush for new resources. In order to sustain the standard of living to which the industrialized world is now accustomed and to which developing countries are aiming, new solutions will have to be found to achieve a smooth transition towards renewable energy sources.

Natural gas is an interesting source of energy on many aspects. It is a very potent resource as it yields a larger amount of energy per CO_2 molecule released than any other fossil fuel, due the low C:H ratio of CH_4 molecules. Even if most of the actual production

originates from geological deposits, methane can also be produced by the fermentation of all kind of organic wastes, under which condition it constitutes a renewable resource. Connected to the fact that methane is a very potent greenhouse gas and is emitted by many anthropological activities, like mining or agriculture, its valorization could lead to the profitable exploitation of some emission sources. However, the main advantage of methane is probably its abundance. As a matter of fact, it is the main component of natural gas, for which the proven reserves amounted 180 trillion cubic meters in 2007 [2]. At the consumption rate corresponding to year 2007, these reserves should last close to 70 years. In addition tremendous amounts of methane are "stored" in ice like solids called hydrates in which the gas molecules are trapped in water cages. These hydrates, or more specifically *clathrates*, can be found worldwide in oceanic sediments or in the permafrost of arctic regions in a depth ranging from 150 to 2000 meters. The exact size of these deposits is still debated and estimations may vary by as much as three orders of magnitude but average values at the present time are in the order of 21'000 trillion of cubic meters, that is roughly 100 times more than the proven gas reserves [3]. However, significant technical issues will have to be solved in order to make methane hydrate resources exploitable. As a matter of fact, there is currently no commercial production of natural gas from hydrates with the possible exception of the Messoyakha gas field in Siberia, where some gas is thought to originate from methane hydrates [4]. Various technologies are presently tested for the extraction of methane, like depressurization, injection of steam, hot water or inhibitors aiming at sublimating the hydrates but none of these techniques has shown commercially profitable yet. In addition, the risk of destabilizing hydrates fields which could trigger the uncontrolled release of huge volume of gas constitutes also a significant hazard. It remains that the reserves are so enormous that even the exploitation of only few percent of the total stored hydrates could provide energy for many generations.

1.2   Environmental impact of methane

In recent years, methane emissions have become a major environmental concern mainly because of its implication in the greenhouse effect [5]. The concentration of methane in the atmosphere increased from 0.7 ppm in 1745 by 250% to reach 1.75 ppm in 2008. It seems

however to stabilize since the end of the 1990s [6]. The global warming potential (GWP) of CH_4 is 20-25 times higher than the one of CO_2 and because of that, it contributes for about 20% to the greenhouse effect in spite of its much lower atmospheric concentration compared to carbon dioxide [7].

Atmospheric methane originates from a variety of sources which can in principle be classified into two categories; anthropogenic and natural sources which account respectively for 60% and 40% of the total emissions. Natural related sources include wetland, gas hydrates, permafrost, termites and oceans. All together, these sources account for about 250 million metric tons of CH_4 every year and are very dependent on environmental factors like temperature and precipitations. The exact contribution of each source to the total natural methane emissions is still relatively uncertain, but literature data allow some estimations shown in figure 1.1 [7]. Wetlands are responsible for the major part of natural methane
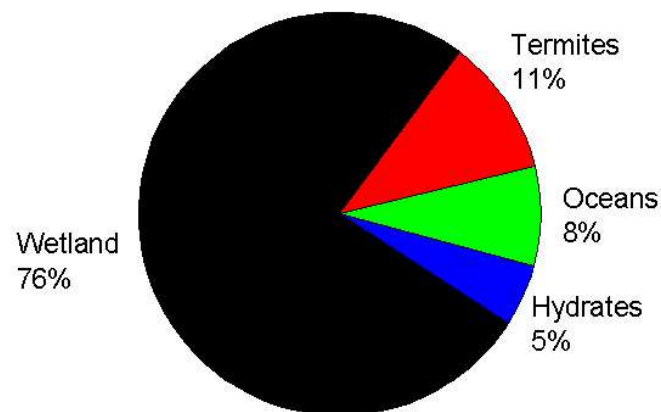
Figure 1.1: Relative contribution of different methane natural emission sources [7].

emissions. They provide an ideal habitat to methanogenic bacteria which produce CH_4 from the decomposition of organic materials. Termites contribute at a level of 11% through their normal digestion process. Oceans are thought to be responsible for 8% of the global natural emissions but the exact origin of methane is not entirely clear yet. Two potential sources are the digestion of zooplankton and the methanogenesis in sediments and drainage areas along coastal regions. Finally, the contribution of methane hydrates is estimated to

be around 5%. Under defined conditions of temperature and pressure, natural gas can form methane hydrates but may also be released from these hydrates due to temperature, pressure or salt concentration changes. It is believed that earthquakes and volcanic eruptions can also lead to a destabilization of marine deposits and therefore to a sudden liberation of tremendous amounts of natural gas. This phenomenon has been suggested to explain rapid global warming events in the past, such as the Paleocene–Eocene Thermal Maximum of 55 million years ago [8]. Some theories suggest that methane hydrates may be responsible for the well known reputation of the Bermuda triangle. As a matter of fact, large methane hydrates fields are present in the ocean floor of this area. It has been hypothesized that periodic methane eruptions (sometimes called "mud volcanoes") may generate regions of frothy water with the consequence of reducing locally the density of water below the buoyancy threshold of ships. Such a phenomenon which would result in the rapid and unexpected sink of vessels have been shown to be realistic by experiments on scale ships in Australia [9].

A theory called the "clathrate gun hypothesis" predicts that a rise in sea bed temperatures could destabilize hydrate deposits and trigger a sudden release of natural gas. The methane emitted could provoke, due to its important greenhouse effect, a further temperature rise and in turn other methane releases, resulting in a "runaway" process heating the earth to unpreceded levels [10]. Less dramatic but already observed is the increase of CH_4 emissions from the arctic region as the permafrost melts. No later than in September 2008, researchers have found evidence that massive deposits of natural gas were bubbling from the seafloor along the Russian northern coasts. Concentrations up to 100 times higher than the background levels have been measured over the sea [11]. The relative contribution from natural sources is therefore expected to increase in the upcoming years.

Anthropogenic sources include the ruminants digestion, agriculture (rice production), production and distribution of gas, decomposition of wastes in landfills, burning of biomass and production of coal [12]. As can be seen in figure 1.2, almost half of the anthropogenic methane results from agricultural activities. In the case of the production of rice, methane originates from anaerobic fermentation in the soil and is mainly transported to the atmosphere by the plant itself via diffusion processes [13]. Rice paddies are ideal for the production of methane as they contain a high level of organic substrates in oxygen de-
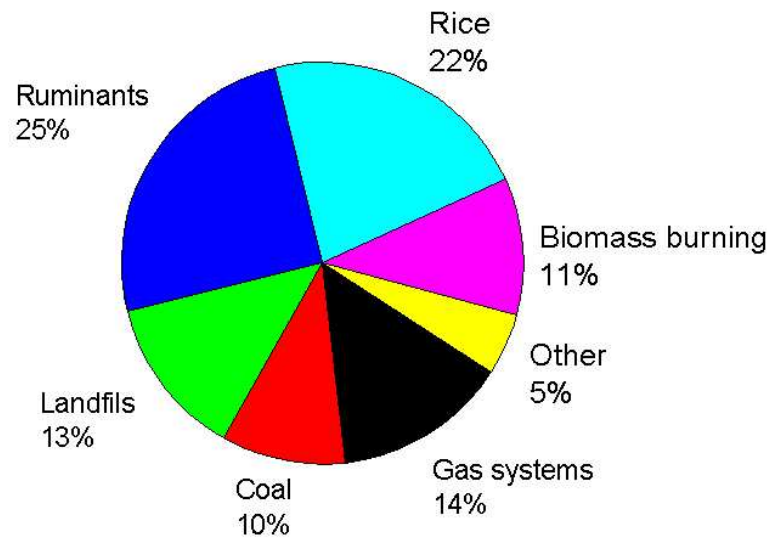
Figure 1.2: Relative contribution of different methane anthropogenic sources [7].

pleted conditions. Ruminants contribution originates from their normal digestion process, making use of microbial fermentation called "enteric fermentation". The contribution of landfills is also significant and ensues from the decomposition of waste under anaerobic conditions. Methane emissions arising from biomass burning are a consequence of incomplete combustion and huge amounts can be produced during large scale burning of woodlands, savanna, and agricultural waste. The last fourth of anthropogenic emissions concerns the production of energy. Coal mining for example releases the methane trapped in the coal deposits during extraction and further handling. Finally, the production of natural gas is also an important methane source which is however difficult to estimate. Losses occur during the production, processing and distribution activities. As a matter of fact, natural gas is transported at a typical pressure of 75 bars over large distance and crosses therefore thousands of valves and connections [14]. The main leaks are thought to occur in compression stations, valve knots and machine halls [15]. Many studies have been carried out in order to determine the importance of this source and it seems that the leak rate depends on the distribution system considered. The transport losses in the United States are estimated at about 1.5±0.5% [16] while values between 1.4 and 10% [17] are suggested for the Russian grid which is older and for which less reliable information is available.

An average leak rate of 1.5% with regard to the 2200 million tons produced in 2007 [2] would correspond to about 10% of the total anthropogenic emissions.

1.3 Activation of methane

Initially considered as an undesirable by-product of petroleum production, natural gas was and is still in some cases, simply flared at oil rigs [18], resulting in an important waste of hydrocarbon. However, after the oil crises of the 1970s and the recent rise of oil prices, many gas resources especially off-shore, until now considered as not economically viable because of logistical difficulties and gas transportation costs, have been revisited. Transporting natural gas by pipeline is relatively easy. Pipelines are however not suitable for the transport of gas from remote locations like off shore platform or from Southern Arabia to Europe or the United States. For intercontinental transportation, natural gas has to be liquefied (LNG). This process is very energy intensive and necessitates special and expensive equipments like tankers able to maintain natural gas below its boiling point (-163 ºC) in double wall, well insulated spherical or cylindrical tanks made of high nickel-steel. The energy needed for the transportation process of LNG including compression, refrigeration, liquefaction, re-gasification and purification is equivalent to an important fraction of the energy contained in the originally produced methane [19]. In order to efficiently use the large gas reserves available, a conversion to liquid fuels is unavoidable.

Different options are considered here but the conversion of methane to methanol is often thought to be one of the most interesting. Methanol has the great advantage to be liquid under normal conditions. It can therefore be stored and transported easily with the existing gasoline grid. It has twice the energy density of liquid hydrogen and can be used in conventional combustion engines without major modifications and also in fuel cells. Fuel cells constitute in fact a convenient and efficient way of producing electric power. An additional advantage of methanol is that it can be catalytically converted to ethylene, propylene and a wide range of other chemical products which constitute very important feedstocks for the chemical industry. These feedstocks are presently obtained from the diminishing oil reserves.

Dimethyl ether (DME) is also often mentioned as a promising alternative as transportation fuel or for gas turbines [20]. It could be used as diesel fuel and provides, like methanol, a clean combustion which is free of soot and SO_2. DME has a higher specific energy content than methanol, is non toxic and environment friendly. It is widely used today as an aerosol propellant for spray cans but is also an important chemical feedstock for the production of dimethyl sulfate which is a methylating agent, in the Montsanto process for the production of acetic acid [21]. Beside methanol and DME, a wide range of other industrial chemicals would also be desirable, as for instance ethanol, acetic acid or formaldehyde.

In 2007, the world natural gas consumption was distributed as shown in figure 1.3. The amount of gas included in the industrial share, used for the production of chemicals was lower than 3%. Half of this value is dedicated to fertilizers and the rest includes basic or-
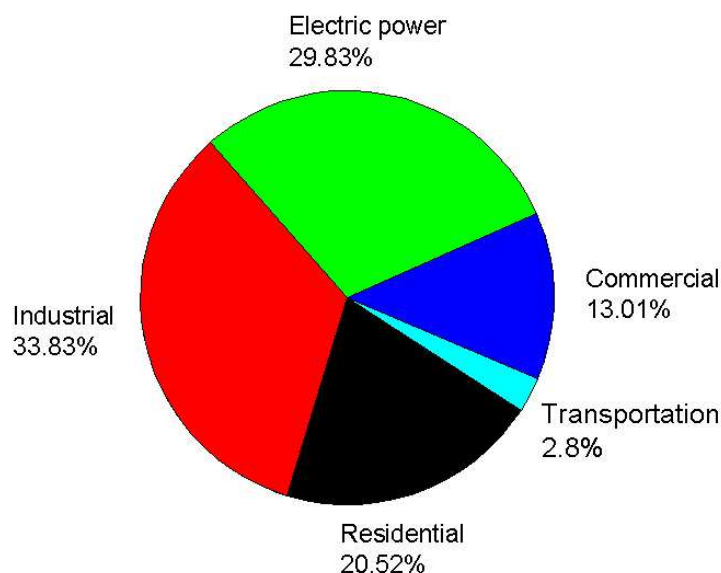
Figure 1.3: Relative usage of natural gas in 2007 [22].

ganic chemicals, polymers and liquid fuels. This means that more than 97% of the natural gas produced is used for heating or electricity production.

The large scale production of chemicals derived from methane today, like hydrogen, methanol or acetic acid requires the initial conversion of methane into synthesis gas. This step is usually carried out by the steam reforming of methane (SRM) taking place at moderate

pressure (15-30 bar) and high temperature (1000-1200 K) on nickel based catalysts:

$$CH_4 + H_2O \rightleftharpoons CO + 3H_2 \quad \Delta H_{298K}\text{=+206 kJ/mol} \tag{1.1}$$
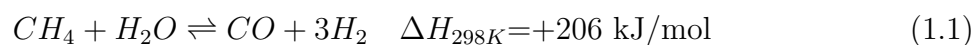
Reaction 1.1 proceeds with a good conversion ($\approx$90%) but is energy intensive. Methane can also undergo partial oxidation with molecular oxygen to produce syngas:

$$2CH_4 + O_2 \rightleftharpoons 2CO + 4H_2 \quad \Delta H_{298K}\text{=-519 kJ/mol} \tag{1.2}$$

Reaction 1.2 is highly exothermic and can be carried out in situ to produce the heat required to drive the SRM reaction. When both reactions 1.1 and 1.2 are combined, the process is called "autothermal reforming of methane". Furthermore, the ratio of CO and H_2 can be adjusted by the water gas shift reaction to provide the CO/H_2 ratio adequate for the envisaged process.

$$CO + H_2O \rightleftharpoons CO_2 + H_2 \quad \Delta H_{298K}\text{=-41 kJ/mol} \tag{1.3}$$
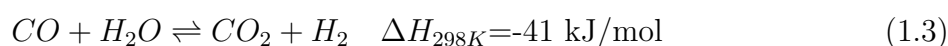
Steam reforming is highly capital-intensive in the "syngas route" processes as it involves extensive heat transfers consequently to the almost total oxidation of methane required for the production of syngas. As a matter of fact, the syngas production accounts for about 70% of the total investment and operating costs in the synthesis of methanol based on natural gas [23]. This fact is also true for the Fisher Tropsch synthesis which additionally results in a complex hydrocarbon mixture. Fossil energy ratios, defined as the ratio of the energy contained in the final product to the total energy invested in the process have been evaluated to 0.39-0.44 for methanol or F-T products derived from methane [24]. The production of liquid fuel from natural gas is therefore only economically feasible if the price of oil is high. Some studies concluded that in order to be profitable, gas to liquid processes (GTL) need a crude oil price above \$45/b together with a gas price below \$2/mmbtu. Such studies are however only based on economical aspects and disregard the environmental impacts of such processes. The syngas route can therefore hardly be seen as a future technology and the consideration of the economic stakes involved definitely provides a substantial incentive for developing new and more efficient alternative processes. One interesting approach would be to convert natural gas directly to gasoline or hydrocarbon products, avoiding the traditional syngas route. Such a process, carried out at the very

site where methane is available would offer several advantages as for instance an easier, safer and more efficient transportation. The main hindrance of a direct conversion process relies in the refractory nature of methane itself. Methane is the simplest hydrocarbon and its coupling or conversion into more complex products necessitates the splitting of a C-H bond. This step or *activation* is hindered by the closed shell structure of the methane molecule requiring a large activation energy to proceed, which necessitates harsh reaction conditions. The activation is usually considered as the limiting step in the reaction of methane [25], as for example for the production of syngas. As shown in figure 1.4, methane is more stable than any other hydrocarbons up to a temperature of 1303 K [26]. For this
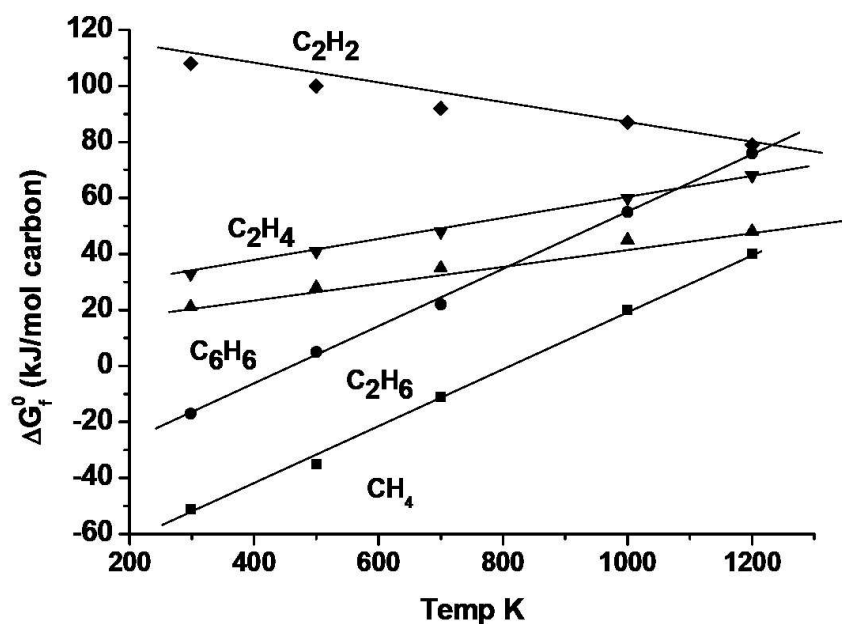
Figure 1.4: Gibbs free energy of formation for various hydrocarbons as a function of temperature [27][28].

reason, the direct conversion of methane into heavier hydrocarbons is a great challenge and has been extensively studied in the past. Several processes have been suggested like the direct oxidation by air or N_2O to C1 oxygenates [29][30], the oxidative coupling to ethane and ethylene [31][32], the enzymatic production of methanol and formaldehyde [33], the methyl bromide process resulting in C3-C7 hydrocarbons [34] or the activation of methane by Marshall's acid [35] and NO_2 [36] yielding various oxygenated hydrocarbons. Although

promising, none of these direct processes have reached a commercial stage yet. Conversions are usually too low and/or selectivities too bad for these processes to be operated in single pass mode, requiring high recycling or complex and expensive separation.

It has been reported recently that methane could be activated photochemically on metal surfaces. In the gas phase, methane requires VUV photons below 140 nm to dissociate the C-H bond. A process based on a direct gas phase activation would not be pragmatic as it may result in a poor selectivity control. In addition, as it will be described in chapter 5, there are technological hindrances in working with photons below 160 nm. Gruzdkov et al. showed that methane physisorbed at 40 K on a Pt(111) single crystal could be photodissociated upon irradiation with an ArF excimer laser irradiating at 193 nm [37]. Although of evident scientific interest, the use of lasers for industrial processes is challenging because of their price, efficiency and limited active area (spot). An alternative monochromatic source of VUV photons called "excimer lamp" has been developed in the past decades. As extensively described in chapter 5, an excimer lamp constitutes a cheap, efficient and convenient source of photons which proved already its ability to be applied to large scale processes.

1.4 Motivation

The photoassisted activation represents an interesting strategy to convert methane into oxygenated compounds or higher hydrocarbons. However, all the reported experiments dealing with this system make use of lasers and most of the time single crystals.

The aim of the present work, is to investigate the effect of a xenon excimer lamp towards the activation of methane on Ni-Pd/$\gamma - Al_2O_3/Si$ catalysts.

In order to achieve this goal, suitable model catalysts are required. They must be conductive in order to be characterized by a wide range of surface spectroscopic techniques including XPS, AES and AFM. In addition, a well-defined surface morphology containing small and homogeneous metal particles is the key for active and selective catalysts. Suitable preparation conditions resulting in the formation of well-defined and homogeneous clusters on the substrates should therefore be established.

A major part of this work has been devoted to the construction and characterization of a

miniature xenon excimer lamp which was a prerequisite for the ultimate goal of project. No excimer lamp able to operate in UHV conditions is commercially available or reported in the literature. Such a setup is technically demanding because of the very limited space available in our system connected with the high tension needed and cooling requirements. Finally, the combination of the model catalysts prepared and the excimer lamp will allow the investigation of the reactivity of the catalysts and the influence of the 172 nm photons towards there reactivity of methane. To our knowledge, this work is the first involving the use of an excimer lamp to study the activation of methane. A key feature of the present project is the use of catalysts and devices potentially usable at a larger scale.

Chapter 2

Experimental techniques

2.1   X-ray Photoelectron Spectroscopy (XPS)

XPS, also called ESCA (Electron Spectroscopy for Chemical Analysis), is a quantitative and surface sensitive spectroscopic technique that permits to determine the surface composition as well as the chemical and electronic state of the components present within a material.

XPS is based on the photoelectric effect discovered by Hertz in 1887 and mathematically described by Einstein in 1905, where the concept of photon was used to explain the ejection of electrons from a surface when photons impinge upon it. However, the modern analytical technique that we know today was developed much later, in the mid 1960s by K. Siegbahn and his research group. K. Siegbahn was awarded the Nobel Prize of Physics in 1981 for his work on XPS [38].

The photoelectric effect consists of the emission of electrons from a material irradiated by soft X-rays. For XPS analyses, Al K_α (1486.6 eV) or Mg K_α (1253.6 eV) lines are often the photon energies of choice. As it can be seen in table 2.1 aluminum and magnesium produce X-rays characterized by a narrow FWHM and a high intensity. Each atom on the surface has core electrons with a characteristic binding energy which is conceptually equal to the ionization energy. When an X-ray beam is directed towards the surface of a sample, the energy of the X-ray photons may be absorbed by core electrons of the surface atoms. If the energy of the incoming photons is sufficient, these electrons will then escape the surface

Source	hν (eV)	FWHM (eV) (A)	Intensity (B)	Satellite Separation (eV) (C)	Satellite Intensity (D)	Preferred Window Material
Mg Kα	1253.6	1.1	100	8.4	8	Al
Al Kα	1486.6	1.3	50	9.8	6	Al
Si Kα	1739.6	1.5	19	11.1	4.6	Be
Zr Lα	2042.4	2.15	5	82.0	41	Be
Au Mα	2122.9	2.9	3	81.8	67	Be
Ag Lα	2984.3	3.3 (E)	1	167.0	40	Be
Ti Kα	4510.9	2.6 (E)	0.3	- 6.0	50	Be or Al

(A) Measured on Ag 3d$_{5/2}$ using the same spectrometer resolution.

(B) Peak intensity relative to Mg Kα using the same power (15kV, 20mA) on the x-ray source.

(C) Satellite separation at higher kinetic energy (lower binding energy) from the principle x-ray line position.

(D) Satellite intensity as a percentage of principle x-ray intensity.

(E) Estimations based on natural line widths reported in the literature.

Table 2.1: Possible anode materials for XPS

atoms. The electrons with the kinetic energy E_K are referred to as photoelectrons and have a characteristic energy distribution that allows the identification and quantification of the atoms they originate in the solid. The spectrum is obtained by measuring the number of photoelectrons generated as a function of their kinetic energy. A typical spectrum of a $Ni/\gamma - Al_2O_3$ catalyst is shown in figure 2.1. The kinetic energy E_K of the core electron is given by the Einstein relationship:

$$E_K = h_\nu - E_B - \phi \tag{2.1}$$

Where $h\nu$ is the energy of the incident photon, E_B is the energy of the core level relative to the Fermi level of the sample and ϕ corresponds to the work function of the spectrometer. On the energy-level diagram shown in figure 2.2, we can see that the kinetic energy measured is independent of the sample work function Φ_{Sample}. This diagram as well as equation 2.1 are only valid for samples in good electrical contact with the spectrometer. If this condition is not fulfilled and as a consequence of the emission of photoelectrons from the sample, a residual positive charge builds up in the material. If the sample is in good electrical contact with the spectrometer, this charge is immediately neutralized by a flux of electrons from the spectrometer [39]. This problem is especially significant in the case of a
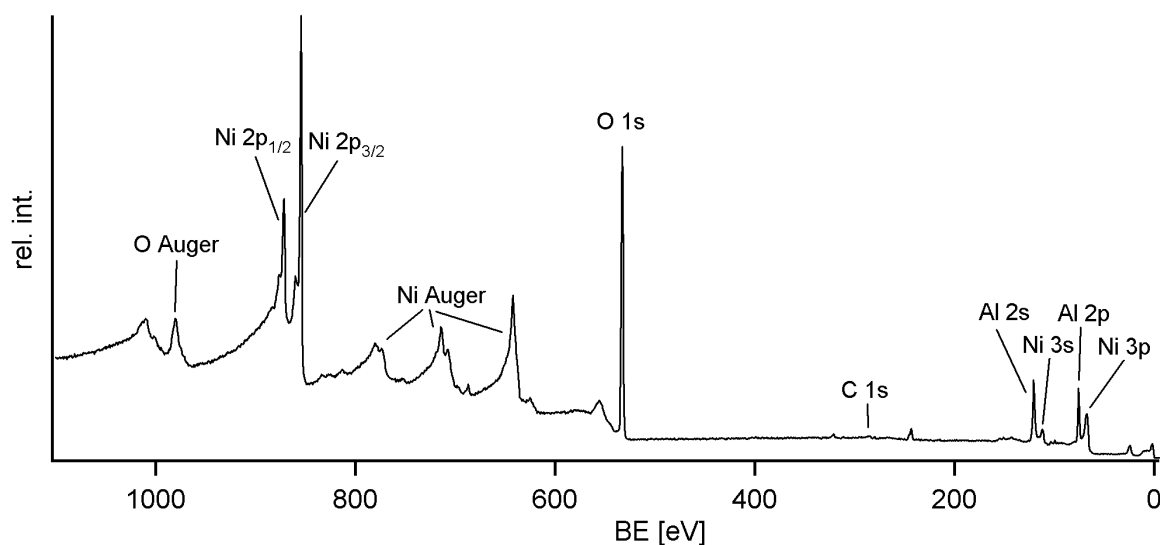
Figure 2.1: XPS spectrum of a $Ni/\gamma - Al_2O_3$ catalyst.

monochromatic X-ray source where low energy electrons available to neutralize the sample are produced in smaller amount than in the case of a non-monochromatic source. Charging causes a shift of the Fermi level of the sample relative to the one of the spectrometer resulting in a "charging shift" towards lower kinetic energies of the photoelectrons reaching the detector. A variety of procedures exists to circumvent this problem and correct the energy scale of spectra but none of those is universal. In this work, the C1s peak is assigned a binding energy of 284.5 eV and the whole spectrum is shifted to get the carbon signal matching this value. This technique has been reported not to be reliable [38], especially in the case of semi-conductors and inhomogeneous samples, but considering its ease of application, it remains a solution of choice when used with caution.

The property which makes of XPS one of the favorite techniques in various fields like catalysis, corrosion science, semi-conductors or adhesion science is surface sensitivity. Solids interacts with the environment through their surface which is therefore of highest importance for the characterization/identification of any sample.

Let us consider a 1 cm edge cube of a typical transition metal (e.g. nickel). This cube is made of about 10^{23} atoms of which only 10^{16} can be found at the surface corresponding to 100 ppb of the atoms. If we then want to detect impurities at a concentration 0.1%
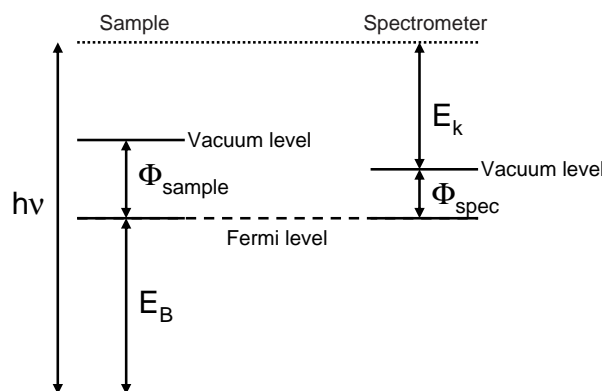
Figure 2.2: Energy-level diagram for a sample in good electrical contact with the spectrometer.

we need a detection limit of 0.1 ppb! The proportion of atoms on the surface of course depends on the shape and roughness of the sample but it remains that surface analysis techniques must be extremely sensitive [40].

Electron spectroscopies are usually well suited to surface analysis because they rely on the fact that electrons going through a medium will undergo energy losses and therefore have a limited penetration depth. The excitation source doesn't need to be surface sensitive as the electrons emitted by the sample undergo energy losses on their way out and the intensity of those electrons will be exponentially damped as a function of the emission depth.

The energy loss process of electrons traveling through a solid can be quantified by the Inelastic Mean Free Path, IMFP. The latter corresponds to the average distance electrons can go in a solid before undergoing an inelastic collision. It is interesting to notice in figure 2.3 that the IMFP varies with the kinetic energy of the photoelectrons and passes through a minimum around 50 eV. As the energy increases further, Seah and Dench were the first to report that the dependence of the IMFP with KE can be modeled with a power law of the form:

$$IMFP \propto (KE)^x \tag{2.2}$$

where x is typically between 0.5 and 1 depending on the class of material (e.g. organic materials, metals, oxides...) [42].

In the interval of energies commonly used for XPS analyses, that is between 10-1000 eV the
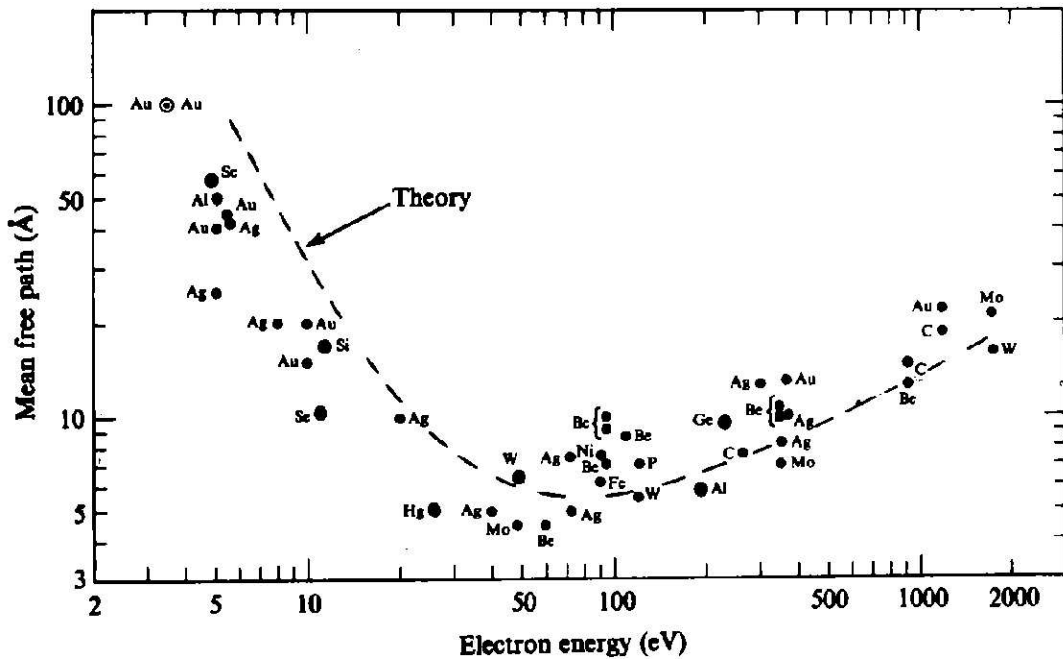
Figure 2.3: IMFP versus kinetic energy for few elements [41].

IMFP is in the range of few atomic layers. It is also noteworthy that the dependence of the IMFP regarding the kinetic energy is qualitatively the same for all materials and therefore the IMFP values tend to a common curve so-called "*universal curve*" if plotted versus the electron energy. It was initially believed that only inelastic scattering was responsible for the decay of the electron intensity obeying a Beer-Lambert law so that:

$$I = I_0 \exp \frac{-z}{IMFP * cos\theta} \tag{2.3}$$

I stands for the intensity contribution of the atoms located up to a distance z from the surface, I_0 is the intensity of an infinitely thick uniform substrate and θ is the take-off angle of the photoelectrons with regard to the surface normal. Understanding in this area has changed significantly in the last decades and it was realized that elastic scattering through which the trajectory of electrons is changed without any energy transfer cannot be neglected. This effect is especially important for large emission angles, leading to

significantly greater values of IMFP. Equation 2.3 is therefore only an approximation of the in-depth distribution of the detected photoelectron intensity but a rigorous calculation taking into account elastic scattering requires complex computations like Monte Carlo simulation. Lassen and co-workers [43] compared the efficiency of different algorithms to correct for elastic scattering effects in the interpretation of angle resolved XPS (ARXPS) and angle resolved AES (ARAES) results of several well-defined overlayer/substrate systems. They found from a systematic study that replacing the IMFP in equation 2.3 with an effective attenuation length (EAL) λ was leading to a mean percentage deviation of 10% compared to the nominal over-layer thickness of their sample, while it is between 13-68% using standard IMFP. Attenuation lengths take into account the influence of elastic scattering and are usually about 10% smaller than IMFP. Tabulated values can be found in [44].

Assuming an exponential decay of the electron intensity, as described above, the escape depth is defined as the depth from which 65% of the signal originates and is equal to λ. In the same way, 85% and 95% of the photoelectrons emitted are coming from a depth of 2λ and 3λ respectively.

The sampling depth can be reduced through angle resolved experiments and increased using more energetic X-ray sources like the titanium K_α or silver K_α lines giving the core electrons a higher kinetic energy. However, sensitivity problems may arise from the choice of X-ray sources like Ti or Ag due to their much lower photoemission cross-section compared to Mg or Al.

When a material is exposed to X-rays, the probability to assist to the emission of a photoelectron per incident photon is the following:

$$P_{A,i} = \sigma_{A,i} N_A d \tag{2.4}$$

$\sigma_{A,i}$ is the photoelectric cross section of orbital i in element A, N_A is the atomic concentration of element A in the sample in $atom/cm^3$ and d is the thickness of the probed area. The photoelectric cross section $\sigma_{A,i}$ corresponds to the probability that an incident photon excites an electron of orbital i in element A. Values of cross section can be obtained by calculation or determined experimentally. Calculated values from Scofield are available in [45] and empirical values can be found in [46].

However, the interesting point is not the probability to excite an electron but the probability for this electron to escape from the sample without undergoing energy losses. For a homogeneous sample, the probability for a photoelectron to be emitted from a depth z is given by equation 2.5:

$$dP_{A,i}^{esc}(z) = \sigma_{A,i} N_A \exp \frac{-z}{\lambda_{A,i}} dz \tag{2.5}$$

which can be integrated over the depth:

$$P_{A,i}^{esc} = \sigma_{A,i} N_A \int_0^\infty \exp \frac{-z}{\lambda_{A,i}} dz \tag{2.6}$$

to give equation 2.7:

$$P_{A,i}^{esc} = \sigma_{A,i} N_A \lambda_{A,i} \tag{2.7}$$

The intensity of the photoelectrons detected from shell i of element A is proportional to the photon flux $F_{h\nu}$, that is the X-ray intensity and to the transmission function of the spectrometer $T_{A,i}$ according to equation 2.8. This relation is the fundamental equation for the determination of the surface composition of homogeneous samples.

$$I_{A,i} = \sigma_{A,i} N_A \lambda_{A,i} F_{h\nu} T_{A,i} \tag{2.8}$$

$I_{A,i}$ corresponds to the area under the peak of the corresponding transition. Equation 2.8 can be used for direct quantification in a so-called "first principle approach" but this technique is not very convenient and usually the relative atomic concentration in percent is calculated with equation: 2.9:

$$C_A = \frac{\dfrac{I_{A,i}}{Sf_{A,i}}}{\sum_n^n \left(\dfrac{I_{n,i}}{Sf_{n,i}}\right)} \tag{2.9}$$

Equation 2.9 is valid for a sample which is at least homogeneous within the sampling depth. The parameters: $\sigma_{A,i}$, N_A, $\lambda_{A,i}$ and $T_{A,i}$ are included in a set of sensitivity factors $Sf_{A,i}$, which are experimentally determined for the spectrometer used.

2.2   Auger Electron Spectroscopy (AES)

Auger electron spectroscopy is, as XPS, a surface sensitive spectroscopic technique for the determination of the composition of the outermost few atomic layers of a material. "Auger" comes from the name of Pierre Auger (1899-1993), a French physicist who is reported to have discovered this process in 1925 [47] [48] [38]. However, Lise Meitner (1878-1968) an Austrian physicist was the first to discover the Auger effect and to report it in 1923 in the journal *Zeitschrift für Physik* [49], that is two years before Pierre Auger [50]. Auger's name was probably associated with this process because of political or gender issues.

The Auger process is initiated by the creation of an electron vacancy in a deep-lying core level of an atom. Several techniques can be used to produce this vacancy but bombardment with an electron beam of typically 2-10 keV is the most common one. The highly excited atoms will eventually relax by filling the core hole with an electron coming from a higher level. The energy liberated through this process can finally be dissipated through the emission of an X-ray photon, phenomenon called *X-ray fluorescence.* Alternatively, the energy can be used to excite another electron from an external energy level which will be emitted out of the atom and is called "Auger electron". When a deep lying hole is created those two processes are competing but the probability for the emission of an Auger electron is much larger for holes having an initial binding energy lower than 10 keV. Figure 2.4 illustrates the relative probability of relaxation by emission of an X-ray photon or an Auger electron after creation of a core hole in a K-Shell as a function of the atomic number. It is noteworthy that the Auger process can also be initiated through irradiation of the sample with X-ray photons. As a matter of fact, Auger features can also be observed in XPS spectra. The Auger process is illustrated on picture 2.5 where an incident radiation creates a vacancy in a K (1s) shell. This vacancy is filled by an electron from level $L_{2,3}$ (2p) and finally another $L_{2,3}$ electron is ejected. This Auger electron is called $KL_{2,3}L_{2,3}$. It is common to omit the subscripts for the groups of electrons having the same quantum number and to write simply KLL. Some authors go even further in the generalization using terms like CVV for transitions involving one core and two valence electrons or CCC for three core electrons [40]. In figure 2.5, the kinetic energy of the $KL_{2,3}L_{2,3}$ electron can be roughly approximated as being equal to the difference between the energy of the core hole
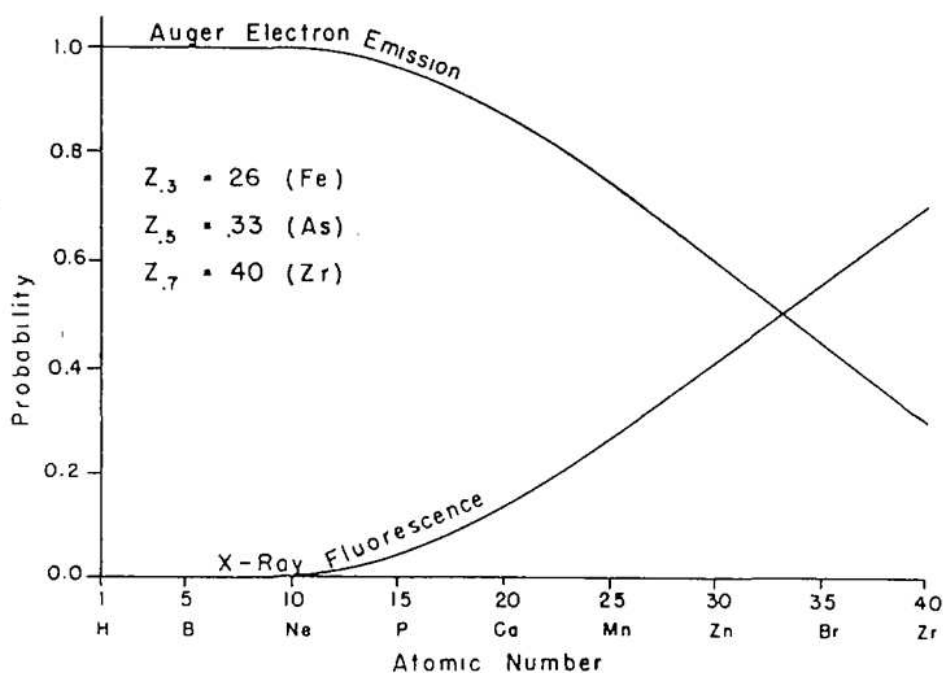
Figure 2.4: Probability of relaxation by X-ray fluorescence and emission of an Auger electron consequently to the formation of a core hole in a K shell [51].

and the two valence electrons according to equation 2.10.

$$E_{KL_{2,3}L_{2,3}} = E_K - E_{L_{2,3}} - E_{L_{2,3}} \tag{2.10}$$

The exact calculation of the kinetic energy of Auger electrons is rather complex as other parameters like the interaction energies between the core holes in the final atomic state or inter- and extra-relaxation energies should be taken into consideration. However, it is noteworthy that the kinetic energy of Auger electrons is independent of the nature as well as of the energy of the excitation source but is characteristic of the sample. An Auger spectrum of a slightly contaminated and oxidized nickel sample is shown in figure 2.6. This spectrum, called direct spectrum shows the total electron signal as a function of the kinetic energy, including Auger electrons and the massive background from secondary and backscattered electrons which basically do not contain any analytical information. This is not a convenient way to display AES spectra as the spectrum is completely dominated
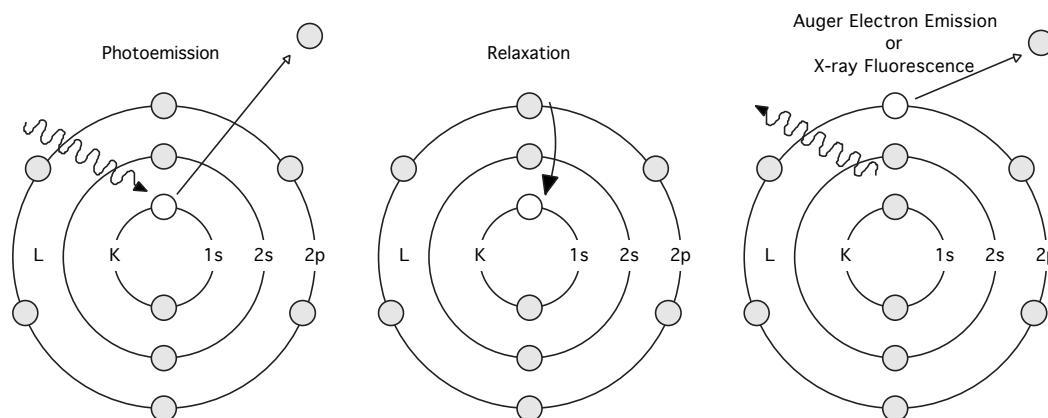
Figure 2.5: Illustration of the 3 steps involved in the relaxation of an ionized atom leading to the emission of an Auger electron [40].

by the background and Auger features appear as very small structures. This problem is especially significant for the detection of contaminants like P,S,Cl or Pb having low intensity signals. This difficulty can be circumvented by taking the derivative of the electron signal in order to suppress the background and to enhance the Auger features. The spectrum of figure 2.7 was obtained by differentiating the spectrum of figure 2.6. The differentiated spectrum is usually preferred to display Auger spectra [52]. On the dI/dE spectrum the intensity of the transitions can be determined by measuring the peak to peak distance which is approximately proportional to the peak area of the direct spectrum. Two methods are used in practice for quantitative Auger analysis. The first one compares the intensity of the elements present in the sample with the one of an external standard having a known concentration. Provided the external standards are comparable to the sample under investigation, this method cancels parameters like the ionization cross section and Auger yield reducing the analysis to a signal amplitude measurement. The major hindrance of this technique is to find a standard with a similar composition to that of the sample. If this condition is not fulfilled, than the influence of the matrix on both the backscattering factor and the escape depth must be considered in detail. Another method, less accurate however highly convenient, involves the use of atomic sensitivity factors. The atomic concentration
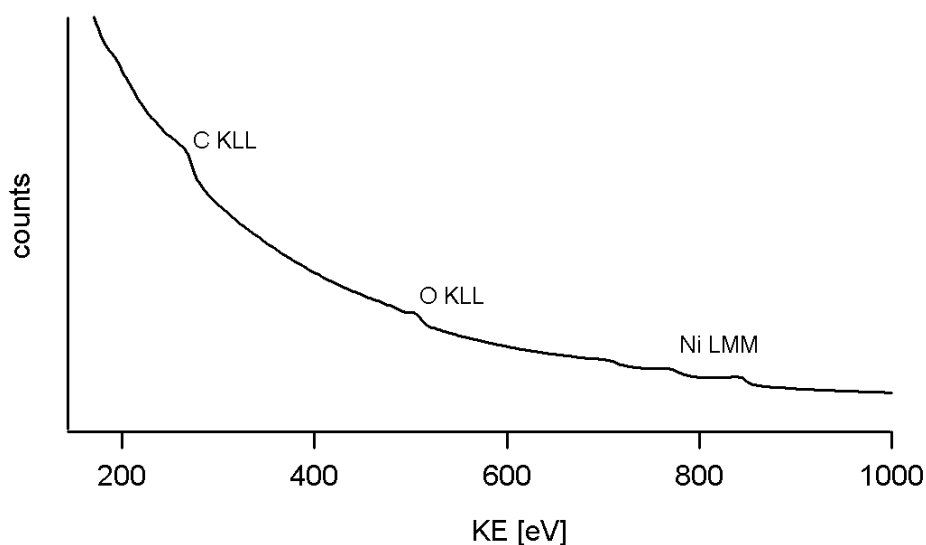
Figure 2.6: Direct Auger spectrum of a contaminated nickel sample.

of an element A in the sample can be calculated by the mean of an equation similar to that used for XPS analyses.

$$C_A = \frac{\dfrac{I_A}{S_{f,A}^{AES} d_A}}{\sum_n^n \left(\dfrac{I_n}{S_{f,n}^{AES} dn} \right)} \tag{2.11}$$

S_f^{AES} is a relative sensitivity factor weighting the intensity of the elements present in the sample with regard to the Ag (351 eV) peak. dx is a scale factor taking into account the electron beam current and energy which cancels if the different transitions are measured with the same beam parameters. As this method neglects variations in the backscattering factor and escape depth with material, it is a semi-quantitative method. It has however the advantage to avoid the need of a large number of pure elemental standards [53].

The major drawback of AES is its lack of accuracy for chemical analyses. It is also noteworthy that the chemical composition of the sample may be subject to modifications due to the excitation source used. It is a matter of fact that many compounds, particularly oxides, are readily decomposed under electron irradiation, so called beam-induced effects. XPS is the preferred technique for investigating the chemistry of the surface as photoelec-
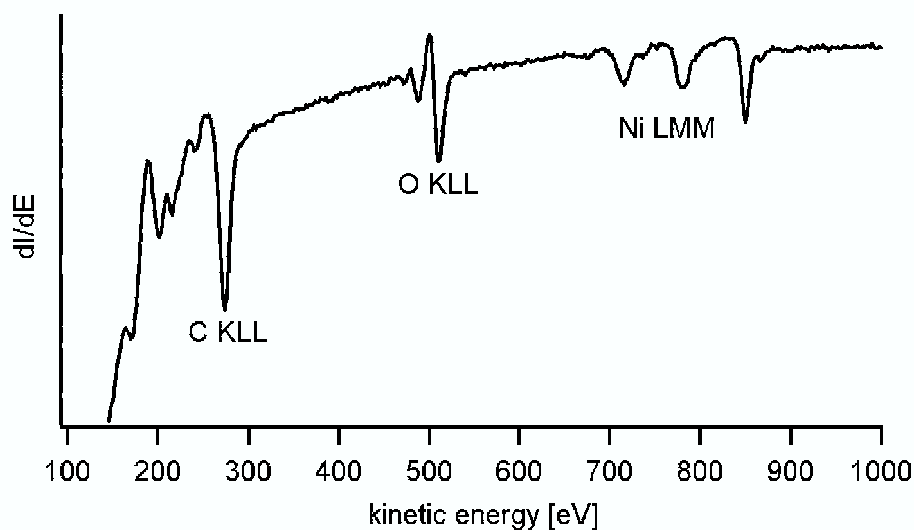
Figure 2.7: Spectrum of figure 2.6 displayed in the differentiated mode.

tron peaks are sharper and chemical effects are more easily interpreted than in the case of the corresponding Auger peaks. On the other hand the main feature making of AES one of the key surface analysis method is its spacial resolution. It is indeed possible to focus an intense electron beam down to a very small spot leading to spacial resolution up to 10 nm compared to few micrometers in the best case for XPS. AES and XPS should therefore be regarded as two complementary techniques.

2.3 Spectroscopic Ellipsometry (SE)

Spectroscopic ellipsometry is a non destructive and contact-less optical technique for the investigation of dielectric properties of thin films. More specifically, this technique measures the change of polarization of a linearly polarized light upon transmission or reflection on a sample. SE is in principle used in the reflection mode where an incoming beam is aimed on the sample and reflected to a detector as shown in figure 2.8.

The basic principles of spectroscopic ellipsometry are known for a long time [54] but data analysis was a major drawback to the wide application of this technique before the advent

of cheap computers in the sixties. SE has nowadays a wide range of applications going from the determination of physical properties in fields like semiconductors, polymer chemistry or optical coating to real time monitoring of chemical and physical processes (etching, oxidation, thermal annealing, chemical vapor deposition...).

The main limitation of SE is the model necessary for the calculation of the optical parameters which is only valid for samples composed of a small number of well-defined layers optically homogeneous, non-absorbing and isotropic [55].

The polarization state of the incident beam may be decomposed into a component s,
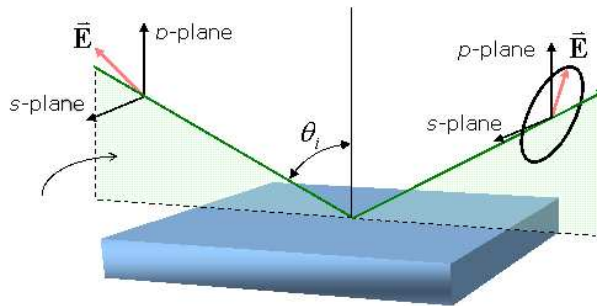
Figure 2.8: Schematic illustration of a typical ellipsometry experiment.

oscillating perpendicular to the plane of incidence and parallel to the sample surface, and a component p oscillating parallel to the plane of incidence. In other words, the p component of the incident and reflected light waves oscillate in the same plane. SE is based on the fact that when a linearly polarized beam reflects on a surface there is a shift of the phases of both p and s. As this shift is usually not the same for the two components, an elliptically polarized beam results from this reflection which is the reason for the name of this technique [56]. This fact is illustrated in figure 2.9.

For both components s and p of the electric field vector, the changes taking place on the sample are described by the amplitude reflection coefficients r_p and r_s [57].

$$r_p = \frac{E_{rp}}{E_{ip}} = \frac{N_1 cos(\theta)_2 - N_2 cos(\theta)_1}{N_1 cos(\theta)_2 + N_2 cos(\theta)_1} \tag{2.12}$$

$$r_s = \frac{E_{rs}}{E_{is}} = \frac{N_1 cos(\theta)_1 - N_2 cos(\theta)_2}{N_1 cos(\theta)_1 + N_2 cos(\theta)_2} \tag{2.13}$$

Equations 2.12 and 2.13 are the so-called Fresnel equations. N_1 and N_2 represent the
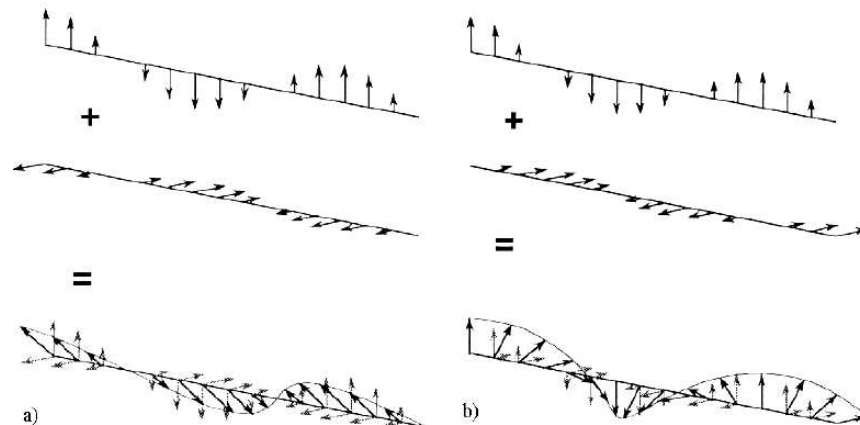
Figure 2.9: a) Components s and p have same amplitude and are in phase, the beam is linearly polarized b) Components s and p are out of phase, the beam is elliptically polarized.

complex refractive indices of the media crossed by the beam as shown in figure 2.10 and can be expressed in terms of real refractive indices n and extinction coefficients k in eq. 2.14.

$$N_i = n_i + ik \tag{2.14}$$

The refractive index indicates the speed of light in the material following equation 2.15 and the imaginary part or extinction coefficient determines how fast the amplitude of the wave decreases.

$$v = \frac{c}{n} \tag{2.15}$$

k is related to the absorption coefficient by eq. 2.16 where α is the absorption coefficient and λ the wavelength of light.

$$\alpha = \frac{4 * \pi * k}{\lambda} \tag{2.16}$$

As mentioned earlier, p- and s-polarization show different changes in amplitude and phase upon light reflection. An ellipsometry experiment measures two values (ψ, Δ) that express the amplitude ratio and phase difference between p- and s- polarization respectively. In fact, if we define δ_1 as the phase difference between parallel (s) and perpendicular (p) components of the incident wave and δ_2 the phase difference between the components of the reflected beam, eq. 2.17 defines Δ as the phase change that components -s and -p
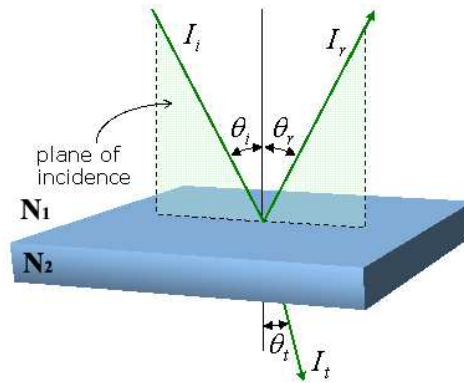
Figure 2.10: Schematic illustration of the incident, reflected and transmitted beams.

experience upon reflection:

$$\Delta = \delta_1 - \delta_2 \tag{2.17}$$

The change of amplitude of components -s and -p can be expressed by the mean of equation 2.18:

$$tan\Psi = \frac{\mid r_p \mid}{\mid r_s \mid} \tag{2.18}$$

Ψ is the angle whose tangent is equal to the ratio of the magnitude of the reflection coefficients. This brings us to the fundamental equation of ellipsometry .

$$\frac{r_p}{r_s} = tan(\Psi)exp(i\Delta) \tag{2.19}$$

A spectroscopic ellipsometry experiment provides values of Ψ and Δ, which depend on the thickness and optical constants of the sample as a function of the wavelength of the beam. A mathematical model corresponding to the sample under analysis has then to be developed. This model should include the order of the layers the sample is made of as well as the thickness and the optical constants characterizing these layers. Parameters of interest like typically void fraction or layer thickness in the case of a multi-layer sample can then be fitted and determine with a high accuracy [58].

2.4   Atomic Force Microscopy (AFM)

Atomic force microscopy is a topographic imaging technique based on the interactions between a sample and a sharp tip typically made of silicon or silicon nitride and installed on a cantilever. An atomic force microscope (AFM) can be considered as a modified profilometer, characterized by contact forces between the tip and the sample surface of less than 10^{-9} N, that is less than interatomic forces, instead of about 10^{-4} N for a standard profilometer. The main advantages of such weak interactions are a limited tip-induced deformation of the surface and a reduced contact area between tip and surface allowing a better resolution [59].

The detection system does not measure directly the force acting on the tip but it "sees" the deflection of the cantilever with an optical technique consisting in detecting the change of position of a laser beam reflected on the back of the cantilever. This is achieved by aiming the laser beam on a position sensitive photodiode such that a deflection of the cantilever will move the beam spot on the diode. The vertical deflection of the cantilever Δz is related to the force acting between the tip and the sample surface following equation 2.20 where k stands for the elastic constant of the cantilever.

$$F = k\Delta z \tag{2.20}$$

An AFM can operate in two different modes called **contact** and **tapping**. In contact mode, the tip is brought very close to the surface, typically few $\mathring{A}$, where interaction forces are mainly repulsive. These forces result from the repulsion between the atomic shells of the tip and the sample when they are contacted. The tip is then scanned over the surface and the cantilever deflection is kept constant by applying a voltage to a piezoelectric transducer via a DC feedback amplifier. This voltage is therefore a measure of the height of structures on the sample surface. The sample topography is reproduced by plotting the z position of the piezo as a function of the location of the tip on the surface. Imaging in contact mode requires sufficiently low forces to avoid any surface deformation. In contact mode, measurements in ambient conditions may turn out to be difficult because of the layer of adsorbed gases on the sample, consisting of 10-30 monolayers of mainly water and nitrogen, causing the cantilever to be attracted towards the surface by capillary forces.

This problem can be overcome by working with the probe and the sample immersed in a fluid. This is however technically more complicated and can also lead to sample damage. An attempt to overcome these complications is the tapping mode which is a dynamic imaging technique. The cantilever is driven here to oscillate up and down over the sample by with of a piezo located in the tip holder. The resonance frequency of the cantilever is typically included between 50 to 500 kHz with an amplitude of 50 to 200nm [59]. When the tip starts to interact with the surface, the oscillation amplitude decreases due to energy losses, indicating a "bump" on the sample. A feedback loop adjusts then the height of the sample in order to reset the original oscillation amplitude. As the tip is placed alternately in contact with the surface and then lifted off, it provides a high resolution, up to atomic level, without pulling material sideways by shear forces as the applied force is always vertical. This makes tapping imaging especially suitable for samples that are easily damaged, loosely hold to their substrate or presenting difficulties connected with electrostatic forces, friction or adhesion.

It is noteworthy that the term microscopy is erroneous as it implies looking while information is obtained by "feeling" with a mechanical probe. In addition, the picture of the surface obtained by AFM does never correspond exactly to the actual topography of the sample, but is a convolution of the surface and the tip. As a matter of fact, the resolution of the picture obtained is strongly dependent on the apical probe geometry [60].

2.5   Quartz Crystal Microbalance (QCM)

The resonance frequency of a mechanical vibrational system depends, among other parameters, on the total mass of the oscillation body. A **quartz crystal microbalance (QCM)** monitors therefore the mass of an adsorbent per unit of area by measuring the change of frequency of a quartz crystal resonator. Such a piezoelectric resonator is a cut slab from a natural or synthetic single crystal of quartz. The application of an external voltage to such a crystal will result in an internal mechanical stress. Thus, when electrodes are attached to a quartz crystal, it can be made to vibrate at the frequency of the excitation source. If the frequency of the driving voltage corresponds to the resonance frequency of the crystal, the amplitude of the mechanical vibrations will reach a maximum. The frequency corre-

sponding to this maximum will depend on the mass of the crystal itself but of course also on the mass of the material deposited on the resonator. In fact, a direct proportionality exists between the mass of material on the quartz and the frequency change. The vibration frequency of the quartz decreases with the increasing mass on the crystal.

Piezoelectricity was first observed by Pierre and Jacques Curie in 1880 [61] and the mass-induced downward shift of the frequency has been known since quartz-crystal resonators have been used for frequency-controlled applications in radiocommunication equipments. However, the understanding of this phenomenon was only of qualitative nature until it was explored by Sauerbrey in 1959 [62]. A QCM based on this technique is extremely sensitive and allows a measurement in situ, in liquid or gas phase, with a detection limit of 0.1 ng/cm^2 [63]. One of the first applications of QCM reported in the literature was as gas detector [64]. Later, the incorporation of various chemically sensitive layers on the oscillating crystal has enabled the transition from the microbalance to the mass sensor and resulted in an explosive growth of piezoelectric sensors in recent years. Nowadays, typical applications deal with the determination of the evaporation rate in evaporating chambers or the ablation process of polymers [65] [66] and since the eighties, QCM are also applied as biosensors to study for example the adsorption of proteins on functionalized surfaces.

Applying an alternating voltage between two electrodes of a properly cut quartz crystal will generate a highly stable oscillating shear deformation which is illustrated in figure 2.11. It is possible with standard equipment to determine the frequency of this oscillation
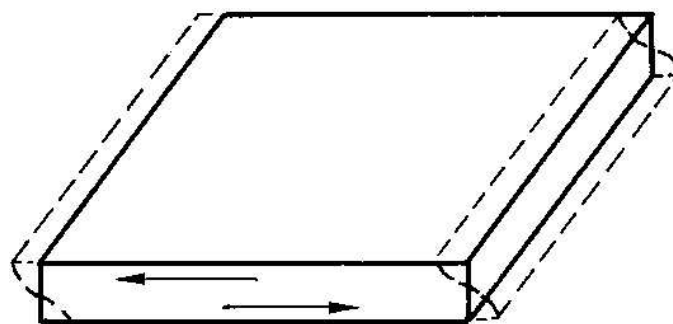
Figure 2.11: Illustration of the thickness-shear mode of vibration of an AT-cut quartz crystal.

with a precision of 1 Hz in the 4-6 MHz range. The crystal used in our experiments had a resonance frequency of 5 MHz. A typical QCM setup is made of a water cooled quartz crystal holder, a frequency sensing equipment, an oscillation source and a measurement device. The QCM itself consists of a thin piezoelectric plate with two electrodes evaporated on both sides of the crystal (see figure 2.12). In order to minimize the coupling

Figure 2.12: Resonator used in our quartz crystal microbalance.

between the oscillating frequency and the temperature, a special crystal cut known as AT-cut is employed. AT-cut quartz crystals are singularly rotated Y-axis cuts in which top and bottom halves of the crystal move in opposite direction during oscillation (fig. 2.13). The AT-cut crystal is relatively easy to fabricate and is rather insensitive to temperature variations around room conditions but has limitation at low and high temperature. Figure 2.14 shows the temperature sensitivity of the vibration frequency of rotated Y-cut quartz crystals. The relation between temperature and frequency is cubic and has an inflexion point around room temperature in the case of AT-crystals [67]. The AT-cut is therefore the most effective quartz crystal for operation at or near room temperature and is in fact the most widely used. It is noteworthy that other crystal cuts are available with different characteristics. The SC (Stress-Compensated) cut for example is a doubly rotated cut that minimizes the frequency change due to temperature gradients for high temperature operation. These crystals are characterized by an inflexion point at 92 ^oC and a "smoother" temperature-frequency relationship. They are therefore less affected by temperature deviations what decreases the dependence on water cooling. However, due to a more complex manufacturing process, they are more expensive and not widely used.
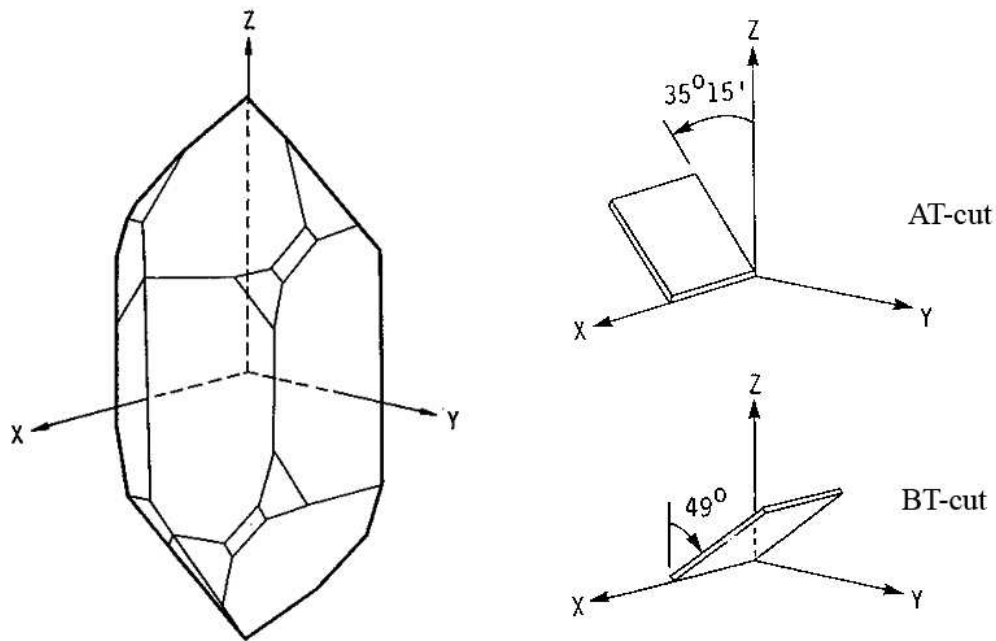
Figure 2.13: AT- and BT-cut quartz crystal plans.

As stated previously, the possibility of using a piezoelectric quartz resonator as mass-measuring device was first investigated by Sauerbrey. He found that the resonance frequency of a thickness shear vibrating crystal of quartz having an AT or BT cut was proportional to the mass build up on its surface according to equation 2.21:

$$\Delta f = -\frac{2f_q^2}{v_q \rho_q S} M_f \tag{2.21}$$

where Δf is the frequency shift induced by the mass of the deposited film M_f, f_q is the fundamental resonance frequency of the crystal, ρ_q is the density of quartz equal to 2650 kg/m^3, S is the surface area of the deposited film and v_q the propagation velocity of an acoustic wave in quartz equal to 3340 m/s for an AT cut crystal.

The resonance frequency of a quartz crystal in the fundamental thickness mode is given by equation 2.22:

$$f_q = \frac{v_q}{2t_q} \tag{2.22}$$

where t$_q$ is the quartz thickness. This equation tells for example that a crystal resonating at 5 MHz will have a thickness of 0.33 mm. Equation 2.22 can also be expressed with
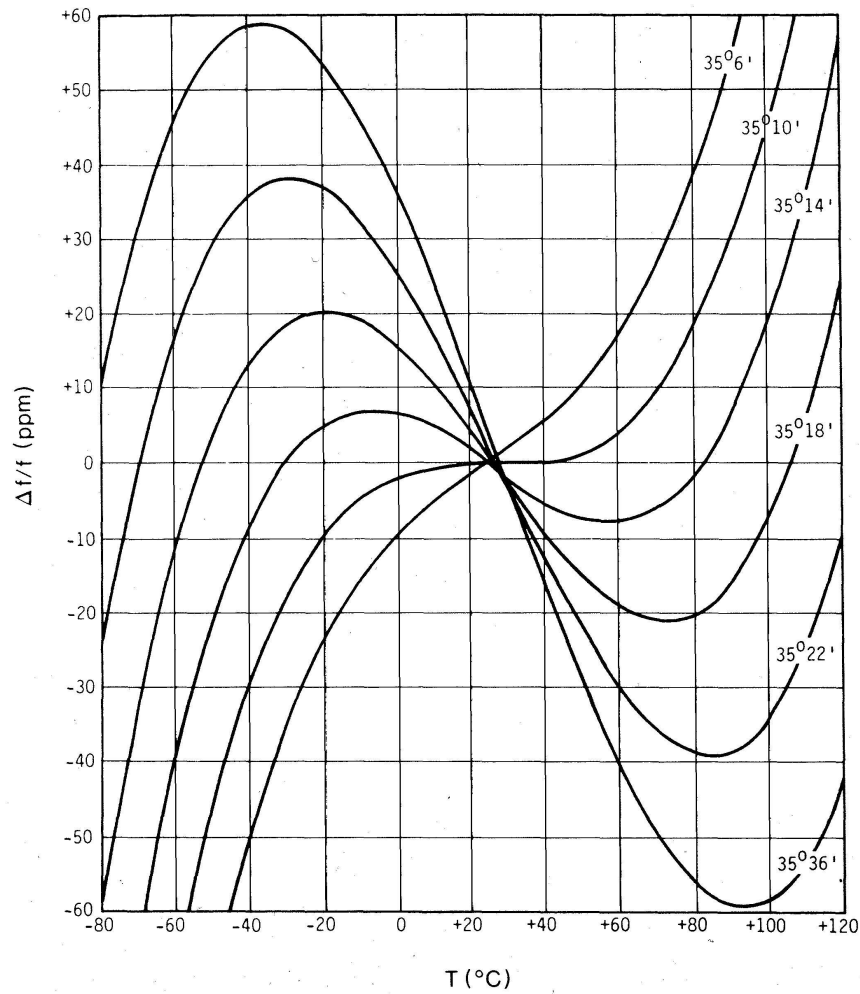
Figure 2.14: Temperature dependence of the vibration frequency of different rotated Y-cut quartz crystals [68].

equation 2.23 in which M_q is the mass of the vibrating quartz.

$$f_q = \frac{v_q S \rho_q}{2 M_q} \tag{2.23}$$

If we now substitute equation 2.23 in 2.21 we obtain equation 2.24:

$$\frac{\Delta f}{f_q} = -\frac{M_f}{M_q} \tag{2.24}$$

If the density of the material is spatially uniform, we can define the areal densities m_f and

m_q as the mass per unit area of the deposited film and the quartz crystal respectively as follows:

$$m_f = \frac{M_f}{S} \tag{2.25}$$

and:

$$m_q = \frac{M_q}{S} \tag{2.26}$$

Substituting equations 2.25 and 2.26 in 2.24 yields:

$$\frac{\Delta f}{f_q} = -\frac{m_f}{m_q} \tag{2.27}$$

It is often of advantage to use areal densities rather than the total mass as the vibrating area of the quartz does not necessarily extend to the whole surface and is not easy to determine. The active area corresponds in fact to the part of the crystal located between the electrodes. Equation 2.27 is well supported by experimental data up to a mass load of m_f/m_q of about 2%. Equation 2.25 can also be substituted in 2.21 to yield equation 2.28:

$$\Delta f = -\frac{2f_q^2}{v_q \rho_q} m_f \tag{2.28}$$

which is more generally expressed by grouping the proportionality factor between Δ_f and m_f in a constant called *mass sensitivity* or *calibration constant*:

$$\Delta f = -C_f m_f \tag{2.29}$$

and therefore:

$$C_f = 2\frac{f_q^2}{\rho_q v_q} \tag{2.30}$$

Replacing ρ_q and v_q by the values corresponding to an AT-cut quartz crystal, equation 2.29 tells us that the mass sensitivity of a 5MHz resonator is 5.65 MHz·m^2/kg. This means that a frequency variation of 1 Hz corresponds to a mass change of 17 ng/cm^2 or a thickness of 0.19 Å if we consider a nickel film.

2.6 Quadruple Mass Spectrometry for Thermal Programmed Reactions Studies (TPR)

Mass spectrometry is based on the production of ions from the substance to analyze which are then separated and detected with respect to their mass over charge ratio (m/q).

Sir Joseph J. Thomson (1856-1940) is usually considered to be the father of mass spectroscopy through his work on the analysis of *negatively charged cathode ray particles* (called electrons today) [69] and of positive rays with a parabola mass spectrograph, the ancestor of a mass spectrometer [70]. Sir J.J. Thomson managed to determine the mass spectra of O_2, N_2, CO_2 and $COCl_2$ and was awarded a Nobel prize in 1906. Since then, the resolution, sensitivity, mass range and accuracy of the technique has improved tremendously. For instance, the resolution of 13 m/δm (m="mass" here) in 1913 [70] increased to 2000 [71] in 1937 to reach eventually 8'000'000 in 1998 [72]. A similar evolution happened with the detection limit going successively from the pico-, atto-, and femto-mole level to a record of 800 yocto-moles for the detection of a peptide in solution [73]. By the 1960s, mass spectrometry was mainly used for the analysis of organic compounds. Later innovations, especially concerning the analyzer and the ionization technique induced a widespread utilization of mass spectrometry in fields like medicine, environmental science, material science, geology, forensic science, physics, chemistry, and especially life science. The development of gentler ionization modes in particular has opened up new possibilities for the analysis of high molecular mass molecules or sensitive materials of biological relevance. Such a wide application of mass spectrometry can be explained by the numerous advantages of the technique [74]:

- It provides an excellent molecular specificity because of its ability to yield both molecular mass and structural information of molecules or fragment ions

- It is extremely sensitive

- It can detect all elements

- It can be applied to all kinds of sample, volatile or not, solid, liquid or gaseous

Mass spectrometry data are presented as mass-to-charge ratio corresponding to the mass of the particle (m) divided by the the number of charge (z) of this ionized particle. The total charge of the ion is therefore q=ze where e is the charge of an electron ($1.602 \cdot 10^{-19}$ C). The unit of the mass to charge ratio is the Thomson [75], however the term m/q is common practice in the literature.

A mass spectrometer is made of three main components; the ion source, the mass analyzer and the detector (fig. 2.15). The role of the ion source is to transform the neutral
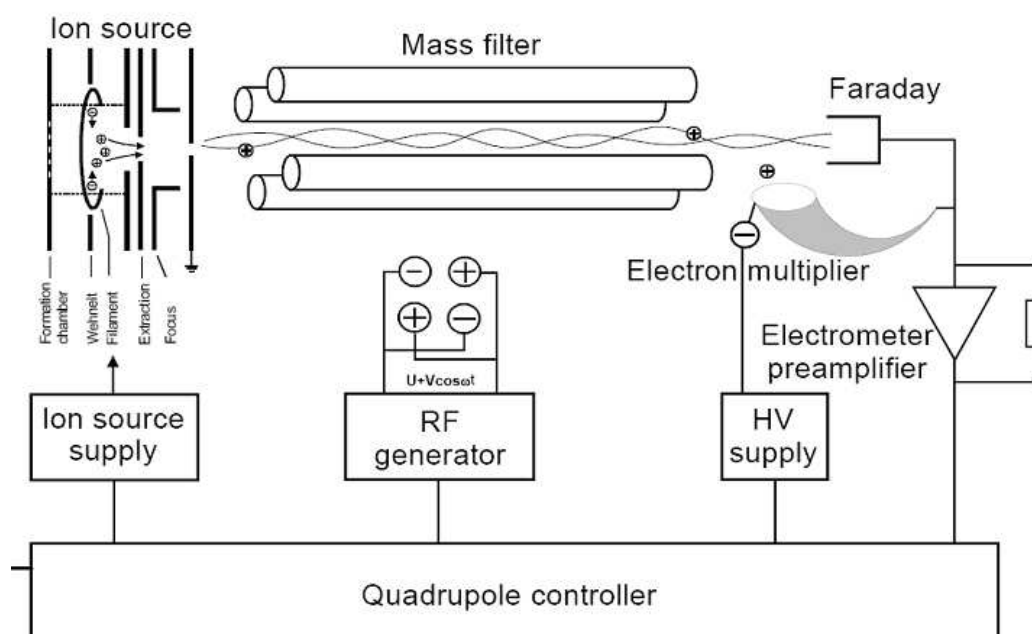
Figure 2.15: Schematic representation of a mass spectrometer.

species into ions prior to analysis. It is in fact much easier to manipulate the motion and direction of ions than neutral species. Many different ionization techniques can be used, each having its own advantages and drawbacks. The choice of the most suitable technique is usually based on the physico-chemical properties of the analyte (volatility, molecular weight...). These different techniques can usually be subdivided into two main classes: those requiring the sample to be in the gas phase prior to ionization and those able to deal with low volatility and/or high molecular weight. The first class includes electron impact ionization (EI) and chemical ionization (CI) representing the most widely used techniques. Those belonging to the second class are electro-spray ionization (ESI), atmospheric pressure chemical ionization (APCI), atmospheric pressure photoinduction (APPI) and matrix assisted laser desorption/ionization (MALDI). The electron impact ionization technique was used in the present work and is based on the interaction of an energetic electron beam with the sample in the gas phase. The electron beam is generated by a heated filament

and accelerated by a potential between the filament and an anode located on the opposite side of the ionization chamber 2.16. Electron ionization usually leads to the production
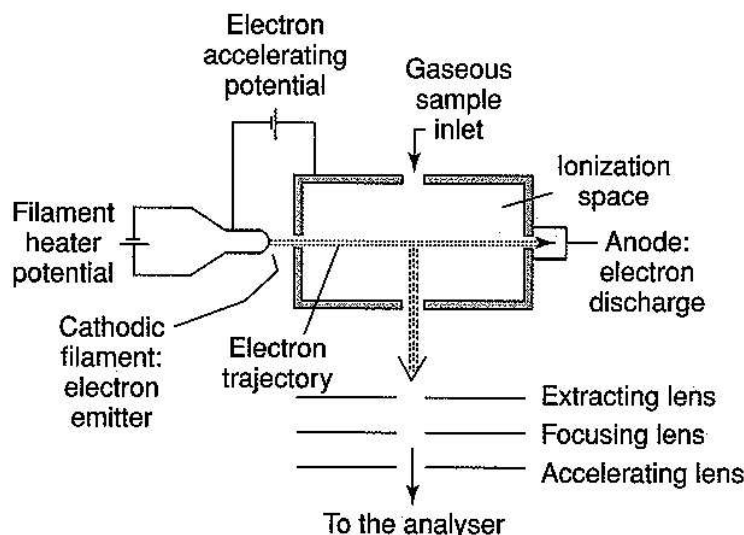
Figure 2.16: Schematic representation of an ionization chamber.

of a molecular ion resulting from the loss of an electron from the neutral molecule and a series of fragments.

Once the ions have been produced in the ion source, they have to be separated with regard to their m/q ratio and the resolved fragments must be focused on a single focal point to be finally detected. As in the case of the ion source, many different analyzers exist, all having their own advantages and limitations. The most popular are the magnetic sector which was used on the first instruments at the beginning of last century, quadrupole, quadrupole ion trap (QIT), quadrupole linear ion trap (LIT), orbitrap, time of flight (TOF) and ion cyclotron resonance (ICR) [76]. A common feature of all these analyzers is that they all make use of static and/or dynamic electric and magnetic fields in order to separate the analyte ions. The basic difference relies on how these fields are used to achieve the separation. The performance of a mass spectrometer can be evaluated on the basis of the following characteristics [77]:

- The *resolution* is the ability to separate two neighboring ions.

- The *mass range* or the highest m/q fragments which can be detected.

- The *sensitivity* is the smallest amount of an analyte which can be detected.

- The *mass accuracy* is the measured error in the m/q ratio divided by the accurate m/q value.

- The *speed* corresponds to the rate at which a particular mass range can be measured in mass unit per second or millisecond.

- The *transmission* is the ratio of the number of ions reaching the detector and the number of ions entering the analyzer

The analyzer used in this work is a quadrupole and is actually the most widely employed system. This device is based on the fact that ions having different m/q values will behave differently in alternating (radio frequency) electric fields. A quadrupole consists of four rods of circular or ideally parabolic section (fig. 2.17) which must be perfectly parallel. Each pair of opposed rods are connected together and held at the same potential which consists of a DC and an AC component [77]:

$$\Phi_0 = +(U - V\cos\omega t) \text{ and } -\Phi_0 = -(U - V\cos\omega t) \tag{2.31}$$

In equation 2.31, Φ_0 is the potential applied to the rods, ω is the angular frequency (rad/s), U is the direct potential and V the "zero to peak" amplitude of the RF voltage. The mass separation is accomplished by varying U and V while keeping the ratio U/V constant. U varies typically between 500 and 2000 volts and V between 0 and 3000 volts. In figure 2.18, the stability areas of masses m1, m2 and m3 are shown. Scanning along the line U/V allows the successive detection of the different masses. It is therefore clear that the resolution can be improved by increasing the slope of the line U/V, as long as it goes through the stability areas.

Once the ions have crossed the analyzer, they enter the detector which basically converts them into a usable signal. In the present case, this signal is an electrical current which is proportional to the ion flux. Many different detectors are commercially available but the most widely used ones are the Faraday cup and the secondary electron multiplier. The spectrometer used in this work was equipped with both of these devices.

The *Faraday cup* is a simple and robust detector which is made of a metal cup or an inclined
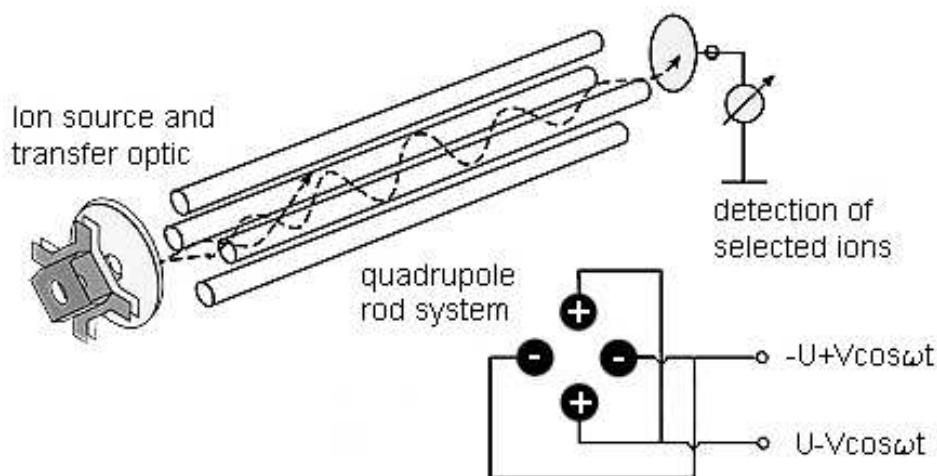
Figure 2.17: Illustration of the mass separation principle of a quadrupole analyzer.

collector electrode surrounded by a metal cage. When an ion beam impacts towards the collector, a voltage drop develops across a resistor inducing a current which is then amplified and measured. This device is very precise because the charge induced on the "cup" is independent on the mass, speed and energy of the detected ions. It suffers however from a low sensitivity and a slow response time and is therefore used in the case of high count rates. The intrinsic properties of this detector make it suitable for the precise measurement of the ratio of specific ion species like isotopes in isotopic ratio mass spectrometry (IRMS). The *secondary electron multiplier* (SEM) is nowadays the most common ion detector in mass spectrometry. It can be a discrete dynode electron multiplier or a channel electron multiplier (CEM or channeltron) which can be seen in figure 2.19. The working principle of this detector is based on the fact that when an ion impinge on the surface of a metal or a semiconductor, secondary electrons are emitted from that surface. If the electrons released are then further accelerated successively against other surfaces by an electric field, the same phenomenon appends again resulting in an "avalanche" of electrons inducing an electric current at the end of the detector. A channeltron is a horn shaped device made either from a lead doped glass having good secondary emission properties or coated with beryllium. A voltage of about 2 kV is applied between the two ends of the tube to create a field throughout the length of the channeltron. The beam of ions is made to knock at the
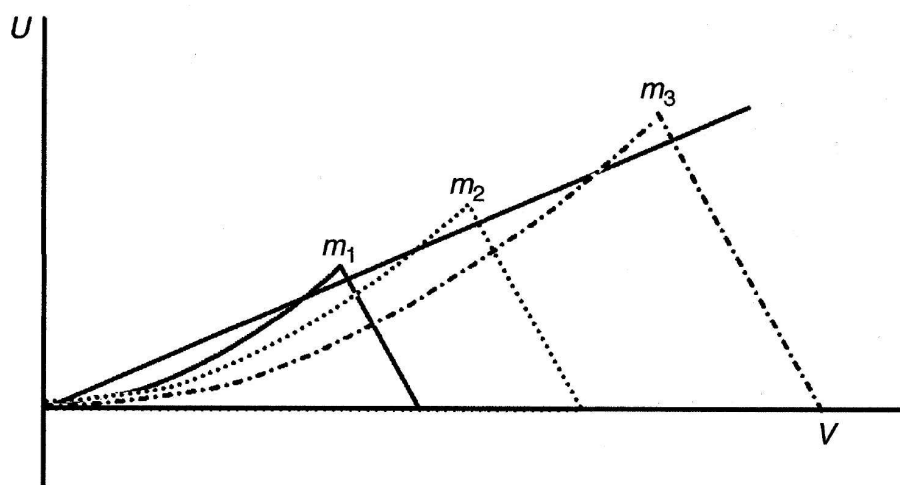
Figure 2.18: Stability areas as a function of U and V for three different masses (m1<m2<m3) [78].
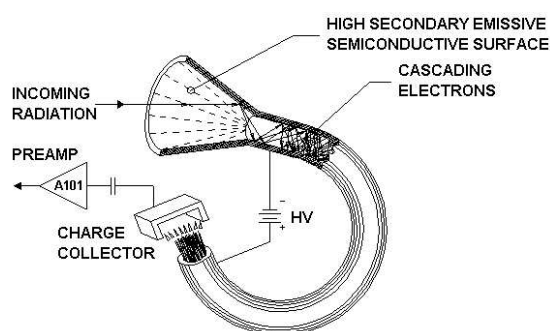
Figure 2.19: (a) Illustration of the working principle of a secondary electron multiplier (b) Picture of a channeltron

entrance of the detector and the electrons resulting from this collision are then accelerated under the influence if the field against the opposite wall producing more electrons at each collision until they reach the end of the tube. Channeltrons provide an excellent sensitivity, a very fast response time and a high gain, the amplification can be as high as 10^8. This makes them especially suitable in the case of low intensity signals. However, they may have a limited lifetime due to surface contamination coming from the detected ions or poor vacuum conditions.

Chapter 3

Experimental setup

3.1 The UHV system

Most of the experiments presented in this work were carried out in the UHV system shown in figure 3.1. This installation is made of several vacuum chambers connected to a central distribution chamber by the mean of mechanical gate valves. The different side chambers are all dedicated to some specific tasks and all possess a separated pumping and venting system. They can therefore be isolated from the rest of the setup, what provides a great working flexibility. In fact, this allows several operations to be carried out simultaneously or a particular chamber to be vented for maintenance or repair without stopping the whole installation. The setup depicted in figure 3.1 is composed of a fast entry air lock (FEAL) corresponding to number 1 (fig. 3.1), an electrochemistry chamber (2), a LEED/AES chamber (3), a preparation chamber (4), a high pressure cell (5), a storage chamber (6) and finally an analysis chamber (7). The high pressure reactor and the electrochemistry chamber have not been used in this work and will therefore not be described in detail. The system can be subdivided into two parts. The first one is the XPS spectrometer (ESCALAB 250i-XL) to which belongs the analysis chamber. The spectrometer was bought in 1995 from the company Vacuum Generators and upgraded in 2008. The second part of the setup was elaborated at the Paul Scherrer Institut by Dr. J. Wambach. It was designed and fabricated by the company Dentech and then continuously updated to improve its performance.
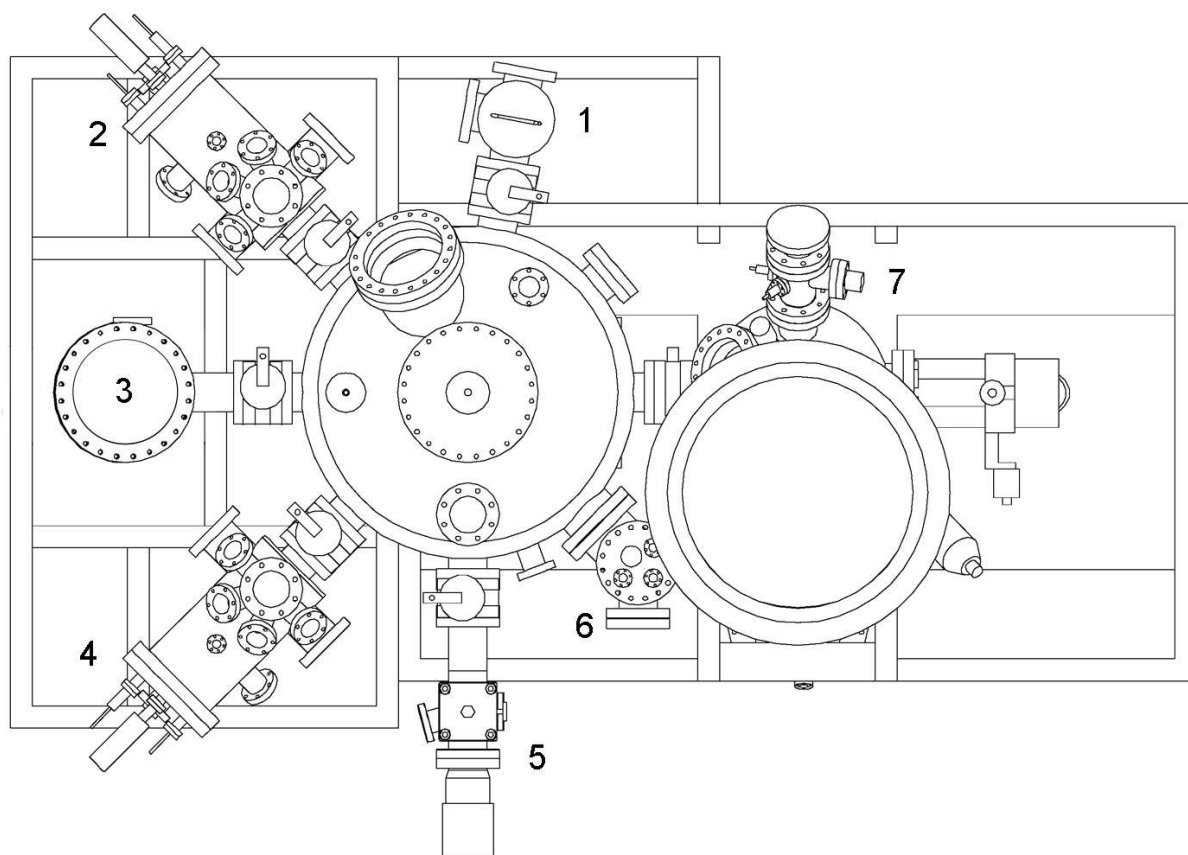
Figure 3.1: Drawing of the UHV setup: fast entry air lock (1), electrochemistry chamber (2), LEED (3), preparation chamber (4), high pressure reactor (5), sample storage chamber (6), analysis chamber (7).

3.1.1 The FEAL

The fast entry air lock (FEAL) is the point where samples are introduced into the system. The door is sealed with a Viton 'O' ring and pressed against the chamber under the effect of the vacuum. It is not a UHV chamber, due to frequent exposure to atmosphere, but is capable of pumping down to $5 \cdot 10^{-8}$ mbar by a Pfeiffer TPU 060 turbomolecular pump connected to an Edwards E2M5 two stage rotary pump which are both controlled by the XPS control system. The main utilization of this chamber is for introducing or taking out samples from the system although it is often used for degassing samples to avoid the contamination of the rest of the system. Due to the very limited volume of this chamber,

a pressure of $<10^{-6}$ mbar can be reached typically within ~ 15 minutes in the case of low surface area samples. The gate valve between the distribution chamber and the FEAL can then be opened and the sample transferred to the UHV.

3.1.2   The distribution chamber

The distribution chamber represented in the center of figure 3.1 contains a carousel made of an extendable and rotatable mechanical arm equipped with a sample holder locking system at its extremity. The arm can be rotated about the vertical axis of the chamber and can access the side chambers through rotation of an actuator situated on the top of the chamber controlling the elongation of the arm. The sample holder seizing mechanism of the arm can be locked and unlocked by application of a slight pressure against the sample holder.

The distribution chamber was initially pumped by a Physical Electronics 220 l/s ion pump resulting in a base pressure of about $2 \cdot 10^{-9}$ mbar. A good vacuum in the distribution chamber is essential to avoid contamination of samples stored or transferred. In order to lower the base pressure of the distribution chamber which was the highest of this UHV setup, a home made titanium sublimation pump (TSP) was designed and built in the frame of this work (fig. 3.2). Titanium sublimation pumps are designed to trap both chemically

Figure 3.2: In-house built titanium sublimation pump.

reactive and inert gases, they are renowned for their high pumping speed and reliability. Titanium is easily sublimed if heated at a suitable temperature and pumping takes place through the reaction of the freshly evaporated titanium with "reacting" gases (H_2, N_2, H_2O, O_2) or by burring (trapping) rare gases on the pump housing without chemical reaction. A titanium pump is especially suited in our case as ion getter pumps do not pump hydrogen. In fact, hydrogen diffuses back out of the pump cathode after being trapped. Our device contains two Titanium/Molybdenum (85%/15%) filaments, heated one minute every two hours by running of current of 50 amperes at 5 volts with a VG PSU controller. This pump appeared to be very effective as the base pressure of the distribution chamber dropped by one order of magnitude to $2{\cdot}10^{-10}$ mbar after installation.

3.1.3 The storage chamber

The storage chamber is in fact part of the distribution chamber and is used as a sample park. It contains a lift actuated by a rotary feedthrough connected to a threaded rod. The lift can therefore be moved vertically in the chamber and contains six sample holder receiving stations allowing to work simultaneously with different samples.

3.1.4 The LEED chamber

The installed 4-grids LEED (type "ErLEED") can easily be fitted with a retarding field analyzer allowing to carry out Auger measurements in addition to LEED analyzes. The system was bought from the company Specs (PU-IQE 11/35 model). The chamber is pumped down to a base pressure of $2{*}10^{10}$ with a Pfeiffer TPU 240 backed by a Scroll pump Leybold SC 15D. This chamber is also used to differentially pump the nozzle of the mass spectrometer installed in the preparation chamber through a flexible DN40CF flexible coupling. This differential pumping noticeably improves the sensitivity of the mass spectrometer.

3.1.5 The analysis chamber

As mentioned previously, the analysis chamber is part of an XPS spectrometer (VG Escalab 220i-XL) upgraded to the Escalab 250i-XL version. The analysis chamber, lens and analyzer housings are constructed from Mu-metal. Mu-metal is a special alloy thermally treated in an oxygen free atmosphere. It has the property to shield the charged particles in the chamber from external magnetic fields, maintaining an optimum performance even at the lowest electron energies. The analysis chamber is equipped for XPS and AES standard analyses and imaging but also for scanning electron microscopy (SEM). Sample cleaning and depth profiling can be carried out with an ion gun (EX05) controlled by a T 164 digital unit. An ion getter pump Physical Electronics 120 l/s together with a titanium sublimation pump are in charge of the evacuation of this chamber which results in a base pressure $<10^{-10}$ mbar.

The electron analyzer is a spherical sector analyzer consisting of two concentric hemispheres and can be operated both in spectroscopic or imaging mode. It is preceded by an input transfer lens which has the task to capture the maximum possible number of emitted photoelectrons from the sample and transfer them to the analyzer with a minimum loss. This is achieved by the use of several electrostatic lenses, L1, L2, and the combination of both, L3. In order to increase its sensitivity, the ESCALAB 250i-XL is fitted with a magnetic immersion lens (or XL lens), which is located below the sample. The XL lens increases the acceptance angle of the electrons emitted from the sample over a cone of up to about 45° into the main lens column, increasing the number of photoelectrons detected and thus the sensitivity. The input lens maybe operated in either a purely 'electrostatic' mode or in a hybrid 'magnetic mode'. In the electrostatic mode, the input lens consists of a pair of electrostatic lenses (L1 and L2) and in the magnetic mode, the input lens is a combination of the magnetic XL lens and L2. The magnetic field from the XL lens is generated by a coil located beneath the sample holder. The use of the magnetic lens is restricted to well conducting samples as the associated magnetic field deviates the trajectories of low energy secondary electrons preventing them to be captured by the sample and thus to reduce the charging generated by the escape of the photoelectrons. By changing the relative strengths of the different lenses, a certain degree of zooming can be achieved and a range of fields

of view accommodated. When using the electrostatic lens, the field of view may have a diameter in the range of 500 μm to 8 mm. With the XL lens, the analyzed area has a diameter of 120 μm to 1 mm.

After the lens system, the electrons are filtered in the analyzer according to their kinetic energy. This is achieved by applying a voltage between the two hemispheres of the analyzer. This voltage disperses the electrons in the direction across the gap between the hemispheres which is called "energy dispersive direction". The hemispherical analyzer acts as a narrow pass filter, allowing only electrons within a defined energy window ΔE, centered on the pass energy E_p, to reach the channeltron detector. Electrons with a higher kinetic energy will collide in the outer hemisphere while electrons with a lower kinetic energy will meet the inner hemisphere. In this way, only electrons with kinetic energies around E_p are able to go through the exit plate and be detected by an electron multiplier unit made of an array of six channeltrons.

The analyzer can be operated in two modes known as constant retard ratio (CRR) or constant analyzer energy (CAE). The difference between the CRR and the CAE modes is related to the way in which the pass energy is varied while acquiring a spectrum.

In the CAE mode, the pass energy E_p is kept constant as the kinetic energy is scanned by the analyzer. This means that the voltage difference between the hemispheres remains constant as the kinetic energy changes.

In the CRR mode, the pass energy changes proportionally to the kinetic energy of the photoelectrons. The retard ratio is defined as E_p/KE. This implies that the absolute resolution of the analyzer will decrease with increasing kinetic energy while the transmission will increase. Alternatively, the relative resolution $\Delta E/E$ will stay constant throughout the energy range.

The CRR mode is usually preferred for Auger analysis as Auger peaks are intrinsically relatively broad (1 eV - 2 eV) and therefore resolution is less important in AES than in XPS. At low Auger energies, E_p and therefore the transmitted signal is low, but again this is acceptable because the total signal is high. The CAE mode is usually preferred for XPS analysis as the quantification is facilitated due to a constant transmission and resolution over the whole spectrum.

When operated in imaging mode, the spectrometer acts as an energy selective filter. Only

electrons with a preset narrow energy range are allowed to reach the detector. The intensity of these electrons is then recorded as a function of their position on the sample, resulting in a two dimensional picture of the sample surface. In order to achieve that, the spatial information of the electrons is preserved while they travel through the input lens and the analyzer. They are not detected by the channeltrons as in the case of standard analyses but are processed by an output lens which produces a magnified representation of the sample on the image detector. This detector consists of two superimposed channel plates coupled to a phosphor screen. Each photoelectron reaching the channel plates (25 mm^2, 10 μm pore size) is amplified by a factor 10^6 before reaching the phosphor screen. The light produced by the interaction of the photoelectrons with this screen is finally detected by a CCD camera through a vacuum view port.

The analysis chamber is equipped with two X-ray sources, an XR4 Twin anode including magnesium and aluminum and a monochromated aluminum source.

The twin anode can generate X-rays with two different energies which can be selected by the operator. The radiations produced are not energy filtered and therefore composed of the main K$_\alpha$ peak but also of the K$_\beta$ superimposed on a background called "Bremsstrahlung". The twin anode is especially interesting for poorly conducting samples as it produces a large number of secondary low energy electrons which contribute to lower significantly the charging resulting from photoemission process. In addition, the twin anode can be used to distinguish X-ray induced Auger electron peaks from the true photoelectron features. Switching from one source to the other, XPS peaks remain at the same binding energy whereas Auger peaks remain at the same kinetic energy with an apparent shift of 233 eV on a binding energy scale. Magnesium has the advantage over aluminum that its X-ray line-width is narrower and twice as intense as the one of aluminum. The FWHM of the observed photoelectron peaks is therefore lower and the intensity higher. This can be explained by the fact that the spectrum obtained is a convolution of the intrinsic XPS features and the excitation source. The other lines of the X-ray source, like K$_\beta$, will therefore also appear in the final XPS spectrum as satellite features making the interpretation and quantification of the spectral results more complex.

The monochromated source produces X-rays by a sharply focused electron beam hitting an aluminum anode. The X-rays are then diffracted by a pair of quartz crystals which are

arranged such that the angle between the crystal lattice is the appropriate Bragg angle to give a pure K_α line with a FWHM of 0.3 eV. The resulting X-ray beam is then focused on the sample into a spot which can be varied between about 0.8x1 mm^2 and 0.1x0.1 mm^2 by setting the appropriate parameters on the electron gun. The narrower X-ray line width of a monochromatic source is reflected in the XPS spectra and results therefore in a higher resolution. The absence of the Bremsstrahlung background and other unwanted satellite features simplifies the spectral data obtained and facilitates the subsequent analysis. Finally, concentrating the X-ray radiations into a small spot allows small area analyses with a high sensitivity. The main limitation of monochromated sources relies in sample charging issues.

The ion gun mentioned at the beginning of this section (EX05 ion gun) is used as an etching source and is usually operated with argon to generate an ion beam of 0.1 to 4 keV hitting the sample at 45°. Argon is admitted to the gun via a leak valve, forming a region of low pressure gas which is ionized by electron impact at the rear of the ion gun. The latter is differentially pumped to maintain a pressure of about 10^{-7} mbar in the main chamber while the region of the gun filament is at a pressure of typically $2 \cdot 10^{-5}$ mbar. The argon ions are then extracted from this region and accelerated towards the sample. The resulting ion beam is focused by some lenses and before leaving the gun, it passes between two pairs of scan plates which deflect the beam in X and Y in order to obtain a well-defined, regular rectangular crater.

The analysis chamber is also equipped with VG LEG 1000 electron gun which can be used for Auger analyses or SEM imaging. In the case of SEM, the electron beam produced generates secondary electrons from the sample which are then detected by a scintillator photomultiplier. This system will however not be described further as it was not used in the present project.

3.1.6 The preparation chamber

Most of the experiments presented in this work have been made in the preparation chamber (PC). The pumping is carried out by a Pfeiffer TPU 240 turbomolecular pump (pumping speed: 220 l/s of N_2) backed by a Leybold SC 15D Scroll pump (pumping speed 15 m^3/h)

shared with the LEED chamber. The system is therefore completely oil free and achieves, with the help of a titanium sublimation pump, a base pressure of $6 \cdot 10^{-11}$ mbar. A picture of this chamber can be seen in figure 3.3. The PC is equipped with an ion gun (1), an
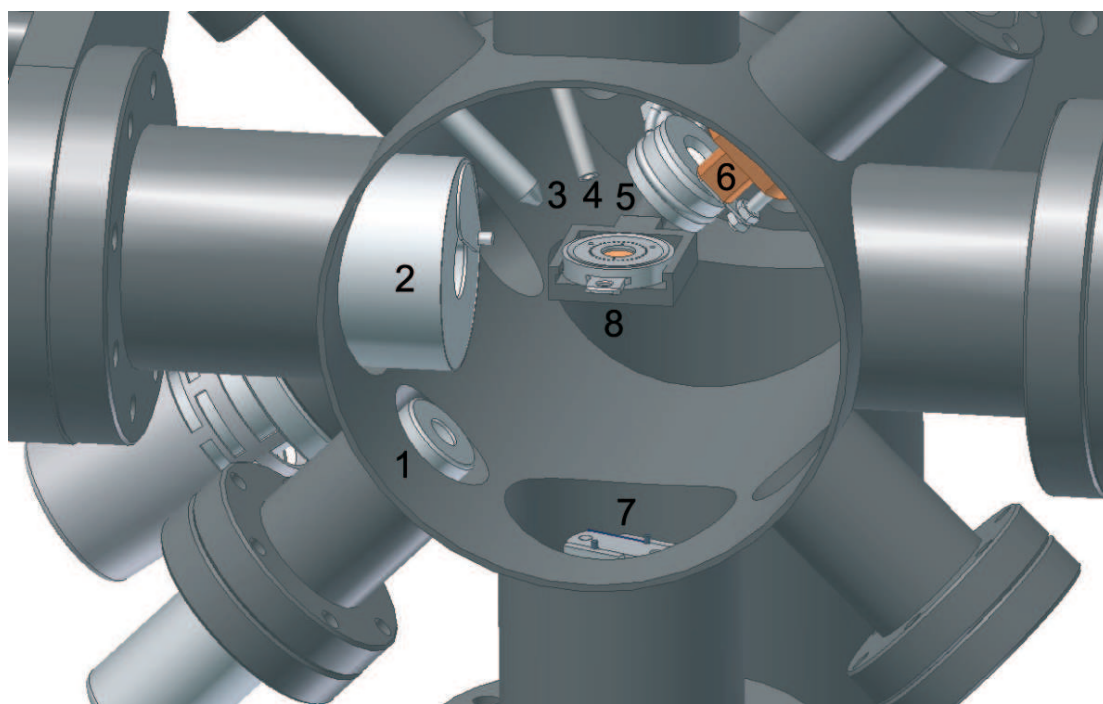
Figure 3.3: Drawing of the inside of the preparation chamber with: Ar-ion sputter gun (1), excimer lamp (2), mass spectrometer nozzle (3), gas inlet tube (4), quartz crystal microbalance (5), bimetallic metal evaporator (6), titanium sublimation pump (7), sample holder receiving station (8).

excimer lamp which is described in detail in chapter 5 (2), a quadrupole mass spectrometer fitted with a TPD/TPR nozzle (3), a gas dosing system (4), a quartz crystal microbalance (5), a metal evaporator able to evaporate two different metals (6), a titanium sublimation pump (7) and finally a heatable and coolable sample receiving station (8). Numbers 2, 3, 4, 5 and 6 are mounted on linear manipulators to be able to change freely their distance to the sample.

The ion gun is a Specs IQE 11/35 extractor type source and was used for substrate cleaning by Ar-ion sputtering. It generates an ion current of 10-15 μA in the case of Argon with a

Gaussian beam profile. The argon atoms are ionized by an electron beam produced from an Yttrium-oxide coated Iridium filament. These electrons are then accelerated towards a cage shaped anode where collisions with the argon atoms take place. The argon ions generated are finally accelerated out of the gun by an extractor plate at positive potential. The beam energy can be set with the Specs IQE 11/35 controller continuously from 0.1 to 5 keV. Argon is leaked directly into the ionization area via a gas line mounted on an integrated Mini-CF Flange (NW16CF). This system allows high current densities while keeping a relatively low pressure in the chamber, typically in the 10^{-5} mbar range.

The preparation chamber is also equipped with a Balzers Prisma 200 quadrupole mass spectrometer characterized by a m/q working range of 100. This device contains both a channeltron and a Faraday detector allowing a maximum pressure of 10^{-5} and 10^{-4} mbar respectively. A description of the working principle of the mass spectrometer can be found in section 2.6. The instrument is controlled via a RS232 port connected to a PC. The QMS can be operated in two modes, "scan analog" or "multiple ion detection" (MID). The former corresponds to the "standard" mass spectrum showing the intensity of different sequentially measured m/q signals. This strategy is usually applied for the quantitative identification of unknown gas mixtures or residual gas analysis of UHV systems. The MID mode is usually used for the investigation of time dependent phenomena as for instance TPD or TPR experiments. The intensity of some m/q signals can be selected in 64 different channels and recorded as a function of time. In the MID mode, the intensity of the selected signals is measured in parallel with the substrate temperature, what makes the handling of TPR/TPD data more convenient. In fact, only one set of data containing all the necessary information has finally to be analyzed. The actual temperature of the substrate during a ramp is provided to the QMS by a Eurotherm 900EPC device via a RS232 interface. The Eurotherm 900EPC controls the substrate temperature with an internal PID regulator.

The head of the mass spectrometer is installed inside a home made nozzle which can be seen in figure 3.3. The inside of this nozzle is differentially pumped by a flexible coupling connected to the LEED chamber and is terminated by a small hole of 1 mm diameter. The nozzle can be brought close to the sample surface with a linear manipulator. The distance between the sample and the nozzle opening has a significant influence on the spectra measured. In order to set this distance precisely and reproducibly, a copper tip is attached

to the extremity of the nozzle. When the sample-nozzle distance decreases to about 0.5 mm, the copper tip touches the sample holder resulting in an electrical contact which can be detected. This technique has the advantage to improve the quality and the sensitivity of TPD/TPR spectra. In fact, as the only contact between the preparation chamber and the inside of the nozzle is the 1 mm diameter hole, a local pressure increase near to the sample surface resulting from the desorption or production of some gas molecules during an experiment, results in a gradient between the "chamber side" and the inside of the nozzle. As a consequence, the gaseous species are "pumped" into the nozzle and detected by the mass spectrometer. In addition, it has been shown previously [79] that this technique prevents undesired species originating from materials surrounding the sample, like the sample holder housing, to be detected by the QMS.

The sample holder receiving station (figure 3.4) contains six contacts pins, two of them are used for heating and two others for temperature monitoring of the sample with a K-type thermocouple. These pins match of course corresponding contacts on the back of the
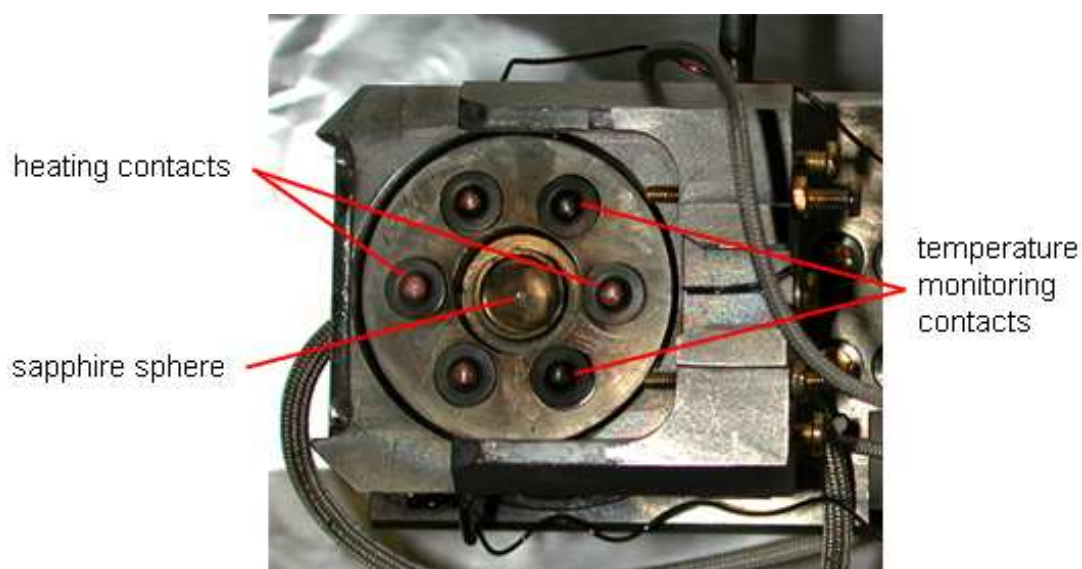
Figure 3.4: Top view of the sample holder receiving station with temperature monitoring, heating contacts and the sapphire sphere in the center.

sample holder and are fixed on a mobile plate. This plate can be moved up and down by a pneumatic actuator. When the plate is down, the sample holder can be introduced or

removed from the receiving station. When a sample holder is present on the station, the contact plate can be moved up under the effect of pressed air, pushing the different pins in their respective contact screws in the back of the sample holder. The contact plate is also fitted with a sapphire sphere which can be seen in the center of figure 3.4. This sphere, which is inserted in a nitrogen cooled copper rod, acts as "heat diode" during cooling or heating of the sample. As a matter of fact, sapphire has the properties to be thermally insulating at high temperature and to become a good heat conductor at low temperature. In this way, when the contact plate is pressed against the sample holder, the sapphire sphere is squeezed in a corresponding cavity of the sample holder and the sample can be heated as high as 1273 K and cooled down to $\approx$120 K where an efficient heat removal is necessary. The receiving station can be rotated around the axis corresponding to the sample transfer direction in order to face the different components of the preparation chamber.

The metal evaporator was designed and built in the frame of this work and is shown in picture 3.5. It is divided into two compartments containing each a selected metal. These

Figure 3.5: Drawing of the metal evaporator with a picture of the two compartments contained in the housing.

compartments which can be seen in the inset of figure 3.5 are separated by a cooled metal plate precisely fitted to a surrounding housing to avoid inter-contamination of the two metal sources. The metal evaporator contains two openings, one in the housing pointing to the sample holder and allowing the evaporating metal atoms to reach the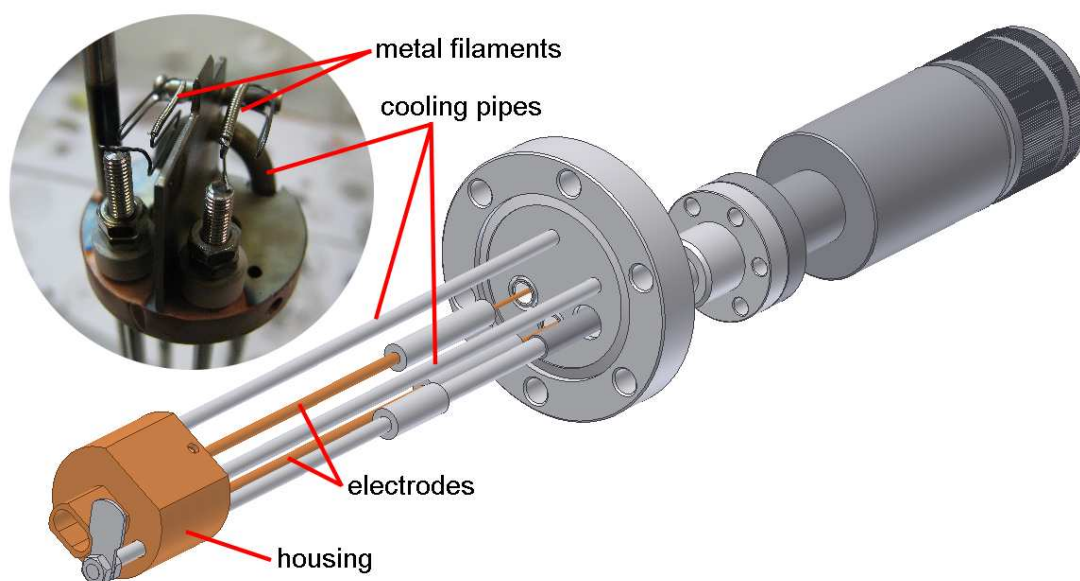 sample surface, and an other one on the back plate insuring a good pumping of the inside of the metal evaporator. The opening in the housing pointing to the sample holder is equipped with a "neck" to focus the metal beam on the sample and thus limiting the deposition of metal on neighboring parts. This opening can be closed with a shutter operated from the outside of the chamber by a rotary feedthrough to have a good control on the amount of metal deposited. The copper back plate is soldered to a water cooled stainless steel tube for an efficient heat removal. This helps to avoid a pressure increase during the evaporation and also to reach a stable evaporation rate rapidly. The filaments are made of a 0.4 mm diameter tungsten wire (inset fig. 3.5) around which the metals to evaporate (Ni 0.5 mm dia. Pluratronic$^{\textregistered}$ 99.999% and Pd 0.25 mm dia. Goodfellow 99.99%) are rolled. The tungsten wire is spot-welded on the electrodes of the metal evaporator to insure a good electrical contact. The electrodes initially made of copper had to be changed to stainless steel as the welding between copper and tungsten was not strong enough and had to be repaired regularly. The filaments can then be resistibly heated with a power supply (ELV SPS9040M, 40V 25A) until evaporation is detected with a quartz microbalance. The evaporation rate can be tuned by varying the current flowing in the filaments.

One of the most important components of this UHV system is the sample holder. This device has in fact to fulfill a certain number of requirements in order to allow convenient and efficient working possibilities. The system delivered by the company Dentech did not exhibited the qualities required and was therefore abandoned. Its most important drawback concerned the lack of compatibility between the different chambers. As a matter of fact, separate sample holders had to be used in the different side chambers. It was for example not possible to prepare a catalyst in the PC and to test it later in the high pressure cell reactor with the same sample holder. These limitations were overcome by Fabio Raimondi who developed a complete different system offering a much higher flexibility [79]. The new sample holder can be seen in figure 3.6. The external housing and the back plate are made of stainless steel while the central part where the sample is fixed is made of copper.

Figure 3.6: Picture of the sample holder. Left: top view, center: bottom view, right: inside view with the thermocouple and the heating element on an insulating Macor®washer.

Copper was chosen for its excellent heat conductivity as the central part of the sample holder constitutes an interface between the sample and the cooling and heating elements. Cooling is assured by the contact between the sapphire sphere previously mentioned and the spherical cavity in the back of the central part which can be seen in the bottom view of figure 3.6 and 3.7. The sample can be heated by running a current in a heating element
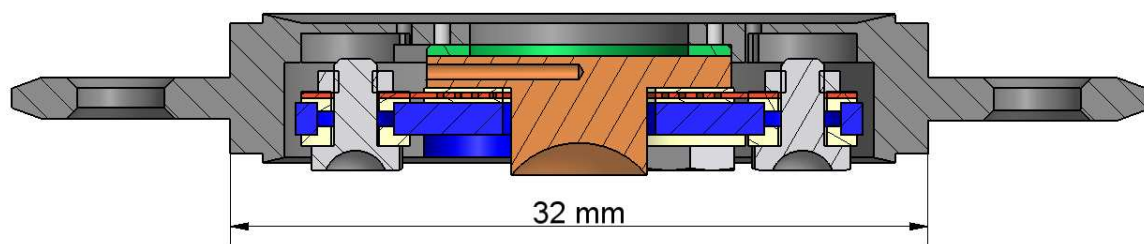
Figure 3.7: Side cut of a sample holder, blue: base plate, red: heating element, yellowish: insulators, brown: central part with cavity for the sapphire sphere.

placed between the back plate and the central part. The heating element has been spark eroded in a molybdenum foil and is fixed with two screws and two bolts which are spot welded together to avoid them to loosen under the effect of the temperature variations. This heating element is represented in red in figure 3.7 and is placed between two Macor® washers to be electrically insulated from the rest of the sample holder. The screws are also insulated from the back plate (blue in fig. 3.7) with two stepped Macor® washers (yellowish in figure 3.7). In order to carry out reproducible experiments and to limit the

power needed to heat the sample, the latter must in intimate contact with the central copper part. This is achieved by pressing the sample installed in the circular cavity on the top of the sample holder against the underlying copper surface with two hooks screwed in the housing of the sample holder. These hooks can be seen in the left picture of figure 3.6. The temperature of the sample is monitored by a K-type thermocouple squeezed in a small channel parallel to the surface of the central copper part, just below the surface. This channel can be seen in figure 3.7. The two extensions on both sides of the housing are used to fix firmly the sample holder in the receiving stations and to hold it in the expandable arm of the distribution chamber during manipulation. Finally, the knife edges present on both sides of the housing can be pressed against copper gaskets in the high pressure reactor in order to isolate the inside of the sample holder containing the catalyst during high pressure experiments. UHV conditions can thus be maintained in the chamber while submitting a sample to pressures up to 10 bars. This offers the nice possibility to analyze a catalyst after reaction without prior exposure to atmosphere. The compact design of the new system prevents also any geometrical limitation in the analysis chamber like interactions with other components coming close to the sample holder during analyzes, like the X-ray gun or the magnetic lens.

The working principle of the quartz crystal microbalance is extensively discussed in section 2.5. This system was partly built in-house with the aim of calibrating the evaporation rate of the metal evaporator and can be seen in figure 3.8. The quartz crystals (5 Mhz) are installed in a water cooled case including electrical contacts which are connected to a Microdot/BNC UHV feedthrough. This feedthrough is then linked to an oscillating circuit (Sycon, OSC-100A) and finally to a frequency counter/thickness rate monitor (Sycon, STM-100). The cooling of the case containing the quartz crystals avoids any temperature rise of the quartz resulting from an exposure to the hot filament of the metal evaporator. Such a temperature increase could lead to erroneous measurements. The quartz crystal microbalance provides a thickness resolution of 1 Å and rate resolution of 0.1 Å/s over a measurement range of 500 kÅ aluminum equivalent.
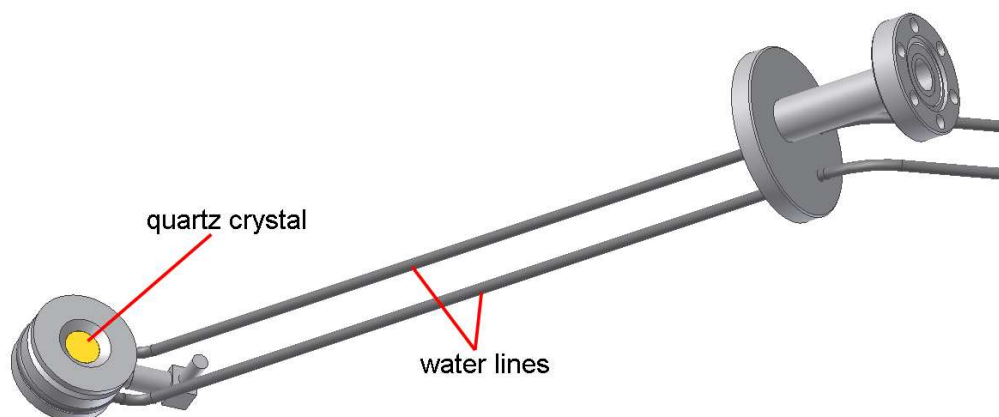
Figure 3.8: Drawing of the quartz crystal microbalance (QCM).

3.1.7   The gas distribution system

The gas distribution system is depicted in figure 3.9. All valves, tubing and other components are made of stainless steel. The gas flow rate is determined by four Bronkhorst mass flow controllers (F-200D-FA-33-V) connected to a Bronkhorst readout system (E-5752, 2 channels). The gas system contains seven distinct outlets. The first one goes to an electronic bubble flow meter which can be used for the calibration of the mass flow controllers. The second and third one are connected to a Leybold scroll pump (SC 5D) for the evacuation of the gas lines. Number four is going to a pressure regulator (Bronkhorst P-702C-FA-33-V) used for maintaining a constant pressure in the lines. This is important in order to avoid pressure variations in the chambers during experiments. Outlets five and six are connected to the high pressure reactor and preparation chamber respectively. Number 7 corresponds to the exhaust and is used for flushing the lines. The pressure in the system is monitored by a manometer and can be tuned with the pressure regulator. The different gases are introduced in the preparation chamber by the mean of three leak valves (Dunyway, VLVE-1000). Two of them can be used with the gas distribution system described above and the third one can be connected to a separate gas supply for more flexibility.
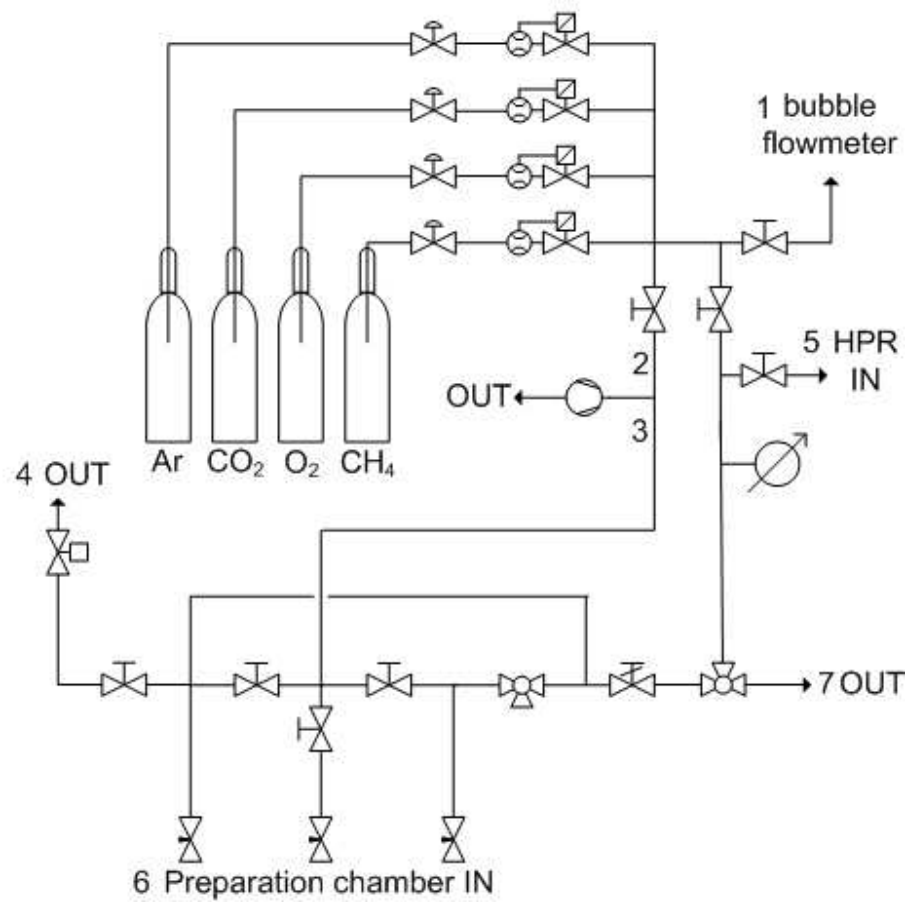
Figure 3.9: Schematic of the gas distribution system

Chapter 4

Preparation and characterization of Ni-Pd/γ-Al$_2$O$_3$ model catalysts

4.1 Introduction

It is well known that many crucial properties of heterogeneous catalysts like activity, selectivity or stability are not only influenced by the absolute composition but also by structural and electronic properties. Typical high surface area industrial catalysts are very complex materials with usually a poorly defined surface and a large distribution of crystallite sizes. As a matter of fact, standard preparation techniques like impregnation or co-precipitation do not permit a good control of the catalysts morphology. This makes the study of the influence of the surface composition and morphology on the catalyst performance rather complicated. Moreover, the application of UHV based surface sensitive techniques like X-ray photoelectron spectroscopy (XPS) or Auger-electron spectroscopy (AES) is limited on limited on such materials. Other methods such as atomic force microscopy (AFM) and spectroscopic ellipsometry (SE) are completely incompatible with commercial catalysts. The reasons explaining these limitations ensue from two main problems. The first one concerns some intrinsic properties of industrial catalysts like their high surface area and lack of electrical conductivity. The high surface area is not limiting in itself but implies a rough surface and inconvenient introduction of the sample into UHV due to extensive outgassing. The second problem concerns the data interpretation of surface-sensitive techniques like

XPS or AES which can be questionable due to the presence of surface contaminants or heterogeneities.

In order to allow the unlimited application of surface sensitive characterization methods for the detailed study of structural, compositional and electronic properties, well-defined single crystals have been used for many decades. Catalysts have been modeled by particular crystal planes expected to be present in the high surface area industrial analogs in order to understand catalytic processes at an atomic scale. Metallic single crystals offer the advantage of an excellent electrical conductivity and the relative simplicity of these systems gives access to some unambiguous information about the catalytic properties of the active sites present. In this way, surface science has gathered a tremendous amount of data about structural and electronic properties of surfaces, dynamics of clean and adsorbate covered surfaces and surface processes. Even if this approach has been successful in a number of cases like the most well known Haber-Bosch process, it is however questionable as it overlooks some crucial aspects of heterogeneous catalysis like the size of the active particles [80][81] and their interaction with the substrate [82][83]. It has been shown that these effects have a dramatic influence on the available active sites and the electronic properties and therefore on the activity and selectivity of catalysts [84]. As a consequence, the resulting understanding of surfaces and surface processes does not automatically translate into a good understanding of heterogeneous catalysts. Progress in that field has been limited mainly by two big obstacles known as the **pressure and material gap** or **complexity gap**. As a matter of fact, the big difference of pressure between UHV experiments and industrial reactions and especially the contrast between the complexity of industrial catalysts and single crystal are not easy to bridge.

In order to circumvent the above mentioned limitations or at least to reduce the complexity gap, the "thin film model catalysts" approach has been applied in this work. The principle of this technique is to study the catalytic activity of metal nanoparticles deposited on a thin oxide film grown on a conductive substrate. These catalysts offer an excellent electrical and thermal conductivity due to the relatively low thickness of the oxide film (1-100 nm) and its intimate contact with the substrate [85]. In fact, electrons can easily cross this oxide layer by tunneling, thus eliminating charging problems inherent to the application of electron spectroscopies. In addition, as the oxide film is very flat, model cat-

alysts are also suitable to surface imaging techniques like atomic force microscopy (AFM), scanning tunneling microcopy (STM) and spectroscopic ellipsometry (SE). A convenient and common method to deposit the catalytically active metal particles on the oxide film is physical vapor deposition (PVD) [86]. As it will be shown in the present chapter, this relatively simple technique allows a certain control of the particle growth like the growth mode, cluster diameter or size by tuning parameters like the amount of deposited metal, the evaporation rate, or the substrate temperature during evaporation [87][88][**?**].

The "thin film model catalysts" approach is considered as one of the most successful techniques in research as it combines the physical and chemical properties of industrial catalysts with the unlimited application of the surface sensitive analysis techniques mentioned previously. Thin film model catalysts constitute a very exciting tool to establish relationships between atomic level physical and chemical properties and the observed catalytic behavior. As a matter of fact, the oxide film are usually polycrystalline with inter-grain boundaries and defects, making them similar to industrial supports. Studies have confirmed that model catalysts exhibit comparable properties to their industrial analogues [89] and they have already been applied successfully by many research groups [90][91].

This chapter addresses the preparation and characterization of Ni-Pd/$\gamma - Al_2O_3/Si$ model catalysts which will be used further in combination with the excimer lamp for the evaluation of the VUV irradiation effect. The substrates are made of a conducting silicon (100) wafer on which 10 nm of γ-Al$_2O_3$ have been previously deposited. Aluminum oxide has been chosen because of its suitability to be used at industrial scale and its actual common application in a variety of large scale processes [92][93]. Nickel was chosen as a starting metal as it is known to be active on the C-H bonds of methane and it is the main constituent of catalysts used in some major industrial processes like the steam reforming of methane (SRM). Palladium was included in various amount to different catalysts in order to see if a possible "tuning" of the activity could be observed. Palladium is an interesting candidate as it is a key component of the main hydrogenation catalysts [94][95][96] and according to Norskov's calculations should form stable alloys with nickel. This is important in order to assure a good stability of the active particles, avoiding for example segregation problems [97][98].

The preparation of the $\gamma - Al_2O_3/Si$ substrates can be achieved by a variety of methods

like electron beam evaporation [99], RF and DC magnetron sputtering [100][101], sol-gel techniques [102], pulsed laser deposition [103], chemical vapor deposition [104][105] or spray pyrolysis [106]. Due to the relatively high number of samples necessary and the associated time investment, it was decided that the most effective way of producing our substrates is DC magnetron sputtering. The procedure has been reported in the literature and results in a stoichiometric thin gamma alumina film upon thermal treatment [107][108]. This technique offers the advantage of a high throughput and an excellent purity as no chemical precursors are required. The final metal addition is then achieved by physical vapor deposition of palladium and nickel over the cleaned substrates. This chapter deals with the preparation and characterization of the $\gamma - Al_2O_3/Si$ substrates as well as of the bimetallic catalysts. Detailed information about the composition, structure and morphology from XPS, AES, SE and AFM will be presented.

4.2   Experimental

The $\gamma - Al_2O_3/Si$ substrates were prepared in the laboratory for neutron scattering at the Paul Scherrer Institut by M. Horisberger. 10 nm thick films of aluminum oxide were deposited on a 10 cm diameter Si(100) wafer by argon sputtering of an aluminum target in a Leybold Z600 DC magnetron sputtering apparatus. The partial pressures of argon and oxygen during the deposition were $3.2 \cdot 10^{-3}$ mbar. A detailed description of the working principle of magnetron sputtering can be found elsewhere [109]. The aluminum oxide deposition rate of 0.25 nm/s was determined with a quartz crystal microbalance. After the coating process, the silicon wafers were cut into 7x7 mm square samples fitting into the 10 mm diameter cavity of the sample holders. The samples were than introduced into vacuum and flashed to 573 K in order to desorb most of the adsorbed gases. In a subsequent step, they were sputtered with the Ar-ion sputter gun described in section 3.1.6 at 1 keV (10 μA ion current) in 10^{-5} mbar of Ar and finally annealed 20 minutes in $5 \cdot 10^{-6}$ mbar oxygen. At the end of the annealing time, the sample was cooled and the oxygen pressure maintained until the substrate temperature decreased below 373 K.

The metal evaporator used to deposit nickel and palladium on the $\gamma - Al_2O_3/Si$ is described in section 3.1.6. The influence of the evaporation rate will be discussed in the

present chapter. The pressure in the preparation chamber during the deposition process did not exceed $3 \cdot 10^{-9}$ mbar.

XPS analyses were performed with the VG Escalab 250 spectrometer described in section 3.1.5. For most of the experiments, the monochromatic Al Kα source was used in "Large Area XL" mode corresponding to a spot size of about 1 mm^2. The hemispherical analyzer was operated in the constant pass energy mode with an energy of 20 eV for detailed regions and 50 eV for survey spectra. Quantification was based on the cross sections calculated by Scofield [45] and the peak areas were determined with the software CasaXPS Release 2.3.13.

Auger analyses were carried out in the LEED chamber (ErLEED 3000D) described in section 3.1.4 which is equipped with a 4 grids optics. By applying suitable voltages to the different grids, this optics can be used as an electron energy analyzer called retarding field analyzer (RFA). The electron gun is equipped with an Iridium filament and operated at 3000 eV resulting in a beam current of 59 μA. Auger spectra were recorded with the RFA-PC software in combination with the ErLEED 3000D power supply via a RS232 interface. Quantification was carried out with the sensitivity factors from Davis [53].

AFM measurements were carried out in tapping mode on a Digital Instrument Nanoscope Extended Multimode Microscope. Silicon tips from Micromasch model NCS15/AIBS were used. These tips have a full tip cone angle smaller than 30° and a radius of curvature <10 nm.

Spectroscopic ellipsometry measurements were performed ex-situ at photon energies between 2.2 and 3.7 eV. The ellipsometer is a MOSS ES 4G SOPRA and uses a xenon lamp with a power of 75 W which irradiates the sample at 70°. The reflected beam is analyzed by a double monochromator scanning the spectral range by intervals of 0.5 eV. The resulting curves $\tan(\Psi)$ and $\cos(\Delta)$ were treated with the software ELLI which allows to fit the experimental data by linear regression analysis (LRA). A multilayer interface model consisting of substances with known parameters was established for the analysis. The model was then compared to the experimental data and a limited number of parameters like the film thickness can be determined.

4.3   Results and discussion

4.3.1   Characterization of the γ-Al$_2$O$_3$ substrates

4.3.1.1   Substrates cleaning and AES/XPS characterization

An XPS spectrum of an "as prepared" $\gamma - Al_2O_3/Si$ substrate is shown in figure 4.1. Only
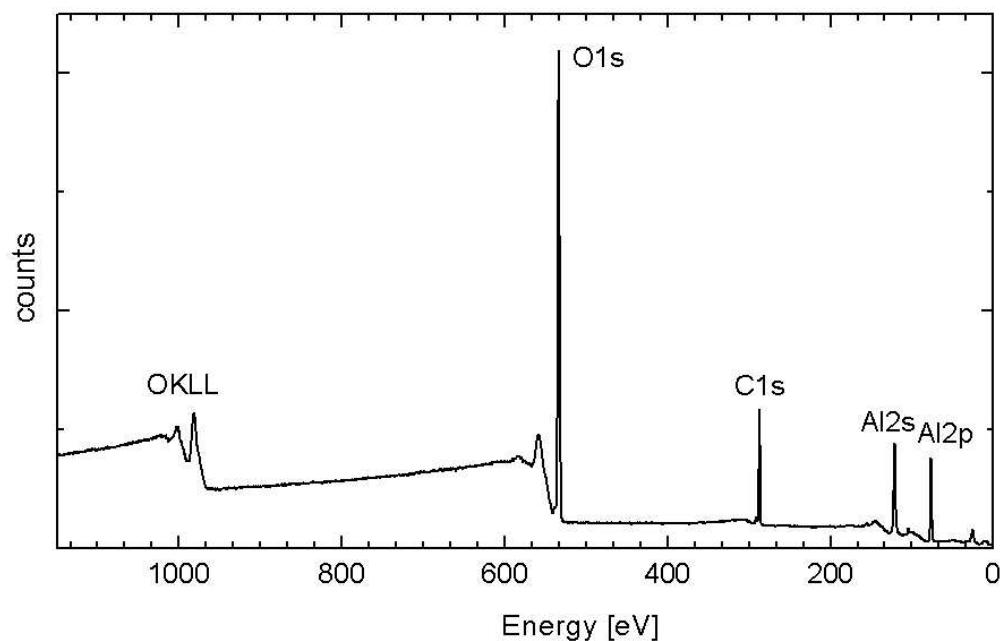
Figure 4.1: XPS spectrum of a $\gamma - Al_2O_3/Si$ substrate.

three components can be seen on this spectrum which are carbon, oxygen and aluminum. The binding energy of the aluminum 2p peak is 74.2 eV, which is reported in the literature to correspond to γ-Al$_2$O$_3$ [110]. The absence of a silicon peak is an indication that the aluminum oxide layer is free of holes or cracks. The relatively intense carbon peak indicates a surface contamination resulting from the storage in air of the substrates. After being introduced into vacuum, the samples were first flashed to 573 K in order to desorb the gases adsorbed on the aluminum oxide layer but also on the sample holder. This avoids heavy outgassing during subsequent cleaning steps and removes already an important part of the carbon contamination as shown in table 4.1. As a matter of fact, the XPS carbon signal was halved upon this thermal treatment. In order to remove the remaining contamination from

Table 4.1: Surface concentration in atomic % of a $\gamma - Al_2O_3/Si$ substrate before and after a temperature flash.

[at %]	C1s	O1s	Al2p
as prepared	19.5	45.2	35.3
flashed	9.4	51.4	39.2

the surface, the samples were then sputtered one minute with Ar as described in section 4.2. In spite of the mild etching conditions applied, some oxygen atoms may be removed from the oxide structure resulting in a non-stoichiometric surface. These substrates were then annealed at 873 K during 30 minutes in $5 \cdot 10^{-6}$ mbar of oxygen to recover a stoichiometric surface but also to oxidize possible remains of carbon. Figure 4.2 shows the XPS spectrum of a $\gamma - Al_2O_3/Si$ substrate after sputtering and annealing. A dramatic decrease of the carbon signal together with the appearance of two small features at 242 and 320 eV can be observed. The peaks at 242 and 320 eV are attributed to argon atoms embedded into the aluminum oxide consequently to the sputtering process . This sputtering/annealing cycle was repeated twice and the surface was analyzed between each cycle with XPS and AES. The resulting concentration can be seen in figure 4.3 for two independent samples A and B. It appears clearly on this figure that AES is much more sensitive to carbon contamination than XPS. As a matter of fact, the carbon level of the "as prepared" sample is around 20% in the case of XPS, compared to 60-70% with AES. It drops then directly to almost zero with XPS after the first cleaning step. This is not the case with AES where the carbon concentration decreases progressively to about 10% and finally below 5% after the second cycle. Two reasons can explain this observation, i.e. the penetration depth of the excitation source and the difference of attenuation lengths between Auger and photoelectrons. In fact, the penetration depth of the electron beam used in AES to induce the emission of Auger electrons is around a few nm compared to about 1.3 μm (at 30° incidence) for the X-ray beam used in XPS. As a result, the "emitting volume" is larger in XPS than in AES. In addition, the electrons originating from carbon in AES have a kinetic energy of 275 eV against 1201 eV for XPS. This indicates that the Auger electrons have a lower attenuation
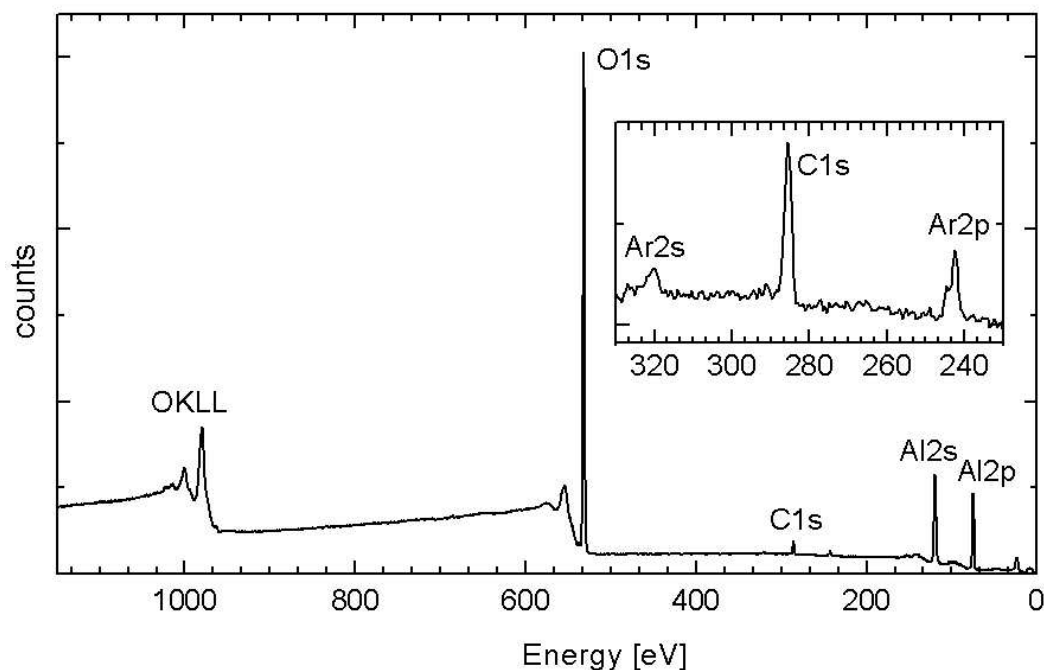
Figure 4.2: XPS spectrum of a $\gamma - Al_2O_3/Si$ substrate after Ar-ion sputtering and annealing.

length than XPS photoelectrons resulting in a higher surface sensitivity. AES was therefore the reference technique in this work for the assessment of the cleanliness of the substrates. Figure 4.4 shows the intensity ratio of the oxygen to the aluminum signal calculated from XPS and AES data. The presented values correspond to the average of the ratios obtained for samples A and B previously mentioned. The O/Al ratio of Auger signals decrease slightly from 0.65 to 0.59 with the successive cleaning cycles, very close to the expected value of 0.6. This decrease cannot be explained by the lower effective attenuation length of the oxygen signal compared to Al. In such a case, the oxygen signal would be more damped by a surface contamination and therefore, the resulting O/Al ratio should increase with a cleaner surface. A possible explanation for the observed behavior could be the presence of oxygen containing carbonaceous compounds progressively removed with the cleaning cycles. More likely, the surface of the "as prepared" substrate might be partly covered with OH groups removed during the cleaning cycles and responsible for the observed decrease of
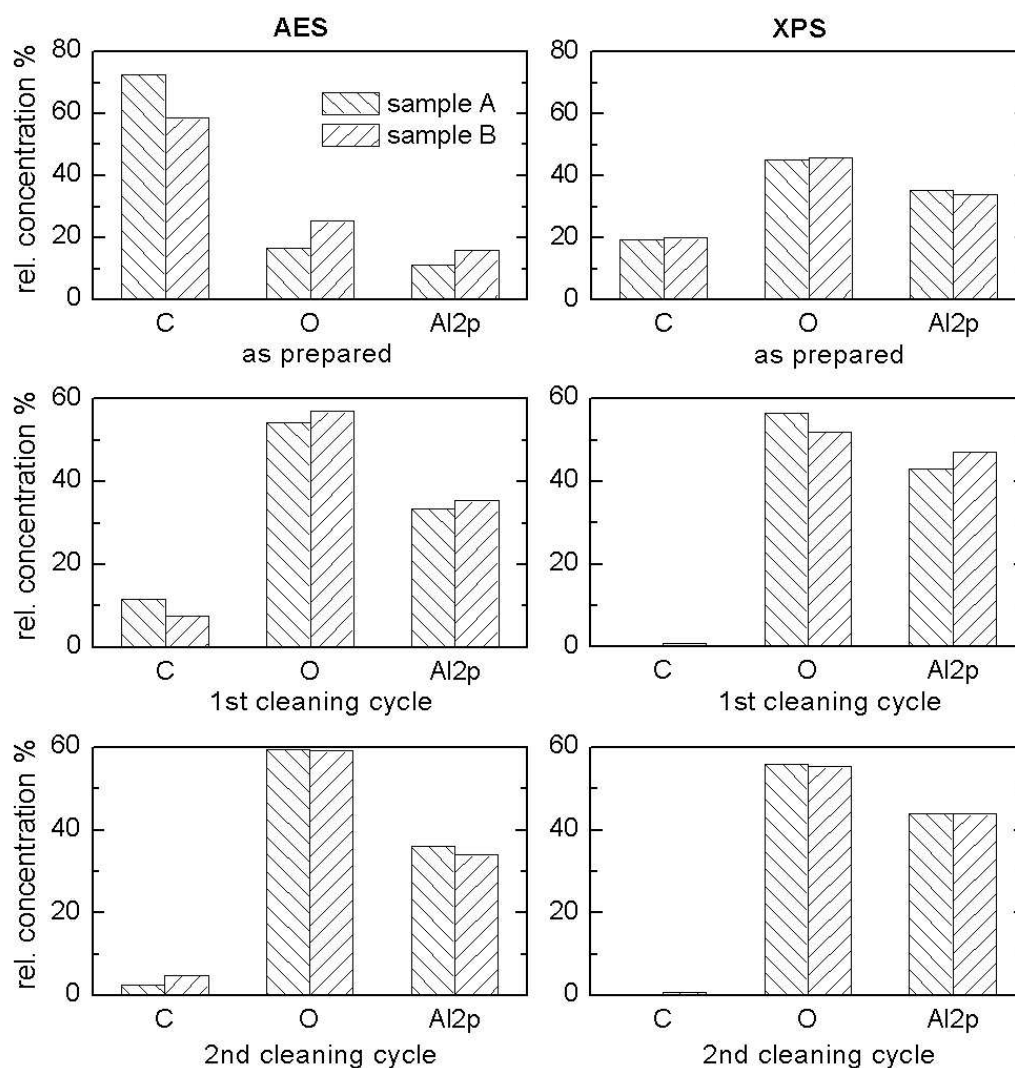
Figure 4.3: Evolution of the relative surface concentration of $\gamma - Al_2O_3/Si$ substrates after successive cleaning cycles: comparison between XPS and AES.

the oxygen intensity. This assumption is supported by the fact that the carbon and oxygen peaks seemed to be composed of only one well-defined signal. A surface contamination by oxygen containing carbonaceous species would probably result in different carbon and oxygen features.

The XPS ratios of figure 4.4 differ significantly from the expected value of 0.6 reflecting a 2:3 stoichiometry of Al_2O_3. The differences observed could result from a depletion of
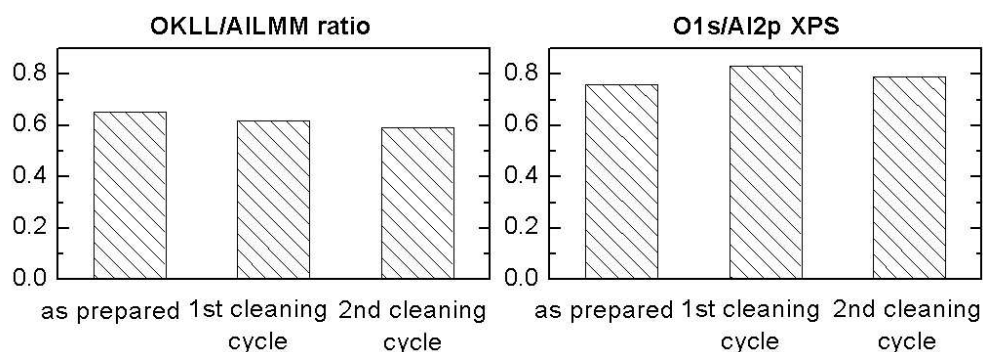
Figure 4.4: Comparison between AES and XPS of the O/Al signal intensity ratio of $\gamma - Al_2O_3/Si$ substrates after successive cleaning cycles.

aluminum on the surface or from an excess of oxygen. A sub-stoichiometric concentration of aluminum might be a consequence of the sputtering. This is however unlikely as oxygen should be removed faster due to its lower atomic mass. In addition, this effect would take place on the top layers of the surface and should be more visible in AES than in XPS analyses, which is not the case here. The same argument is valid in the case of an excess of oxygen on the surface, as in the form of OH groups. However, the measured ratios of 0.75-0.8 do not necessarily indicate a non-stoichiometric surface. This might come from to the large uncertainties involved in the conversion of XPS signals to surface concentration. The intensity of XPS signals is converted to surface concentrations with equation 2.8. Some parameters involved in this equation contain relatively large uncertainties like for example the photoelectric cross section, which is derived from theoretical calculations. As discussed in section 2.1, their use might introduce significant errors in the calculated surface composition. The same is valid for the attenuation lengths which are very difficult to determine accurately and may vary with the surface composition or crystal structure of the sample. These considerations imply therefore that the XPS data presented in figure 4.4 could be affected by a significant systematic error and may therefore not be representative of the actual surface stoichiometry. AES data seem to support this fact as they indicate the expected Al/O concentration ratio of 0.6. This point does however not call into question the accurate evaluation of relative concentration changes with XPS as they are no longer subject to systematic errors.

4.3.1.2 AFM

A 1x1 μm AFM picture of a cleaned $\gamma - Al_2O_3/Si$ substrate is shown in figure 4.5. No clear structures can be distinguished on this picture and the associated root mean square roughness of 0.68 Å indicates a very flat surface. This point is of high importance as it implies that the influence of the substrate morphology can be neglected in further studies of the metal films structure.
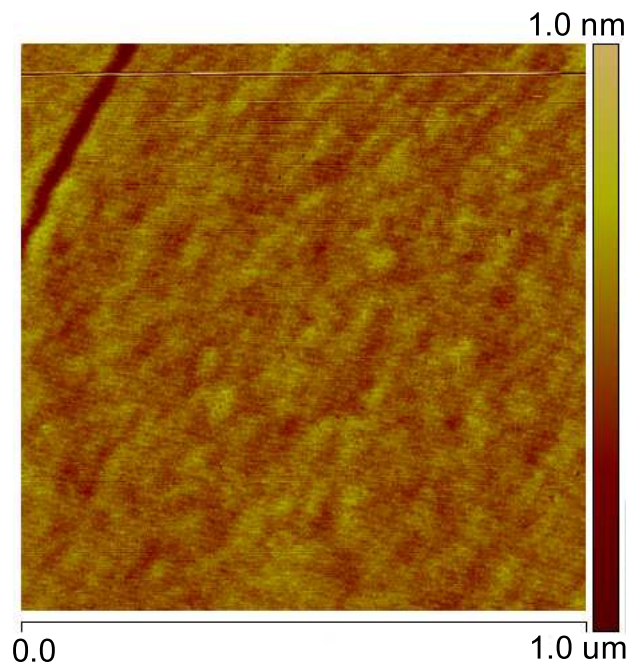
Figure 4.5: AFM picture of the surface of a $\gamma - Al_2O_3/Si$ substrate after UHV cleaning.

4.3.1.3 SE

The cleaned substrates were analyzed by spectroscopic ellipsometry. Values of $\tan(\Psi)$ and $\cos(\Delta)$ have been determined for a spectral range from 2.2 to 3.7 eV with a light source irradiating the sample at an incidence angle of 70°. Measurements together with a fit of $\tan(\Psi)$ and $\cos(\Delta)$ can be seen in figure 4.6 and 4.7 respectively. The data were fitted with a model assuming an aluminum oxide layer deposited over a silicon. The fit was performed with the computer program ELLI supplied by the manufacturer of the ellipsometer.
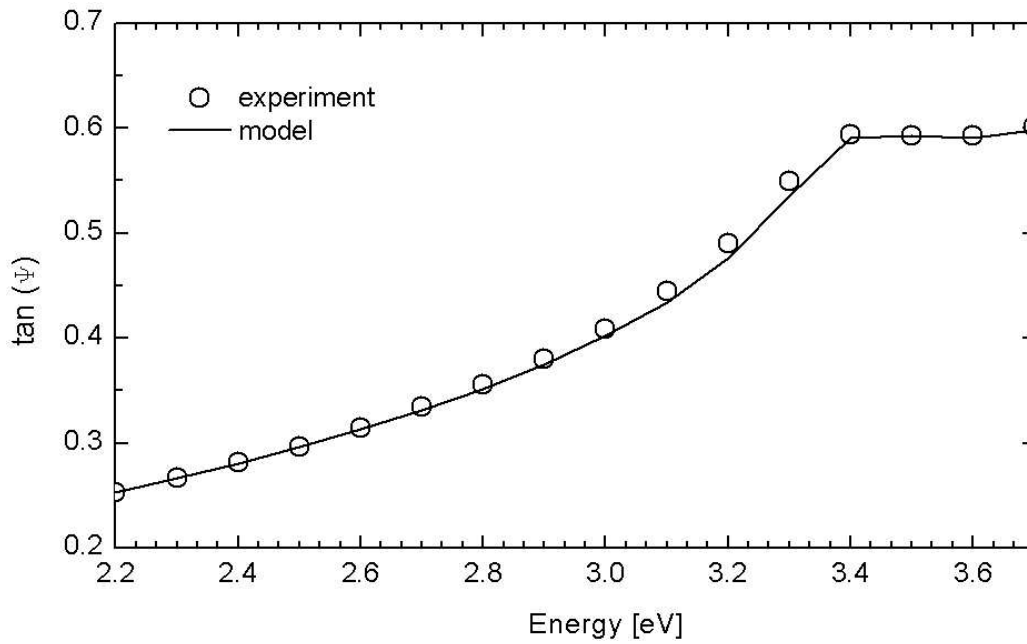
Figure 4.6: $\tan(\Psi)$ values of a cleaned $\gamma - Al_2O_3/Si$ substrate obtained by SE and the corresponding fit.

This software uses a linear regression procedure based on the Bruggeman effective medium theory. As shown in figures 4.6 and 4.7, the model giving access to the thickness of the alumina layer fits the measurements very well. The validity of the measurements presented here is supported by the low roughness found by AFM (see section 4.3.1.2) which fulfills a requirement of ellipsometry being that surface roughness $\ll$ wavelength of the ellipsometer. The thickness of the alumina film was found to be 14.4 ± 0.1 nm. The low error of the film thickness is a consequence of the small standard deviation of the model curve compared to the experimental data. The value obtained is slightly higher than the thickness determined with the QCM during the aluminum oxide film deposition which was 10 ± 0.5 nm. In order to clarify the origin of the difference observed between the QCM and the SE measurements, a depth profile was carried out on a nickel catalyst.
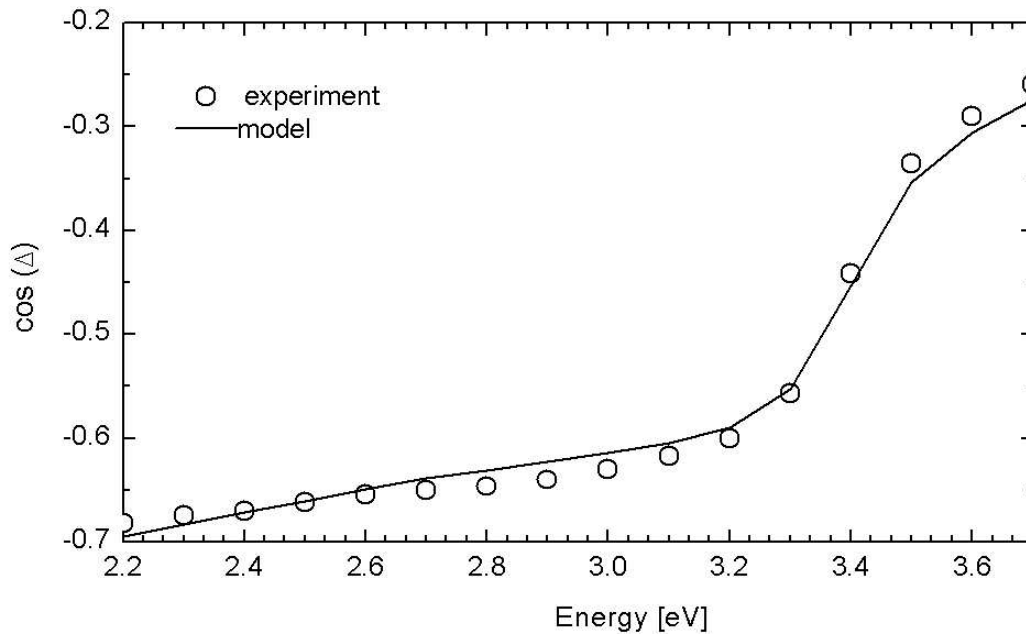
Figure 4.7: $\cos(\Delta)$ values of a cleaned $\gamma - Al_2O_3/Si$ substrate obtained by SE and the corresponding fit.

4.3.1.4 Depth profile

A depth profile was performed with a catalyst on which a nickel film of 3 nanometers thickness had been deposited by evaporation over a $\gamma - Al_2O_3/Si$ substrate. This experiment was carried out in the analysis chamber with an argon ion beam energy of 3 keV and a pressure of 10^{-7} mbar. The present analysis will be treated qualitatively as a quantitative interpretation requires a proper calibration of the sputter rate with standard samples which should reflect the composition of our substrates. Such a calibration is going beyond the scope of this work and may not be reliable for complex samples like ours [40]. As a matter of fact, the accurate determination of the sputter yield is relatively complex and depends on several parameters like the chemical nature and electronic state of the components included in the film. Our samples have a layered structure composed of heavy, light and intermediate-weight elements such as nickel, oxygen and aluminum/silicon respectively. Light materials are subject to preferential sputtering in multi-components samples leading

to surface roughening and a possible local enrichment of heavy atoms. This would make a quantitative analysis of our samples questionable.

The atomic concentrations after each sputtering step is shown in figure 4.8. Initially, a
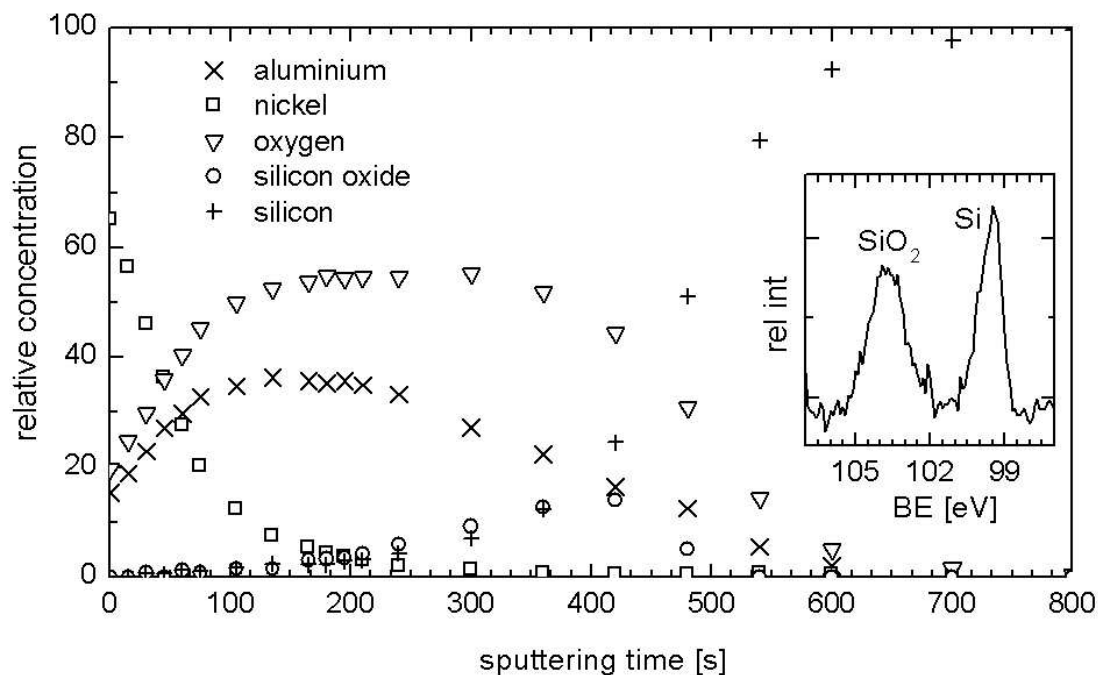
Figure 4.8: Evolution of the concentration profiles of a $(3\ nm)Ni/(10\ nm)\gamma$-Al_2O_3/Si catalyst with the sputtering time.

steep decrease of the nickel concentration combined with an increase of both aluminum and oxygen can be observed. This corresponds to the expected removal of the nickel layer. It is noteworthy that the oxygen concentration remains constant from about 120 to 350 s, while the intensity of the aluminum signal starts declining already before 250 s. In an ideal case, the ratio of aluminum to oxygen should stay constant all along the depth profile. In practice, this ratio is rather expected to increase slightly as a consequence of preferential sputtering due to the lower atomic mass of oxygen atoms compared to aluminum, which is the opposite of the actual behavior. A careful analysis of figure 4.8 reveals a possible reason for this unexpected behavior. As a matter of fact, a layer of SiO_2 represented by circles can be observed at the interface between aluminum oxide and silicon. As shown in

the inset of figure 4.8, silicon can be easily distinguished from silicon oxide by XPS as their respective 2p signals appear on the spectrum at 99.5 and 103.5 eV respectively.

Such an oxide layer is to be expected as the magnetron sputtering process took place in an oxygen atmosphere. The native oxide film should however not be thicker than 1-2 nanometers [111][112]. In the present case, this layer spreads over 150 s between the inflexion points of the feature corresponding to SiO_2. By comparison, the peak of the 3 nm nickel layer has a width of about 100 s. Assuming an equivalent sputter yield between nickel and silicon oxide, the SiO_2 layer would have a thickness of approximately 4.5 nm. Similarly, the total oxide layer including Al_2O_3 and SiO_2 which goes from about 50 to 500 s would corresponds to a thickness of 13.5 nm. As mentioned previously, this value must be considered with great care due to the approximations made for its calculation. It remains that this value is very close to the oxide layer thickness found by spectroscopic ellipsometry. As a matter of fact, Al_2O_3 and SiO_2 have very close optical properties which make spectroscopic ellipsometry unable to distinguish between them. It is therefore likely that the 14.1 nm measured correspond to the total oxide thickness including silicon and aluminum oxide. The origin of this thick interfacial silicon layer has already been observed in the literature and the mechanism of formation is still debated [102]. Gopireddy et al. suggested the diffusion of an excess of oxygen contained in the alumina film followed by a reaction at the Al_2O_3/Si interface to form SiO_2 [113]. Krug et al. proposed a different mechanism based on the diffusion of oxygen trough the alumina film and reaction at the alumina/silicon interface. Oxidized silicon occupies a larger volume and generates interstitial Si which is prone to move [114]. It has been shown that interstitial silicon cannot be trapped in SiO_2 [115] and diffuses therefore in the sample. However, when present in the alumina layer, it can displace aluminum atoms as the formation of silicon oxide is favored over the formation of aluminum oxide. This implies therefore that some silicon is fixed in the alumina film and aluminum and oxygen move to the silicon wafer [116]. If we look at the depth profile, a diffusion of oxygen following the mechanism proposed by Gopireddy et al. would result in a well defined alumina/silica/wafer layers which is not the case here. As a matter of fact, the SiO_2 signal is very broad and characterized by a low intensity, indicating diffuse boundaries. In addition, it seems that the silicon oxide layer is "included" in the alumina film as the intensity of aluminum is always higher than the intensity of the

silicon signal originating from SiO_2. Our observations seem therefore to corroborate the mechanism proposed by Krug et al.. At the same time, it confirms also the spectroscopic ellipsometry data and the film thickness determined with the quartz crystal microbalance during the aluminum oxide deposition. The phenomenon itself is not a problem for the present work as no silicon can be detected on the $\gamma - Al_2O_3/Si$ surface and the substrates are still conductive in spite of the additional oxide layer.

4.3.2 Characterization of the Ni/γ-Al$_2$O$_3$/Si catalysts

4.3.2.1 SE

In order to check the accuracy of the evaporation rate determined with the quartz crystal microbalance, various amounts of nickel were deposited on cleaned substrates at room temperature. This step was of course essential for reliable interpretation of future experiments. The experimental points of $\cos(\Delta)$ and $\tan(\Psi)$ were fitted with a 3 layers model including Ni/Al$_2$O$_3$/Si, nickel being on top and silicon below the nickel and aluminum oxide layers. The layer thickness determined experimentally with the QCM and SE measurements can be compared in table 4.2. The correlation between the values presented is remarkably good and provides therefore a solid base for a more detailed characterization of the catalysts.

Table 4.2: Comparison between the thickness in nm of the nickel layer obtained by QCM and SE for two independent samples.

[nm]	sample 1	sample 2
QCM	2.0	7.0
SE	1.9±0.5	6.9±1.2

4.3.2.2 AFM

In order to find suitable preparation conditions for our catalysts, nickel was evaporated on UHV cleaned $\gamma - Al_2O_3/Si$ substrates which were subsequently analyzed by AFM. Considering the goal of preparing catalysts, it is desirable to form metal clusters on the

substrates, not only to increase the active surface area but also to enhanced the catalytic properties. As a matter of fact, irregular surfaces presenting defects are expected to be more active than well ordered systems. Different theoretical growth modes illustrated in figure 4.9 have been suggested in the literature [117][118][119]. The "Volmer-Weber" (VW)
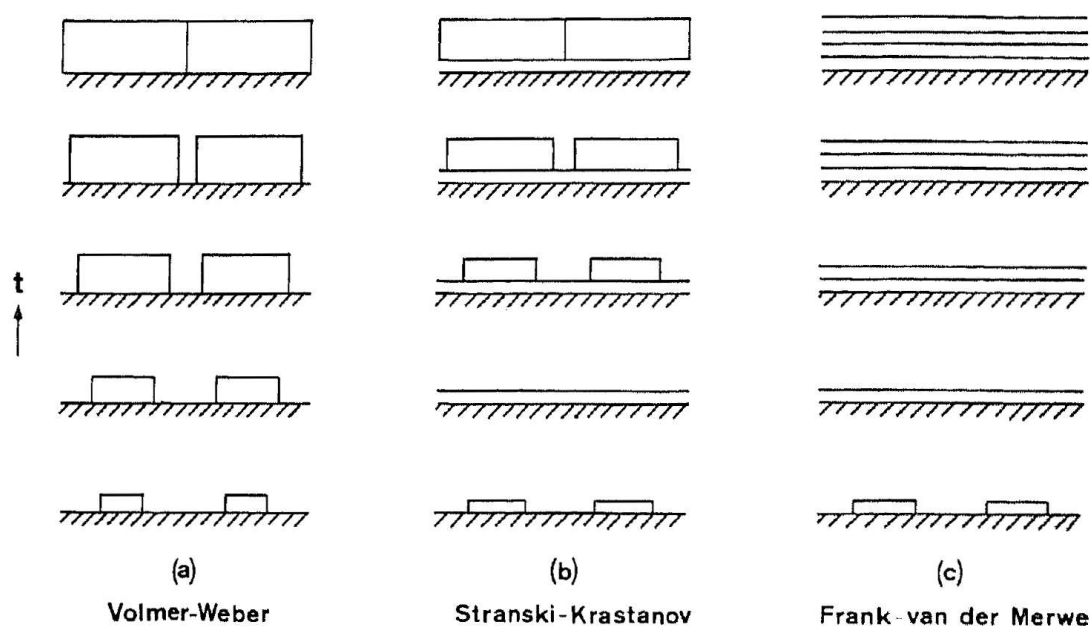
Figure 4.9: Illustration of the different growth mechanisms.

growth mode corresponds to the immediate formation of metal clusters; the "Frank-van der Merwe" (FM) growth mode describes a layer-by-layer growth while "Stranski-Krastanov" (SK) is characterized by a transition from an initial layer-by-layer growth to a consecutive three dimensional cluster formation at a critical film thickness. Other mechanisms have been suggested like the one of Jacobs et al. [120]. They describe a complex growth process of Ni on Al_2O_3 where nickel adsorbs on the strongest binding sites of the alumina support. Ni centers are thought to be the base for the subsequent growth of nickel particles. This scheme would however correspond to a "Volmer-Weber" or "Stranski-Krastanov" growth mode mentioned previously. The model adopted by a given system depends both on thermodynamic and kinetic aspects. Neglecting the shape and size dependence of a surface,

the quantity which determines the growth mode can be written in a simplified form as:

$$\Delta = \sigma_f + \sigma_i - \sigma_s \tag{4.1}$$

where σ_f and σ_s stand for the specific surface free energy of the film and the substrate and σ_i corresponds the specific interfacial energy. The Volmer-Weber growth mode is favored when $\Delta > 0$ and SK/FM when $\Delta < 0$. In the FM growth mode, the condition must be fulfilled for each layer, which is the case if the film and the substrate are similar, meaning $\sigma_f \approx \sigma_s$ and $\sigma_i \approx 0$. This condition may, however, only be fulfilled for one or few monolayers leading to a transition from a layer by layer growth to the formation of clusters corresponding thus to a SK growth mode. A prediction of the deposition mechanism is very difficult as the "bulk" surface free energy does not constitute a good approximation for a monolayer which can be strongly influenced by the interaction with the substrate. In addition, the interfacial energy is difficult to determine precisely, even in the case of bulk crystals. Furthermore, the growth mode criteria described above corresponds to the equilibrium state. In practice, the diffusion of the surface species is often too low or the surface reconstruction activation energy too high to reach the equilibrium state [121]. Pseudo growth modes may result from such situations which can be identified by studying the film morphology at different temperatures. The paper of C. Argile et al. describes extensively this problem and also includes a catalogue of the systems studied between 1968 and 1988 [122]. A consequence of the above mentioned considerations is that a determination of the growth mechanism for our specific system was required.

Films were therefore deposited initially at room temperature with a metal evaporation rate of 1.5 Å/min. The AFM analysis of these samples did not reveal the presence of any cluster, the sample surface appeared to be relatively flat in spite of the fact that the presence of nickel was confirmed by XPS measurements. Several combinations of deposition rates, from 0.4 to 2 Å/min, and substrate temperatures, between 273 and 873 K, have been tested. A general observation resulting from these experiments is that when the substrate temperature during the deposition is too low and/or the evaporation rate is too high, no clusters are formed on $\gamma - Al_2O_3/Si$. However, as with certain combinations of substrate temperature and evaporation rate nickel clusters could be observed in our system, a flat surface corresponds therefore to a "pseudo Volmer-Weber" growth mode. At temperatures

above 823 K, the surface morphology appeared "chaotic", with a badly defined structure and large particle size distribution. This observation is illustrated in figure 4.10 where 5 nm of nickel have been evaporated on $\gamma - Al_2O_3/Si$ substrates at different temperatures in UHV. Picture a) corresponds to a surface temperature during deposition at 273 K. The surface appears relatively flat here with a roughness of 0.15 nm. On b), corresponding to 623 K, a well-defined cluster structure can be seen together with a roughness of 0.87 nm. It was observed that the higher the amount of nickel evaporated, the less homogeneous
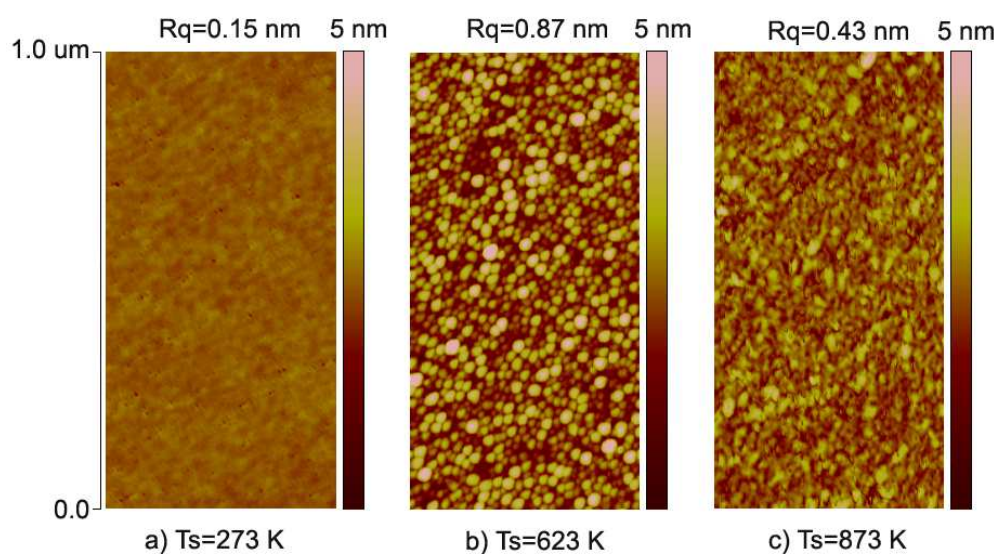
Figure 4.10: Dependence of the surface morphology of $(5 \text{ nm})Ni/\gamma - Al_2O_3/Si$ catalysts with regard to the surface temperature during the evaporation of nickel.

the surface. At higher temperature, the nickel layer formed irregular structures and the surface roughness decreased to 0.43 on c). Qualitatively, the best defined surfaces were obtained at a 623 K. The observed behavior supports the fact previously mentioned that at low temperature, the metal atoms do not diffuse rapidly enough on the surface to adopt the thermodynamically most stable morphology [123]. This is in agreement with thermodynamical data as the surface free energy of a clean Al_2O_3 surface is significantly lower than for a clean Ni surface [124]. A system composed of both nickel and aluminum oxide should therefore expose preferably Al_2O_3 than nickel at or close to the thermodynamic equilibrium.

The size of the metal particles as a function of the amount of nickel evaporated has also been investigated. Pictures a), b), and c) of figure 4.11 show catalysts with nickel films of 1.5, 5 and 7 nanometers thickness. The size of the clusters formed increases with the
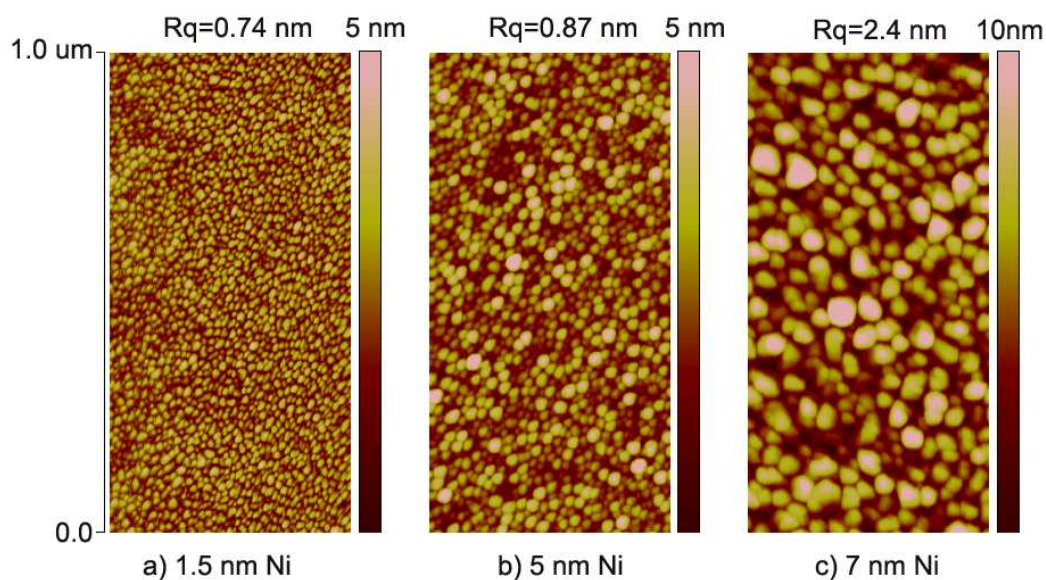
Figure 4.11: Influence of the nickel loading on the surface morphology of $Ni/\gamma - Al_2O_3/Si$ catalysts at 623 K.

average thickness of the nickel film. The growth mechanism is probably a combination of the direct accumulation of nickel atoms reaching the surface and the coalescence of the growing particles. As a matter of fact, it appears that the particle number decreases from a) to c). Additionally, the size distribution increases in parallel with the cluster growth. Picture a) is characterized by well-defined homogeneous particles while the surface of c) shows a wide range of particle sizes and shapes with clusters wider than 50 nm. These large particles have a height of only about 10 nm, which means that they are characterized by a flat island shape with a diameter to height ratio of about 5.

4.3.2.3   XPS

In order to investigate the growth mechanism at low nickel coverage, XPS spectra of a sample were acquired after the deposition of small amounts of metal. Nickel was therefore

evaporated stepwise on a UHV cleaned substrate at 623 K at a rate of 0.75 Å/min by opening and closing the shutter of the metal evaporator. The surface of the sample was analyzed between each deposition step by XPS and the ratio of the intensity of the $Ni2p_{3/2}$ signal over the intensity of Al2p was calculated for each measurement and plotted as a function of the average nickel thickness. These data are represented by circles in figure 4.12.
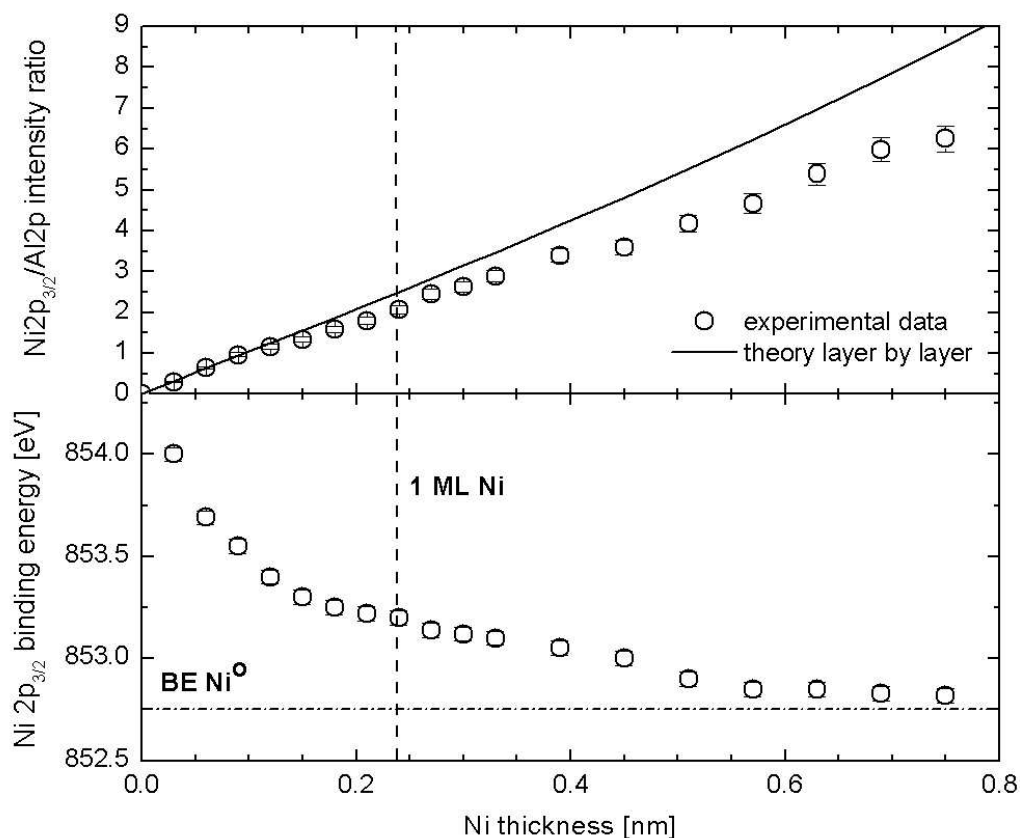
Figure 4.12: Upper panel: Evolution of the ratio of the XPS intensities of the $Ni2p_{3/2}$ signal over the Al2p signal. The dots correspond to experimental measurements and the solid line to the theoretical ratio assuming a layer by layer growth mode. Bottom panel: Evolution of the binding energy of the $Ni2p_{3/2}$ with the average thickness of nickel deposited on the $\gamma - Al_2O_3/Si$ substrate. Nickel was deposited at 623 K.

The dependence of the intensity ratio of Ni2p$_{3/2}$ over Al2p on the thickness of the nickel film d$_{Ni}$ can be described with equation 4.2:

$$\frac{I_{Ni2p_{3/2}}}{I_{Al2p}} = \frac{\sigma_{Ni2p3/2}N_{Ni}T_{Ni2p_{3/2}}}{\sigma_{Al2p}N_{Al}T_{Al2p}} \cdot \frac{\int_0^{d_{Ni}} exp(-\frac{z}{\lambda_{Ni2p_{3/2}/Ni}})dz}{exp(-\frac{d_{Ni}}{\lambda_{Al2p/Ni}})\int_0^{\infty} exp(-\frac{z}{\lambda_{Al2p/Al_2O_3}})dz} \tag{4.2}$$

In this equation, σ is the photoelectric cross section of orbitals 2p$_{3/2}$ and 2p of nickel and aluminum respectively, N is the atomic concentration in atoms/cm^3 and T the transmission function of the considered transition. $\lambda_{Al2p/Ni}$ and $\lambda_{Ni2p_{3/2}/Ni}$ are the effective attenuation lengths of Al2p and Ni2p$_{3/2}$ and are equal to 1.40 and 0.80 nm respectively [125]. Upon integration, equation 4.2 becomes:

$$\frac{I_{Ni2p_{3/2}}}{I_{Al2p}} = \frac{\sigma_{Ni2p_{3/2}}N_{Ni}T_{Ni2p_{3/2}}\lambda_{Ni2p_{3/2}/Ni}}{\sigma_{Al2p}N_{Al}T_{Al2p}\lambda_{Al2p/Al_2O_3}} \cdot \frac{1 - exp(-\frac{d_{Ni}}{\lambda_{Ni2p_{3/2}/Ni}})}{exp(-\frac{d_{Ni}}{\lambda_{Al2p/Ni}})} \tag{4.3}$$

This equation is valid for a uniform nickel layer. At low coverage, that is for values of d$_{Ni}$ lower than 0.1 nm ($\simeq$ 0.4 ML) equation 4.3 can be approximated with equation 4.4:

$$\frac{I_{Ni2p_{3/2}}}{I_{Al2p}} = \frac{\sigma_{Ni2p_{3/2}}N_{Ni}T_{Ni2p_{3/2}}}{\sigma_{Al2p}N_{Al}T_{Al2p}\lambda_{Al2p/Al_2O_3}} \cdot d_{Ni} \tag{4.4}$$

This equation corresponds to a line as the only varying parameter is d$_{Ni}$. The thickness of nickel has been accurately determined with the quartz microbalance and we can therefore fit the first four points of the top graph of figure 4.12 in order to determine the sum of the constant parameters, or slope. As explained in section 2.1, these parameters are not straightforward to determine theoretically and may be subject to a large error, an experimental determination is therefore an advantage. The obtained slope was then re-introduced in equation 4.3 in order to calculate the theoretical value of I$_{Ni2p_{3/2}}$/I$_{Al2p}$ corresponding to a layer by layer growth of the nickel film. This theoretical ratio is represented by the solid line in the upper graph of figure 4.12. On this graph, our experimental data follow as expected the layer by layer growth line up to a Ni thickness of about 0.1 nm. This fact suggests that in the initial phase Ni does not form clusters immediately, but 1D (or possibly 2D) islands. In a second stage, the experimental Ni2p$_{3/2}$/Al$_{2p}$ ratio deviates from the prediction of equation 4.3. This negative deviation can be interpreted as a change in the growth mechanism corresponding to the formation of 3D islands. As a matter of

fact, when nickel atoms land on the substrate, they progressively cover the aluminum oxide, thus attenuating the intensity of its XPS signal by the mechanisms described in section 2.1. When clusters start to be formed, the nickel atoms landing on top of existing nickel islands do not damp the aluminum signal as "efficiently" as in the case of sitting directly on the aluminum oxide. This mechanism attenuates therefore the rate at which γ-Al_2O_3 is covered and consequently the rate at which the $Ni2p_{3/2}$/Al2p ratio increases. This growth mode corresponds therefore to a Stranski-Krastanov growth described in section 4.1, which is in accordance with the findings of Jacobs et al. [120].

Support for the suggested growth mode can be found by considering the binding energy of the XPS nickel signal. As shown on the lower graph of figure 4.12, the binding energy of the $Ni2p_{3/2}$ signal decreases with the increase of the nickel thickness. This change of the binding energy can be divided into three domains. In the initial domain, going from 0 to 0.1 nm, the BE is decreasing sharply from 854 to 853.25 eV. A binding energy of 854 eV corresponds to the published value for NiO [110]. This can be interpreted as single Ni atoms deposited and chemically modified by strong interactions with the oxygen of the support. The decrease of the binding energy can be explained here by changes in the electronic structure of nickel atoms as a result of the growth of 2 dimensional islands on the substrate. From 0.1 to 0.4 nm the slope of the binding energy change decreases and the BE reaches 853 eV. It is interesting to notice that the thickness of 0.1 nm correlates to the deviation in the graph of the $Ni2p_{3/2}$/Al_{2p} ratio of our experimental points from the line corresponding the a layer by layer growth. This may be a consequence of a transition from a two dimensional to a three dimensional growth of the nickel agglomerates which are still not "metallic", but chemically modified. After 0.4 nm, the BE energy decreases slowly towards 852.7 eV corresponding to bulk nickel, indicating a continuous cluster growth and the progressive formation of a band structure typical of bulk Ni. These observations have been subject to theoretical investigations [126] which are in agreement with our data. The interpretation of the dependence of the binding energy on the cluster size or surface coverage is still debated in the literature [127]. It has not been settled yet whether the decrease of binding energy observed is a consequence of the changes in the electronic structure of the metal atoms, known as *initial state effect*, or results from a better screening of the core ionized final state with the increasing particle size known as *final state effect* [86].

4.3.3 Characterization of the Pd/γ-Al$_2$O$_3$ catalysts

4.3.3.1 AFM

Similar experiments to what has been carried out in the case of nickel on γ-Al$_2$O$_3$ have been carried out for Pd. Initially, palladium was evaporated at a rate 1.5 $\mathring{A}$/min at 300 K and the samples were analyzed by AFM. No clusters could be observed at room temperature and the evaporation rate was therefore decreased to 0.8 $\mathring{A}$/min and the substrate temperature was raised successively to 373 and 473 K. This was done to enhance the surface diffusion of palladium atoms possibly resulting in the formation of clusters already observed in the literature for the Pd/$\gamma - Al_2O_3/Si$ system. The samples prepared in the present work at 473 K exhibited a well-defined morphology made of homogeneous clusters. Gillet et al. studied this system at 300 and 600 K and observed an earlier cluster formation at 600 K than at 300 K [128]. They attributed this phenomenon to the enhanced migration of palladium atoms on the surface. This corresponds also to the findings of Atanasova et al. for identical experimental conditions [129]. The formation of clusters is reflected by the drastic increase of the surface roughness as shown in figure 4.13. The lower substrate temperature compared to the nickel system at which the formation of clusters is observed can be explained by a weaker interaction between $\gamma - Al_2O_3/Si$ and Pd than between $\gamma - Al_2O_3/Si$ and Ni. This results in a higher mobility of palladium atoms on the substrate and therefore a faster clusters formation [130].

At higher Pd loading, the same conclusions as for nickel are valid here, that is an increase of both the diameter and the size distribution of the particles resulting from the accumulation of evaporated palladium and coalescence of existing islands [131]. It is interesting to notice that between a layer thickness of 1.5 and 3.5 nm the surface roughness only increases from 0.47 to 0.58. The reason is that at high palladium loading, the particles cover entirely the substrate surface and the clusters seem to grow vertically. The dark regions of picture c) in figure 4.13 do not corresponds any more to a free aluminum oxide surface but to the boundaries between palladium particles. The Pd clusters seem in fact to be squeezed against each other on this picture.
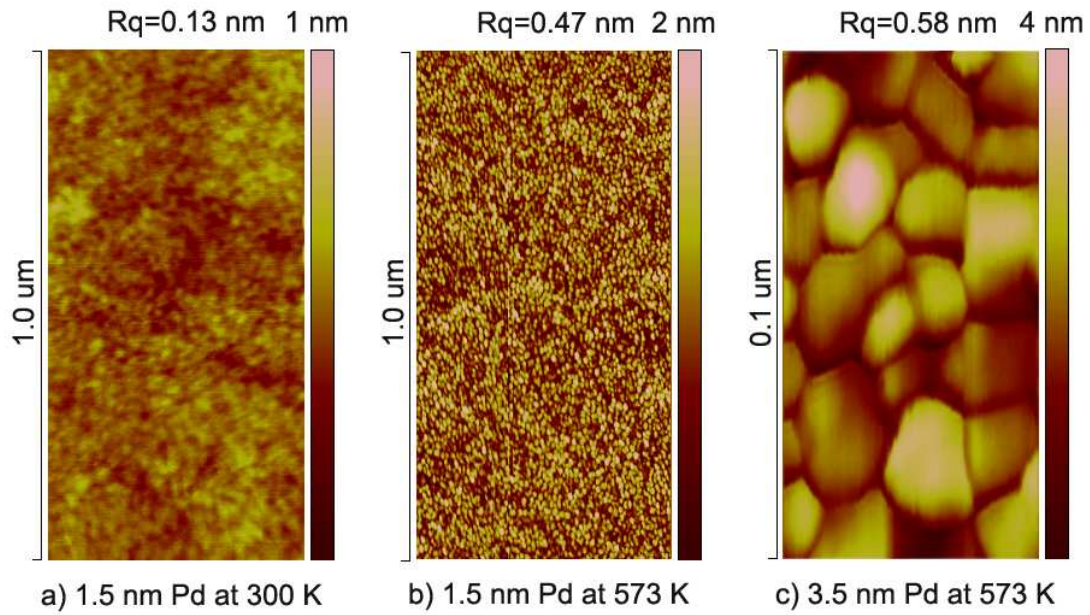
Figure 4.13: Comparison of the surface morphology of three palladium catalysts prepared at different temperatures and with a variable nickel loading.

4.3.3.2   XPS

Palladium was evaporated stepwise on a UHV cleaned $\gamma - Al_2O_3/Si$ substrate, similarly to what has been done in section 4.3.2.3 for nickel, with the aim of investigating the growth mode of palladium at low coverage in our experimental conditions. The evaporation rate of 0.8 Å/min together with a substrate temperature of 473 K determined in section 4.3.2.3 were applied. The ratio of the intensity of $Pd3d_{5/2}$ over Al2p was calculated and corresponds to the circles in the upper graph of figure 4.14. Equation 4.3 was adapted to the present situation as follows:

$$\frac{I_{Pd3d_{5/2}}}{I_{Al2p}} = \frac{\sigma_{Pd3d_{5/2}} N_{Pd} T_{Pd3d_{5/2}} \lambda_{Pd3d_{5/2}/Pd}}{\sigma_{Al2p} N_{Al} T_{Al2p} \lambda_{Al2p/Al_2O_3}} \cdot \frac{1 - exp(-\frac{d_{Pd}}{\lambda_{Pd3d_{5/2}/Pd}})}{exp(-\frac{d_{Pd}}{\lambda_{Al2p/Pd}})} \qquad (4.5)$$

The attenuation lengths $\lambda_{Al2p/Pd}$ and $\lambda_{Pd3d_{5/2}/Pd}$ come from [125] and are equal to 1.85 and 1.30 nm respectively. We have seen in the previous sections that the evaporation rate could be determined accurately with the quartz microbalance. The first five experimentally measured intensity ratios corresponding to a Palladium thickness of 0.1 nm (<0.4 ML)
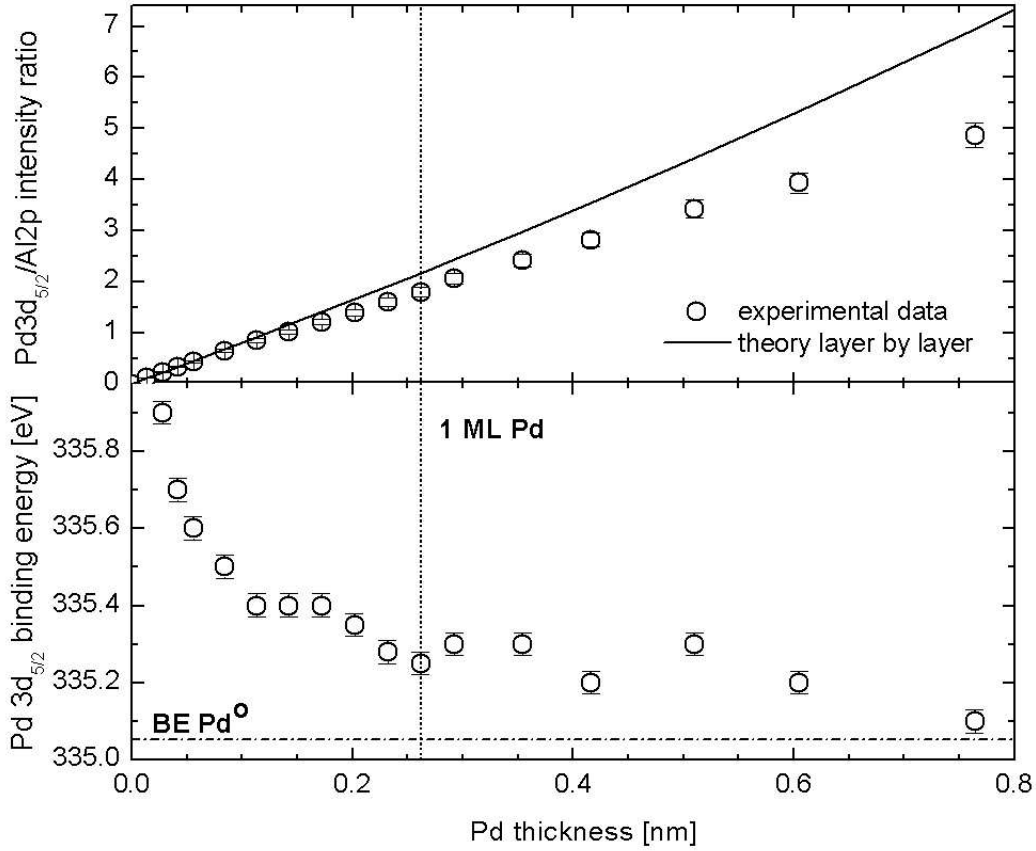
Figure 4.14: Upper panel: Evolution of the ratio of the XPS intensities of the $Pd3p_{5/2}$ signal over the Al2p signal. The dots correspond to experimental measurements and the solid line to the theoretical ratio assuming a layer by layer growth mode. Bottom panel: evolution of the binding energy corresponding to the $Pd3p_{5/2}$ signal with the thickness of palladium deposited on the $\gamma - Al_2O_3/Si$ substrate. Palladium was deposited at 473 K.

have been fitted with equation 4.6 in order to determine the overall value of the constant parameters.

$$\frac{I_{Pd3d_{5/2}}}{I_{Al2p}} = \frac{\sigma_{Pd3d_{5/2}} N_{Pd} T_{Pd3d_{5/2}}}{\sigma_{Al2p} N_{Al} T_{Al2p} \lambda_{Al2p/Al_2O_3}} \cdot d_{Pd} \qquad (4.6)$$

The curve of the theoretical intensity ratio corresponding to a Frank-van der Merwe growth mode was, as previously, calculated by replacing the parameters of equation 4.5 corresponding to the slope of equation 4.6 with the value obtained through the fitting procedure

mentioned previously. This curve is shown together with the experimental measurements in figure 4.14. The negative deviation of the experimental data from the theoretical line at about 0.1 nm ($\simeq$0.4 ML) can be interpreted by the formation of Palladium clusters for the same reasons as presented in section 4.3.2.3. The same deviation has been observed previously [132] at a coverage of 0.5 ML which is in very good agreement with the present findings. These observations correspond to a Stranski-Krastanov growth mode.

On the lower graph of figure 4.14, the BE of Palladium is decreasing from 335.9 eV to 335.1 which corresponds to the BE of bulk palladium [110]. The BE of 335.9 eV at the beginning of the deposition is close to the BE of PdO of 336 eV. This is in agreement with the statement of Bogicevic et al., who suggest, based on DFT calculations, that an oxide-metal bond is ionic at low coverage, regardless of the metal adsorbates considered [133]. The shift of 0.8 eV between low coverage and bulk palladium is close to the value of 1 eV found by Legare et al [134] and 0.9 eV by Bastl et al. [135]. Both authors emphasize that the exact mechanism of the BE shift is still debated in the literature. It is noteworthy that the BE decrease is not monotonous in figure 4.14 but presents some oscillations starting at a palladium thickness of 0.1 nm. Similar observations have been reported in the literature concerning the FWHM of XPS signals [136]. In our case, the thickness of 0.1 nm corresponds also to the beginning of the deviation of experimental data from the theoretical line shown in the upper graph of figure 4.14. It is therefore likely that the BE oscillations observed in graph 4.14 reflect some surface reconstruction. It could for instance be imagined that strains in the palladium film become more and more important with the increasing layer thickness. At a certain critical coverage, the strains may become sufficiently important to allow the system to overcome the activation barrier for a self reconstruction.

4.4   Conclusion

In a first step, the structure, morphology and chemical composition of $\gamma - Al_2O_3/Si$ substrates was investigated by the combined application of XPS, AES, SE and AFM. The cleaning procedure of these substrates included an initial flash of the sample followed by consecutive cycles of sputtering and annealing in oxygen. AES appeared to be more sensi-

tive to surface carbon contamination than XPS. After two cleaning cycles, the surface was considered as free of any external contamination. This corresponds to a carbon concentration below 5% with AES and 0.5 with XPS. Auger measurements indicated an almost perfect surface stoichiometry while XPS data suggested a slight excess of oxygen. This can be explained by the presence of -OH groups on the surface as already reported in the literature.

The images of the $\gamma - Al_2O_3/Si$ substrates obtained by AFM did not allow to distinguish any structure on the surface, indicating therefore a very smooth morphology. SE suggested in a first step, an aluminum oxide thickness of 14.1 nm instead of the expected 10 nm. It was shown later by the depth profile of a catalyst that the SE value probably included the Al_2O_3 layer but also an additional layer of SiO_2 with a few nm thickness at the interface between Si and Al_2O_3. It is well known that silicon oxide and aluminum oxide cannot be distinguished by SE due to the similar optical properties.

SE confirmed the nickel and palladium evaporation rates determined by the QCM with a remarkable accuracy. The growth mechanism of nickel and palladium over γ-Al_2O_3 has been investigated by a combination of XPS and AFM analysis. At room temperature, no clusters could be observed by AFM and based on literature data, the evaporation rate was lowered and the surface temperature of the substrate increased. This should in principle enhance the mobility of the metal atoms in order to accelerate the formation of clusters reported in the literature to be thermodynamically favored compared to a flat layer. The optimal conditions for the preparation of our catalysts were found to correspond to substrate temperatures of 623 K and 473 K combined with evaporation rates of 0.5 and 0.8 Å/min for nickel and palladium respectively. The size of the palladium and nickel aggregates could be tuned by varying the amount of evaporated metal. However, an increase of particle size was accompanied with an increase of the size distribution and resulted therefore in a bad homogeneity of the surface. It was finally shown, based on XPS experiments, that within our experimental conditions, the deposition of both metals follows a Stranski-Krastanov growth mode. The formation of clusters was found to start already around 0.5 average ML for both nickel and palladium.

Based on the present results, it is possible to prepare Ni/Pd model catalysts with a well-defined composition and surface morphology which is essential for the further experiments.

Chapter 5

UHV xenon excimer lamp construction and characterization

5.1 Introduction

In the past decades, the use of UV-VUV radiations with an energy in the range of 5 to 15 eV has found numerous industrial applications. The expression *Vacuum Ultra Violet* derives from the fact that air strongly absorbs radiation below 190 nm with the consequence that these wavelengths can only be used under vacuum or non-absorbing gases like argon or nitrogen. UV/VUV sources have become essential technologies for a variety of photoinduced processes in fields such as chemistry, electronics, food/water treatment [137] as well as medical therapies [138]. Concrete examples of applications are photoinduced thin films deposition [78][139][140][141][142], curing of polymer (glues, inks...) [143], large scale surface cleaning, ozone production, copy machines, micro-structuring of polymers [144][145], skin disorders treatment, water disinfection and plasma display panels. The reason why UV and VUV photons are so interesting is the fact that they are able to split most chemical bonds (figure 5.1).

 For the industrial applications listed above, high intensity sources of UV/VUV photons are desirable. In addition, the UV spectrum of these sources has to match the process of interest. Until recently, mercury based lamps were the main commercially available system which was applied at an industrial scale. Medium and high pressure mercury lamps have
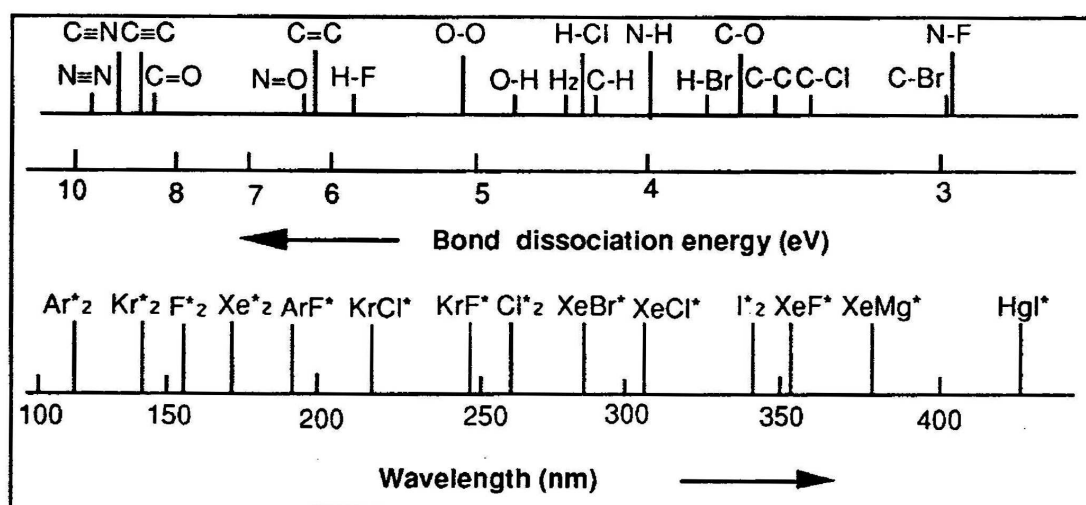
Figure 5.1: Selection of wavelength available from excimer sources compared with some common chemical bonds [146].

been the workhorses in most applications. However, these lamps are characterized by a very broad emission spectrum ranging from 200 nm to the infrared They emit therefore, beside the wavelengths of interest, other unwanted radiation. More selective UV sources were restricted to low pressure mercury/rare gas mixtures with a main line at 254 nm and a less intense line around 185 nm. Other sources like low pressure rare gas (argon 107 nm, krypton 124 nm, xenon 147 nm) or deuterium lamps (122 nm) are in principle available but suffer from a low photon flux and are consequently not suited for industrial applications [147]. Since most materials absorb radiation below 250 nm, there was a strong demand for intense, high efficient, selective and low cost UV/VUV sources.

An interesting approach to satisfy this demand was the application of rare gas excited dimer (excimer) radiative decomposition to produce energetic photons. These excimers can be generated from pure rare gas or rare gas/halide (excited complex) mixtures and various excitation sources can be applied, as for instance synchrotron radiation [148], γ-rays [149], X-rays [150], microwave discharges [151][152], high energy electron beams [153], α-particles [154][155] or protons [156]. For evident reasons, all these techniques are however not really suited for industrial applications and widespread utilization. A much more convenient system for the generation of excimers is the so called **dielectric barrier discharge (DBD)**.

A typical DBD configuration consists in a planar arrangement of two electrodes with at least one dielectric layer located between the electrodes (fig. 5.2). The first investigations
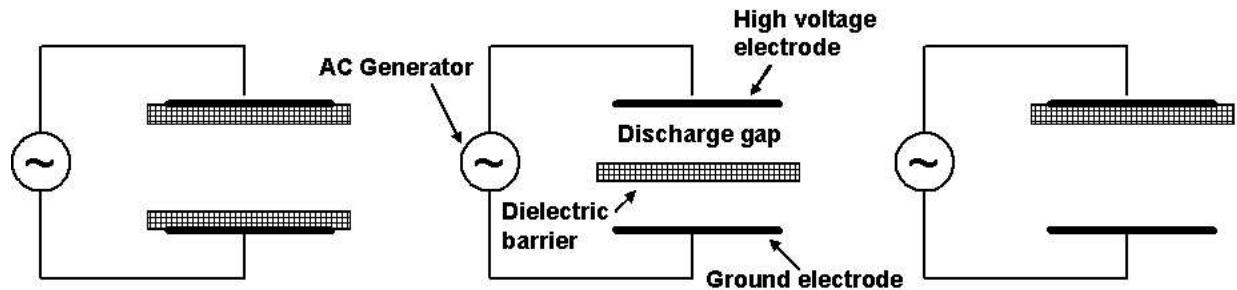
Figure 5.2: Basic dielectric-barrier discharge configuration.

about DBD were reported by Ernst Werner von Siemens in 1857 [157] who studied the production of ozone. Oxygen or air was exposed to a DBD in the gap between two concentric glass tubes by an alternating electric field. The most innovative feature of this system was that the electrodes were located outside of the glass tubes and therefore not in direct contact with the reactant gas and microdischarges. DBD was originally called *silent discharge* by Andrews and Taig three years after Siemens' publication [158]. At the

Figure 5.3: Ozone generators for the treatment of water [159].

beginning of the last century, large scale ozone generators for the treatment of water were produced in Europe [160] and Tanaka published the first experiments involving dielectric barrier discharges for the generation of VUV excimer radiations [161]. His research was focused on the generation of small light sources for spectroscopic applications. Later, at the end of the eighties Kogelschatz and Eliasson [162] brought a decisive contribution to the development of DBD lamps and initiated the large scale and widespread application of UV/VUV excimer sources in industry. The most striking example of the commercial success of DBD lamps is probably their utilization in plasma display panels (PDP). The visible light is produced through irradiation of some phosphor layers irradiated with small DBD cells filled with a mixture of xenon and neon or helium. From roughly 300'000 units produced worldwide in 2001 [163] this number increased dramatically to exceed 1 million units in the month of August 2007 and 1.53 million in November of the same year. A total of 12.2 million PDPs have finally been produced in 2007 and the market is expected to exceed US$10 billion revenue in 2008 [164].

When a high alternating voltage (2-10 kV/100-500 kHz) is applied to the electrodes of a DBD lamp filled with a few hundred mbar of a suitable gas mixture, breakdowns are initiated in many different filaments at a frequency equal to two times the driving frequency. At each discharge, a flow of electrons travels from one side of the dielectric in the direction of the positive electrode. As charge accumulates at the "end" of the filament, the voltage drop across the filament decreases dramatically which results in the extinction of the discharge. The charge which accumulates on the surface of the dielectric is then neutralized during the next half wave by electrons flowing the "opposite way". The low mobility of the electrons on the surface of the dielectric is not only responsible for the rapid extinction of the filaments but also for the limited area around them where the voltage drop occurs, allowing the formation of parallel filaments in the proximity of "previous" ones. This explains why the whole surface of the dielectric becomes covered with close and equally spaced filaments when the lamp is in operation. These filaments are typically characterized by a diameter of about 0.1 mm, an electric field strength of 0.1 to 100 kV/cm and electron densities which can reach values as high as 10^{14} to 10^{15} cm^{-3} [138] corresponding to currents in the range of 100 to 1000 A/cm^2.

When a breakdown is initiated in the discharge gap, the gas becomes immediately conduc-

tive as a result of the formation of ions and electrons. The electrons formed during the ionization process are immediately strongly accelerated under the influence of the electric field up to kinetic energies in the range of 1-10 eV [162]. They experience then collisions with the gas atoms contained in the lamp resulting in the formation of various excited and/or ionized species. These species undergo then non radiative relaxation and recombination between each other following some intersections of their potential energy curves going sequentially from the upper excited state to the lower one. The final transition from the lower excited state to the ground state is radiative and the origin of the resulting UV/VUV emission. A simplified description of the pumping mechanism involved for the case of xenon is shown in figure 5.4. At low pressure, the emission of xenon atoms is
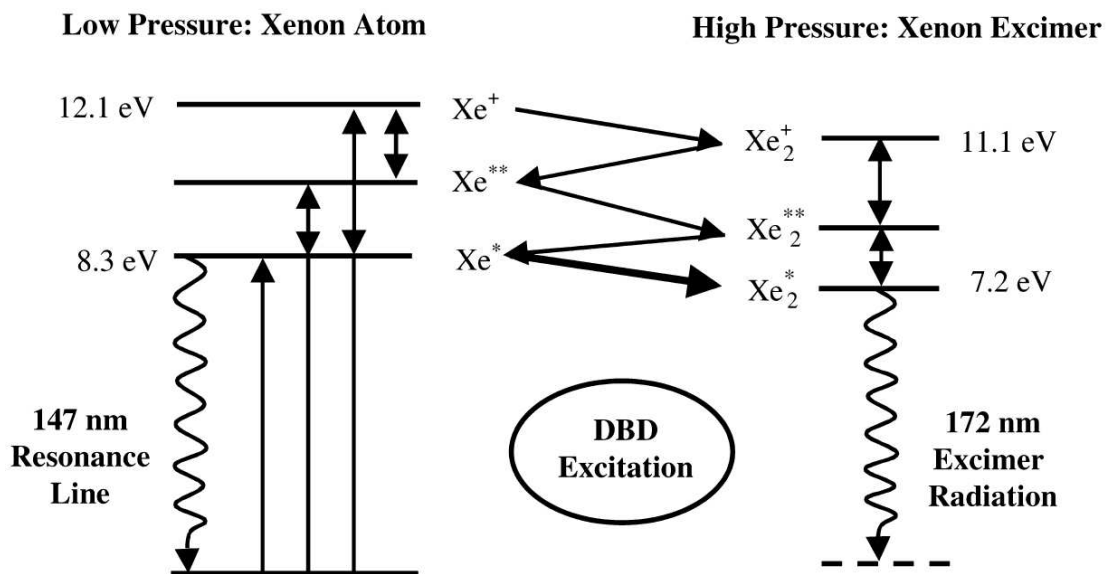
Figure 5.4: Simplified pumping scheme for xenon [159].

predominant while the formation of excimers is favored at pressures above 50-100 mbar. A simplified scheme describing the mechanism of UV/VUV emission at high pressure is given below [165]:

1) Excitation of rare gas (Rg) atoms by electron impact:

$$e^- + Rg \rightarrow Rg^* + e^-$$ (5.1)

2) Excimer formation by three body collision:

$$Rg^* + Rg + Rg \rightarrow Rg_2^* + Rg \tag{5.2}$$

3) The formed excited molecule is highly unstable and dissociates after typically few nanoseconds into two atoms in the ground state with the emission of a photon:

$$Rg_2^* \rightarrow 2Rg + h\nu \tag{5.3}$$

A potential energy diagram of this process is shown in figure 5.5. It is noteworthy that the
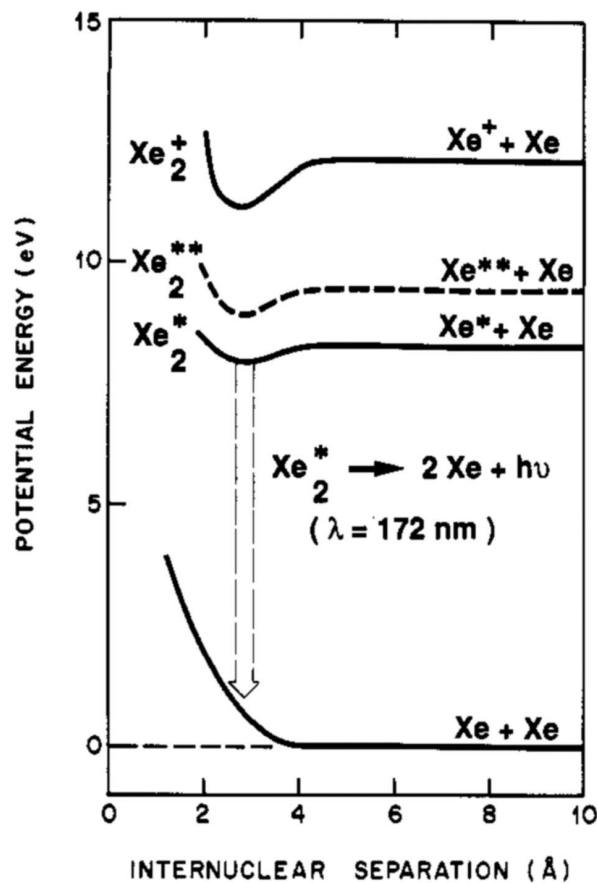
Figure 5.5: Simplified potential energy diagram of molecular xenon [147].

excimer molecules do not possess any stable ground state and this property is the origin of a key feature of excimer lamps, namely the absence of self-absorption. No reabsorption

can occur, as excimers only exist as excited species for an extremely short moment. The gas inside of the lamp is therefore perfectly transparent to the radiation generated. This partly explains the high UV intensity and efficiency of these UV/VUV sources. In theory, some excimer lamps can reach 50-80% efficiency under special discharge conditions [166][167]. Practical efficiencies up to 60% have been reported [138]. Another very important characteristic of excimer lamps is connected with the DBD configuration itself. The role of the dielectric barrier is to distribute the microdischarges evenly over the entire electrode area and to limit the amount of charge which can flow in a single discharge as described above. The gas discharges are therefore very quickly terminated, after few tens of nanoseconds, preventing them to degenerate into a thermal arc. The self extinguishing property of this type of discharge allows the use of high pressure without causing any sputtering of the dielectric. In addition, as the dielectric material separates the discharge gases and the electrodes, it prevents any electrode corrosion and gas contamination build up as it is the case in conventional UV/VUV sources. This feature results in an extended lifetime of lamps based on the DBD technology. Up to 10'000 hours have been reported depending on the lamp design and operating conditions [138]. Also noteworthy is the fact that DBD excimer lamps can be built with a variety of different geometries, the most common one consisting of two concentric quartz tubes with an annular gap of about 1 mm in between. A planar configuration is also relatively common but more exotic shapes could be imagined to suit the process of interest. Figure 5.6 shows three standard geometries for excimer lamps. Finally, other advantages excimer lamps provide compared to mercury
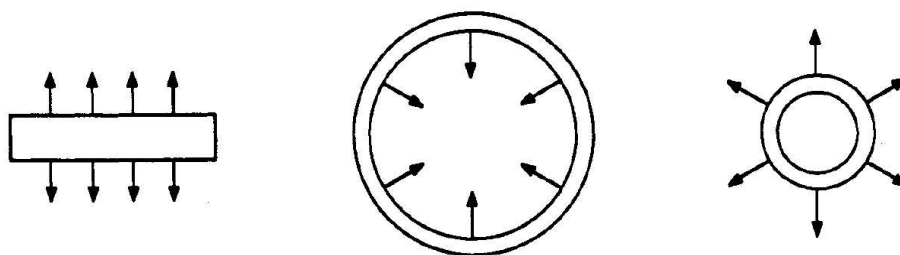
Figure 5.6: Schematic diagram of different geometrical silent-discharge configurations [147].

lamps are the ecological aspect as no elementary mercury is needed, the fact that most of the radiations are concentrated in a narrow emission peak and that no warm up time

is required to reach full radiant power. This point is especially interesting in the case of printing machines where the UV source used for curing printing ink can be switched off during successive jobs resulting in a substantial energy economy. Due to their low cost, simplicity and reliability, DBD excimer lamps have definite advantages compared to mercury lamps or lasers when certain industrial applications are envisaged.

Today, DBD based UV sources can be built for a variety of wavelengths ranging from 126 nm to 354 nm (figure 5.1). The major hindrance for lamps producing photons with wave-

Table 5.1: Excimer complexes and corresponding peak wavelength [168].

Excimer	Wavelength [nm]	UV range
Ar_2^*	126	
Kr_2^*	146	
F_2^*	158	
$ArBr^*$	165	
Xe_2^*	172	VUV
$ArCl^*$	175	
KrI^*	190	
ArF^*	193	
$KrBr^*$	207	
$KrCl^*$	222	
KrF^*	249	UVC
XeI^*	253	
Cl_2^*	259	
$XeBr^*$	283	
Br_2^*	289	UVB
$XeCl^*$	308	
I_2^*	342	UVA
XeF^*	354	

length shorter than 160 nm is the window materials which should of course be transparent to the photons produced. 160 nm corresponds to the cut-off wavelength of high purity quartz. More energetic photons require the use of MgF_2, CaF_2 or LiF, which present serious drawbacks like low transmission, hygroscopicity, and limited lifetime due the formation of color centers. These materials are in addition less convenient to handle and difficult to shape into the desired lamp geometry compared to quartz. For some applications, an interesting way to circumvent the problems connected to the window material is to use a particular configuration called "windowless excimer VUV source with parallel cylindrical electrodes" [169] shown in figure 5.7. With this arrangement, the substrates
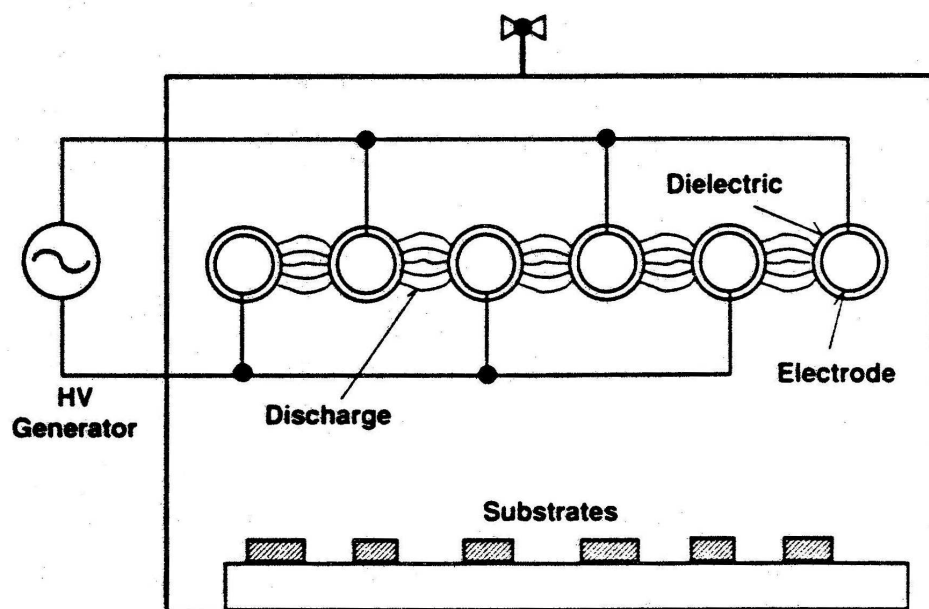
Figure 5.7: Windowless excimer VUV source with parallel cylindrical electrodes [169].

can be directly exposed to the VUV excimer radiation, hence suppressing the need of a transparent dielectric and allowing the application of very low wavelengths.

In the frame of this work, a xenon lamp emitting at 172 nm (fig. 5.8) was chosen for the study of the photoassisted activation of methane. Methane does not absorb significantly above 140 nm and its C-H bonds have only an absorbance maximum at 125 nm. A direct activation in the gas phase which is not desirable will therefore not take place.
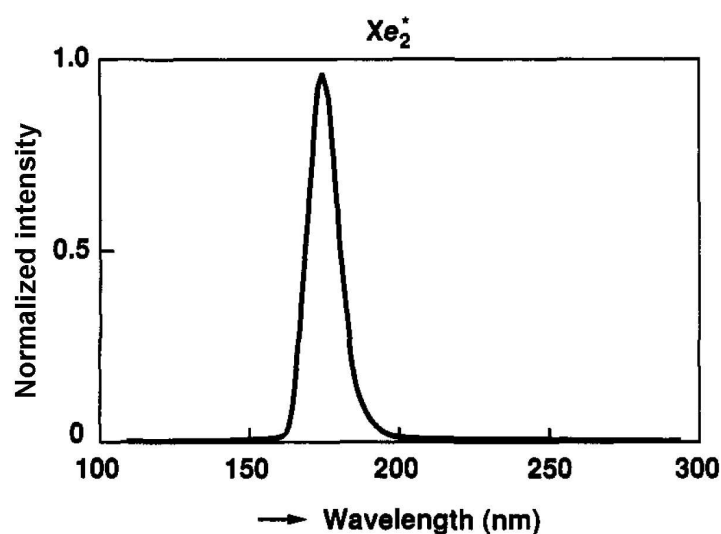
Figure 5.8: Emission spectrum of a xenon excimer lamp.

This however does not exclude an assisted activation following a mechanism different than the direct activation by a combination of a catalyst and photon effect. Among excimer lamps, the xenon lamp is especially interesting because it has the highest efficiency and represents an excellent "energy/ease of construction" ratio because no exotic materials are needed as dielectric. High purity quartz which is relatively easy to handle was used in the present work. In spite of the fact that some UV sources are available commercially, none of those can be fitted into the UHV chamber used for our research. A unique system had therefore to be developed in order to fit the stringent requirements imposed by the use of high voltage and the need of an efficient cooling in the extremely limited space like a UHV chamber.

5.2 Experimental

5.2.1 Lamp envelope

The lamp had to be installed in a DN63CF (ID 66 mm) port of the preparation chamber with the lamp tube perpendicular to the axis of the port. Taking into account the need of a support including water cooling and shielding to protect the chamber from the radiation,

the total length of the lamp tube was chosen to be 40 mm to leave some space for the other required parts. The quartz tube used for the lamp envelope have an inner diameter of 12 and 18 mm and an outer diameter of 14 and 20 mm respectively. The wall thickness is therefore 1 mm and the discharge gap has a width of 2 mm. A sketch of the lamp is shown in figure 5.9. The small tube (8 mm ID 10 mm OD) connected to the side of the envelope
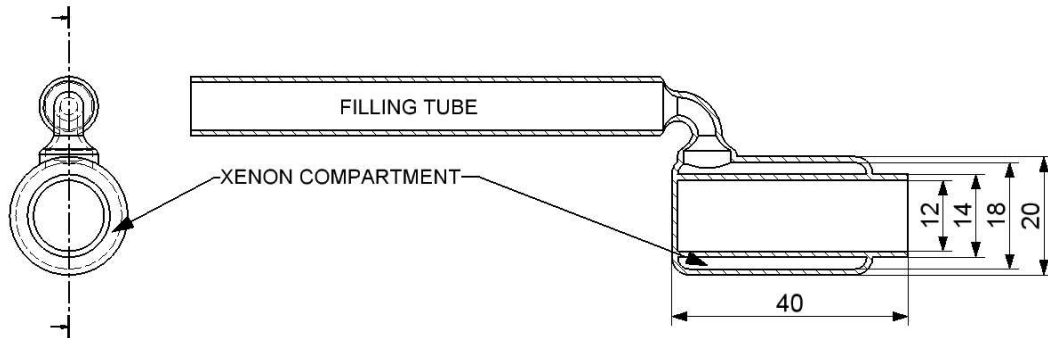
Figure 5.9: Excimer lamp envelope geometry as used in the experiments.

is used for cleaning purposes and to attach the lamp to a filling station where it will be evacuated, filled with xenon, and finally sealed. The material used for this lamp is a high purity synthetic fused silica manufactured by flame hydrolysis of $SiCl_4$. This special quartz known as "SUPRASIL[R]" combines excellent physical properties with outstanding optical characteristics in the deep UV wavelength range. As it can be seen in figure 5.10, the transmission is still higher than 90% at 172 nm for a wall thickness of 1 mm. In addition, this materials provides an excellent resistance to damage by VUV radiation, which is not the case for standard quartz quality. This special property is partly due to the high OH content of this quartz which is typically around 250 to 1000 ppm. OH groups lower the viscosity of SiO_2 and probably reduce the number of strained bonds in the network which are known to have a negative effect on the radiation resistance [170].

5.2.2 Excimer lamp cleaning and filling

As mentioned above, the gas compartment must be thoroughly cleaned before being filled with xenon 5.0. It is first rinsed with a 1:1 mixture of concentrated HF (20%) and concentrated HNO_3 (65%). The purpose of this operation is to remove impurities but also to
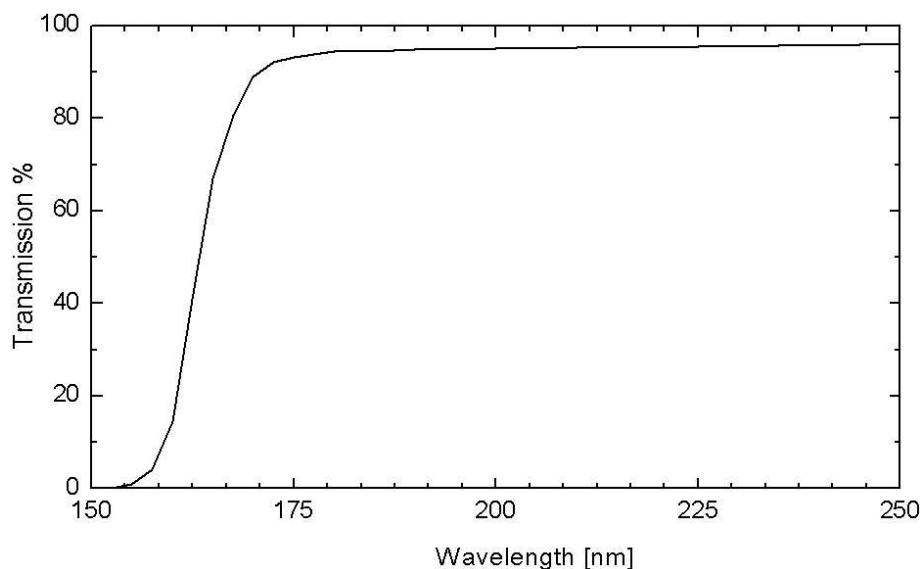
Figure 5.10: Transmission of a 1 mm thick suprasil®sample.

etch slightly the quartz walls which may take a milky tint due to SiO_2 reduction during the manufacturing process. The lamp is then rinsed three times with high purity water and mounted on a dedicated "filling station". The filling station is a small UHV chamber including a home made quartz-metal connection, an argon and xenon inlet as well as two pressure gauges, a UHV and a mechanical one. The mechanical gauge has a working range going up to 1 bar absolute and was used for the determination of the xenon filling pressure. The pumping system includes a Pfeiffer 50 l/s turbo drag pump backed by an Alcatel 15 m^3/h rotary vane pump. This filling station can be seen in figure 5.11. The lamp was first evacuated and water adsorbed on the inner walls was removed by filling the lamp with argon and running discharges for 1 minute. This procedure was repeated three times. Then, a tubular oven fixed on a rail was placed around the lamp, which was annealed for 12 hours at 850 ^{o}C. The filling step took place only when the pressure in the filling station reached 10^{-8} mbar after cooling down and was immediately followed by the sealing of the lamp envelope by an experienced glass blower. The optimal filling pressure was determined by measuring the lamp intensity at various pressures with a XUV-detector from the company Gigahertz-Optik. This detector includes a 1 cm^2 VUV-photodiode and was operated together with a 172 nm standard bandpass filter (FWHM 20 $\pm$7.5 nm) in

(a)   (b)
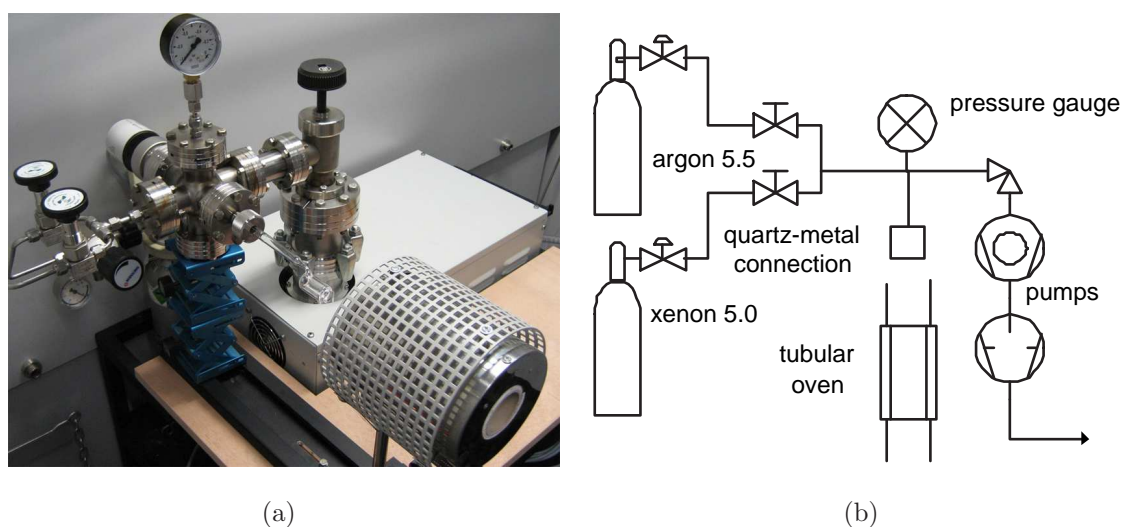
Figure 5.11: (a) Filling station with a lamp attached (b) Sketch of the filling station.

order to remove all wavelengths other than 172 nm, especially IR radiation. The lamp was powered by an ENI plasma generator, model HPG-2, 0-10 kV, 125-375 kHz. The emitted intensity of the excimer lamp cannot be measured in air as oxygen absorbs VUV at 172 nm. A small chamber made of polycarbonate was built for this purpose. This chamber, shown in figure 5.12, can be flushed with a non absorbing gas, nitrogen in our case, and comprises an aperture where the VUV detector can be installed as well as a high voltage feedthrough.
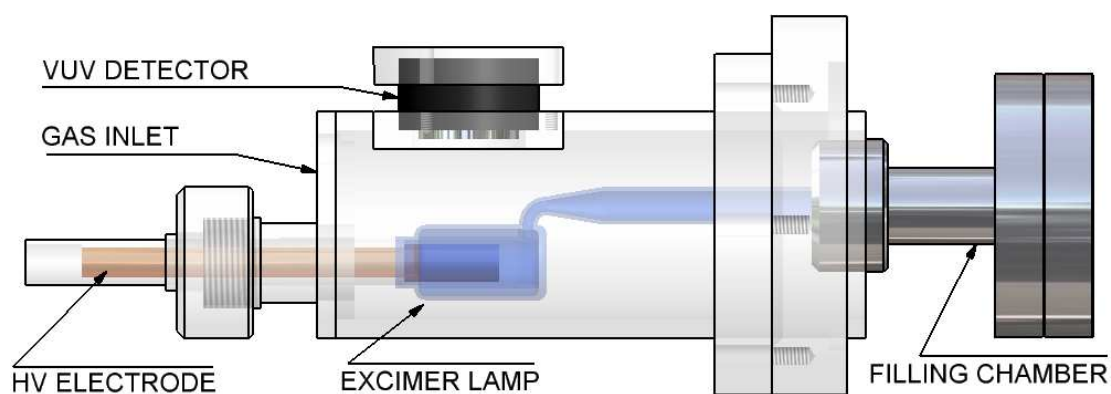
Figure 5.12: Drawing of the device used for evaluation of the xenon pressure.

5.2.3   Excimer lamp calibration

After being filled with xenon and sealed, the lamp was finally calibrated "in situ" in a small UHV chamber (figure 5.13) at a base pressure of 10^{-8} mbar. This chamber contained a UV grade sapphire window (Caburn) in front of the lamp tube through which the VUV emission could be measured with a photodiode located outside of the UHV chamber. A fitting including a gas inlet and outlet was built and install between the photodiode and the sapphire window. This fitting can be flushed with nitrogen in order to avoid absorption of the VUV photons by oxygen in air. The present setup allowed us to test the lamp in UHV, that is in the same experimental conditions as in the preparation chamber where the lamp will eventually be applied.
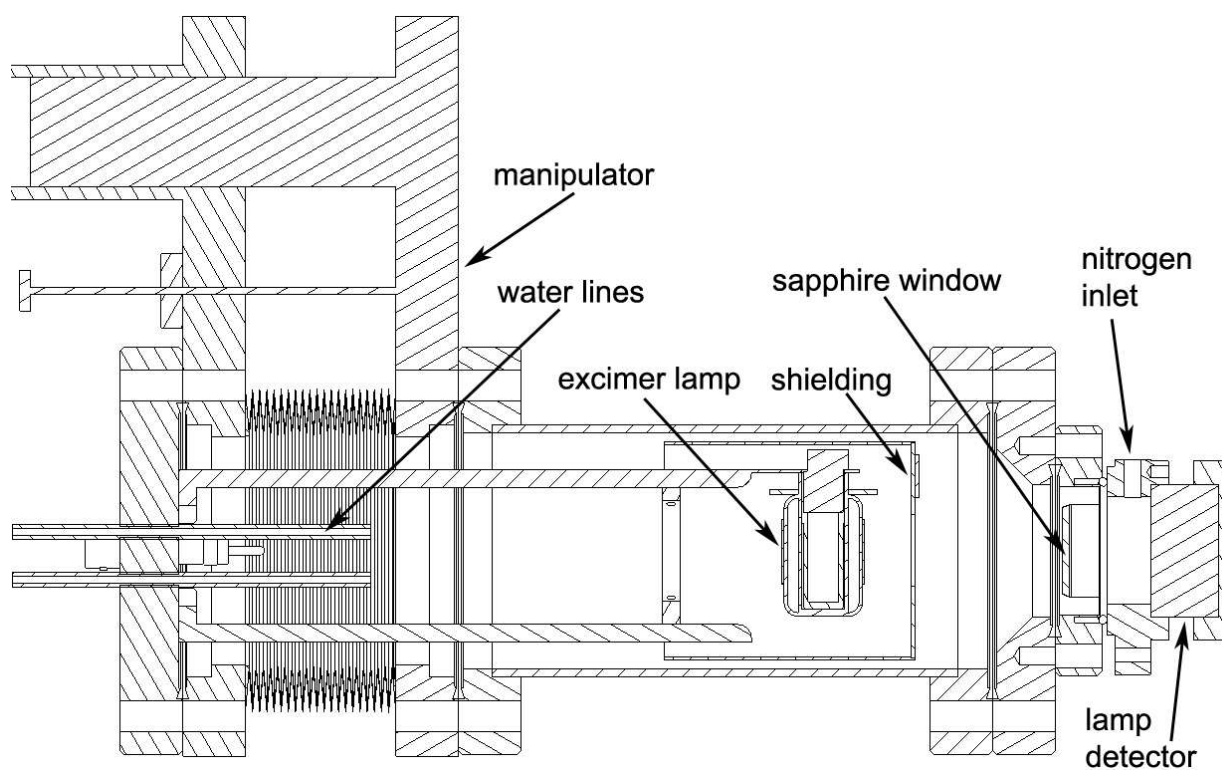
Figure 5.13: Side cut of the calibration chamber.

5.2.4   Lamp cooling

5.2.4.1   Indirect cooling configuration

In the initial design of the excimer lamp, the inner electrode contained a small channel in which water was circulated. Because of that, we placed the high voltage electrode on the external quartz tube of the lamp and we used the inner cooled electrode for the ground. This avoids the use of HV breaks along the cooling lines which would have been complicated to incorporate in the already very compact design. This electrodes configuration is the opposite of the "usual" one where the high voltage electrode is located "inside", a design which is probably used for safety reasons.

A particularly crippling drawback of this cooling design resides in the heat transfer between the lamp envelope and the inner electrode which appeared to be very low. After few minutes of operation the lamp was starting to glow red indicating a temperature of several hundred degrees. As it can be seen in figure 5.14 the heat produced has to "flow" from the quartz to the electrode which is actually very efficiently cooled. The problem originates from the
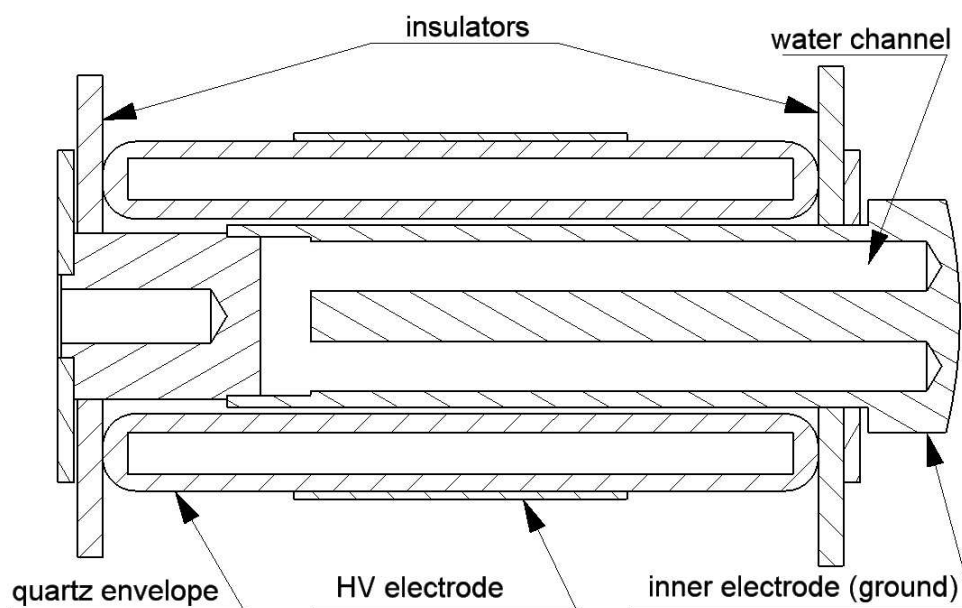
Figure 5.14: First configuration of the excimer lamp based on an indirect cooling.

fact that the contact between the inner quartz tube and the electrode is very poor. This is a consequence of the lamp manufacturing process which results in non perfectly regular walls. A small gap exists therefore between these two parts hindering the heat transfer. This problem is especially serious as the lamp is operated in vacuum.

5.2.4.2 Direct cooling configuration

In order to improve the cooling of the lamp, a different configuration which makes use of a direct cooling was tested. In this design, which is illustrated in figure 5.15, one side of the inner lamp tube was sealed compared to the configuration of figure 5.14. The lamp was then glued with a special UHV sealant (Epotek H27D) on the inner electrode which was cut beforehand to let water flow directly inside of the inner quartz tube hence providing a very efficient cooling. This design was working well from the point of view of the heat removal.
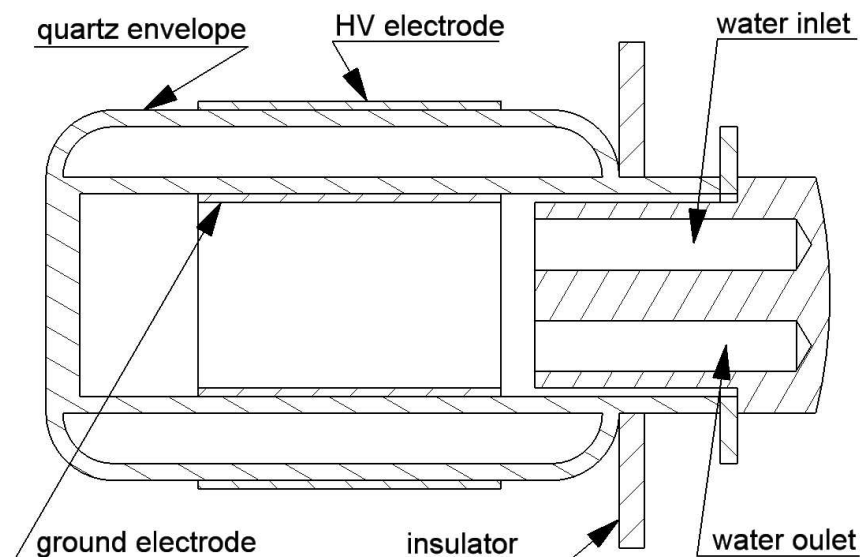
Figure 5.15: Direct cooling of configuration of the excimer lamp.

Unfortunately a crack appeared in the quartz at the connection between the lamp tube and the inner electrode. This breakage was probably a consequence of the big discrepancy between the thermal expansion coefficients of copper and quartz being $17 \cdot 10^{-6}$ K^{-1} and $0.5 \cdot 10^{-6}$ K^{-1} respectively. The consequence is the formation of strains with temperature changes and maybe glue curing. This design was finally abandoned because of its fragility.

5.2.4.3   Improved indirect cooling configuration

The final configuration adopted makes use of an indirect cooling similar to the one presented in section 5.2.4.1, but modified for more robustness. This is essential as a breakage of a directly cooled lamp would result in the release of water into the UHV chamber resulting in potentially serious damages. In order to avoid the cooling problems encountered previously, the gap between the inner electrode and the quartz envelope was filled with an alloy of 97% indium and 3% silver (Ostalloy 296, Arconium). This alloy is very soft and has a melting temperature of 146 ^{o}C. A small amount of it was deposited in the inner cavity of the lamp tube and placed in an oven at 160 ^{o}C. The copper inner electrode was also heated at about 160 ^{o}C and then inserted in the lamp envelope so that the liquid indium/silver alloy filled the gap between lamp and electrode. As indium is sticking very strongly to quartz, the inner wall of the lamp envelope was treated beforehand with formic acid vapors in order to form a very thin layer of indium-formate at the quartz/indium interface. As indium formate does not adhere to quartz, this technique is meant to decouple the thermal expansion and contraction of the electrode and the lamp and therefore avoid the formation of strain due to temperature changes. A drawing of the resulting configuration is shown in figure 5.16.

5.3   Results and discussion

5.3.1   Lamp emission

As shown in figure 5.17 some in-house built lamps exhibited, beside the VUV photons, a characteristic green glow (figure 5.17(a)). A green emission is known to be typical of an oxygen contamination of the discharge gap. The typical blue fluorescence of excimer lamps can be seen in figure 5.17(b). A leak test on the filling station as well as an analysis of the xenon bottle composition excluded the possibility of an oxygen contamination. The green light observed was then characterized by emission spectroscopy. The resulting spectrum can be seen in figure 5.18 and does not correspond to the typical emission of XeO which is formed in the case of an oxygen contamination (figure 5.19).   Furthermore, it was observed that some experimental factors had an influence on the intensity of the emitted
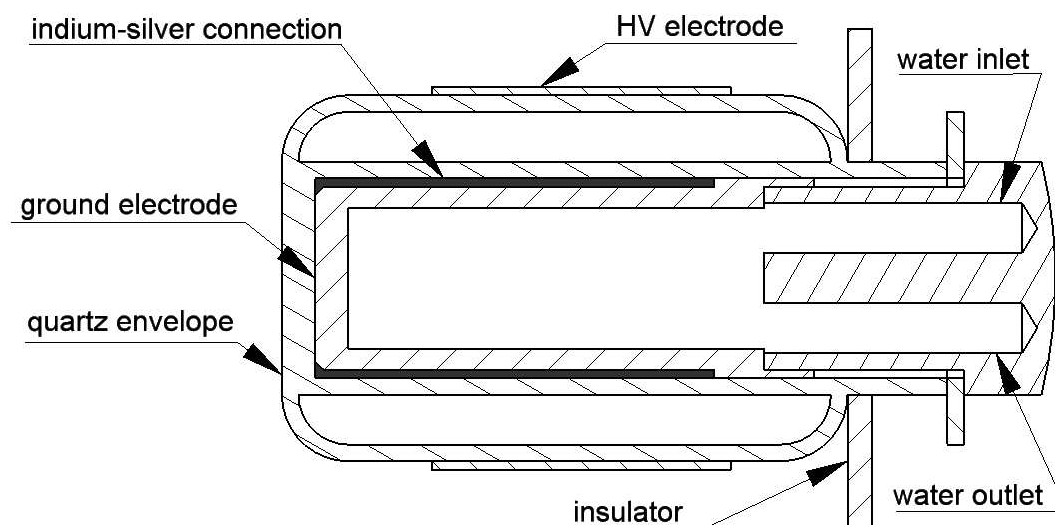
Figure 5.16: Final configuration of the excimer lamp making use of an indium connection between the lamp envelope and the inner ground electrode.

green light, in spite of the fact that the same quartz quality was used for the construction of our lamps. The factors found to have the greatest influence were the "manufacturing process" and the annealing time and temperature of the lamps before filling. It was observed that long annealing time and/or high temperature result in a more intense green emission and simultaneously in a weaker blue color. The lamp shown in figure 5.17(b) has not been annealed while the one of figure 5.17(a) was heated in air during 24 hours at 850 ^{o}C. This phenomenon had been reported elsewhere [170] but the source of the green light is still uncertain. It was however noticed that the quartz samples exhibiting such properties showed a superior VUV resistance.

Some common intrinsic defects present in fused silica are oxygen deficiency I (ODCI), corresponding to relaxed oxygen deficiency centers symbolized by $\equiv$Si-Si$\equiv$, oxygen deficiency II (ODCII), corresponding to unrelaxed oxygen deficiencies or $\equiv$Si$\cap$Si$\equiv$, Si-H and Si-OH groups, three fold coordinated silicon atoms (E') and non bridging oxygen holes ($\equiv$Si-O$\bullet$ or NBOH). Some of these defects are known to act as optical absorption centers in the UV/VUV range like for example Si-OH, ODCI and ODCII which absorb at 160, 163, and 215 nm respectively. The optical properties of quartz are strongly related to the concentra-

(a)   (b)
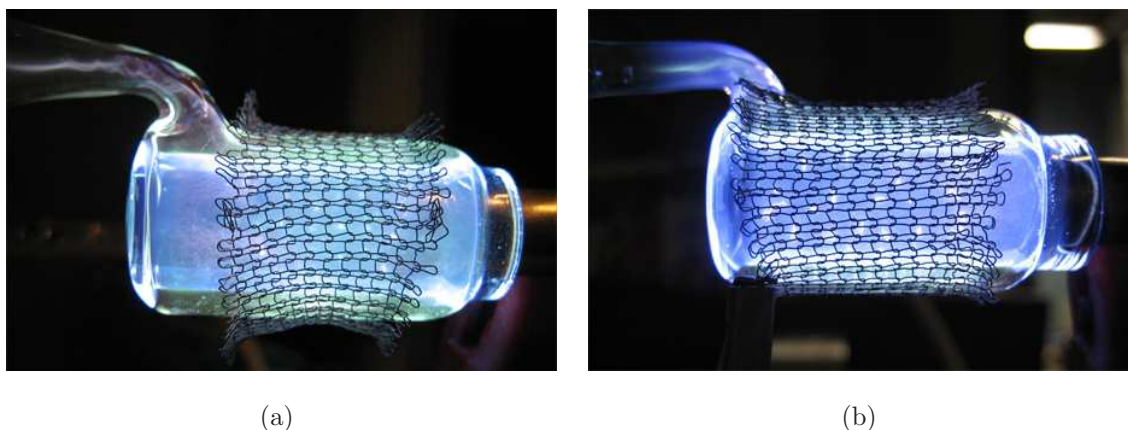
Figure 5.17: (a) Lamp emitting a greenish light (b) Typical xenon excimer lamp color.

tion of the different defects which act as precursors for the formation of color centers upon UV/VUV irradiation. ODCII is for instance responsible for a blue photoluminescence at 390 nm [172] and NBOH for a red one at 650 nm [173]. Possible reactions which can lead to a transmission decrease of the quartz envelope of excimer lamps are listed below [174]:

$$\text{Si-O-Si} \xrightarrow{h\nu} \text{NBOH} + \text{E'} \tag{5.4}$$

Reaction 5.4 is a photoinduced network breakage with the creation of a NBOH and E' absorption centers. It was indeed observed that after a few ten hours of operation our lamp became slightly reddish. This is typical of xenon lamps and can be attributed to the formation of NBOH.

SiH groups can be broken to form E' according to reaction 5.5. The E' can finally be converted to ODC as described in equation 5.6.

$$\text{Si-H} \xrightarrow{h\nu} \text{E'} + \frac{1}{2}\text{H}_2 \tag{5.5}$$

$$2\text{E'} \underset{}{\overset{h\nu}{\rightleftharpoons}} \text{ODC} \tag{5.6}$$

It is a well known that synthetic fused quartz silica containing high -OH concentrations exhibit an excellent radiation resistance, especially after thermal treatment. Reaction 5.7 has been proposed to explain this phenomenon.

$$\text{Si-OH} + \text{Si-H} \xrightarrow{\Delta} \text{H}_2 \uparrow + \text{Si-O-Si} \tag{5.7}$$
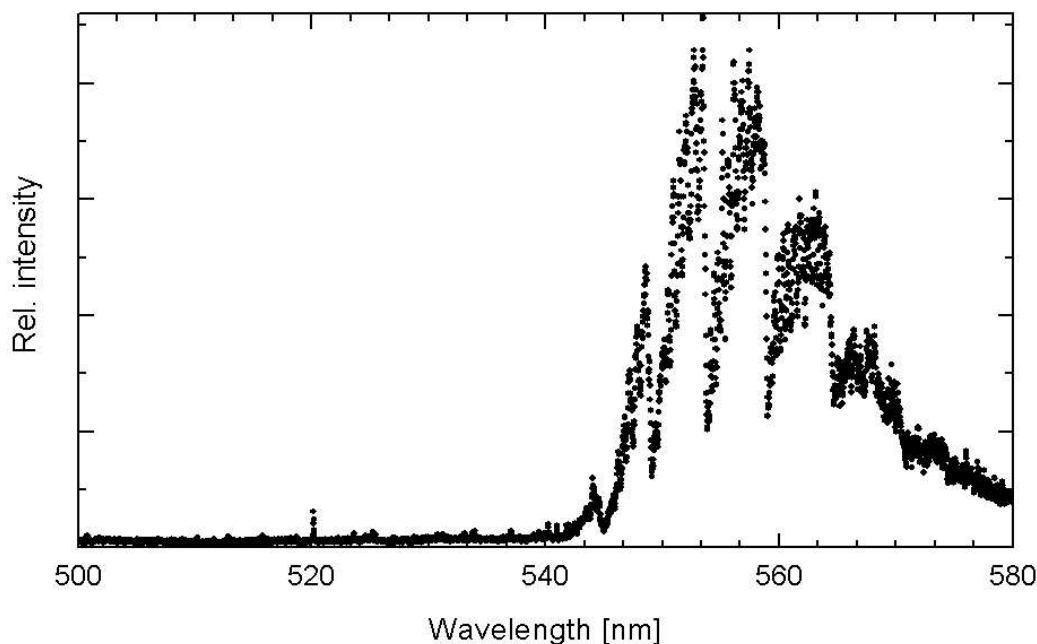
Figure 5.18: Emission spectrum in the visible range corresponding the green emission of the lamp [171].

Due to the large excess of Si-OH, most of the Si-H centers are bleached and the released hydrogen diffuses out of the material. After annealing, the formation of E' from Si-H (reaction 5.5) is no longer possible and the only source of new defect centers is given by equation 5.4. The decrease of the blue photoluminescence observed upon annealing seems to indicate a conversion of ODCII defects. As a matter of fact, ODCII are responsible for the blue photoluminescence of the lamp under irradiation. Imai et al. [175] have suggested that the ratio of ODCI to ODCII can be changed by thermal treatment. A relaxation of ODCII to ODCI during annealing according to reaction 5.8 would therefore explain the observed attenuation of the blue luminescence.

$$\equiv\text{Si}\cap\text{Si}\equiv \xrightarrow{\Delta} \equiv\text{Si-Si}\equiv \tag{5.8}$$

Apart from the annealing process, the manufacturing technique also has a clear influence on the quartz photoluminescence. The lamps built in the framework of this project have been made by three different glass blowers resulting in three different green photolumines-
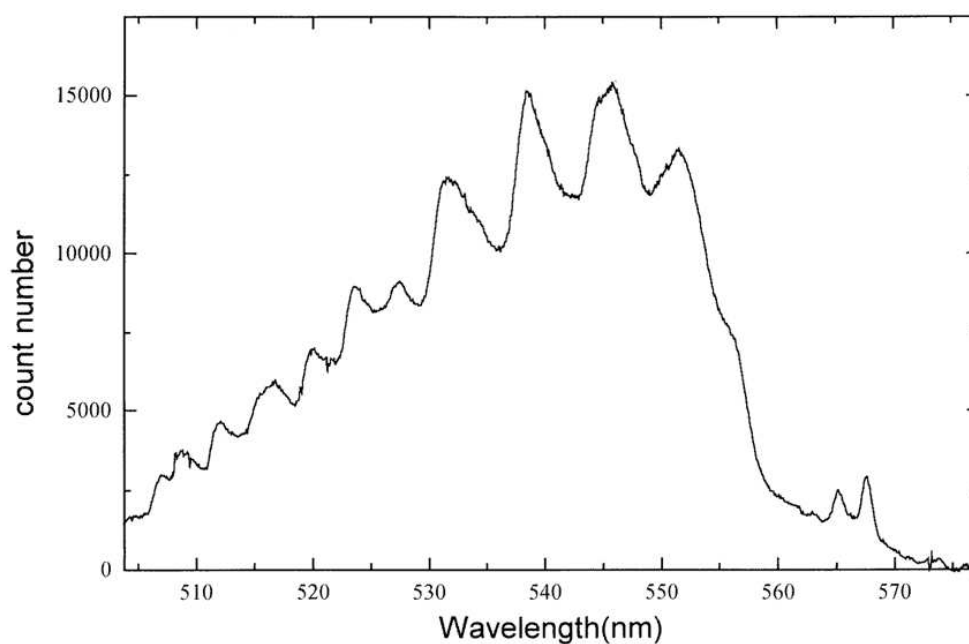
Figure 5.19: Emission spectrum of XeO formed in the case of an oxygen contamination of a xenon excimer lamp.

cence intensity. The exact origin of this green emission is still uncertain but can probably be explained by the "promotion" of particular defects or diffusion of impurities, which originate from the fabrication technique, in the envelope. Quartz impurities can for instance be created by the tools used in hot forming processes which are typically made of graphite, tungsten and molybdenum. These materials contain metal impurities which can diffuse into the quartz at high temperature. Such a contamination known as *extrinsic defects* is not likely in our case as no materials were in contact with the quartz during the annealing process which also resulted in an increase of the green photoluminescence intensity. Other network imperfections may originate from the "experimental" conditions applied during the lamp construction and are called *technology related defects*. The creation of such defects can be influenced by the heating temperature of the quartz or the overall fabrication duration. The use of different regions of the blowtorch flame, oxidizing or reducing, may also result in different imperfections in the final quartz network. This could explain the changes observed between lamps manufactured by different glass blowers.

5.3.2   Influence of the filling pressure

The influence of the xenon pressure had to be evaluated in order to determine the optimum filling parameters. This was achieved by filling lamps with pressures between 400 and 1000 mbar and measuring the VUV intensity with the setup described in section 5.2.2. It can be seen in figure 5.20 that the lamp intensity is increasing almost linearly with the pressure up to 1000 mbar. It is likely that the lamp output would continue to increase at
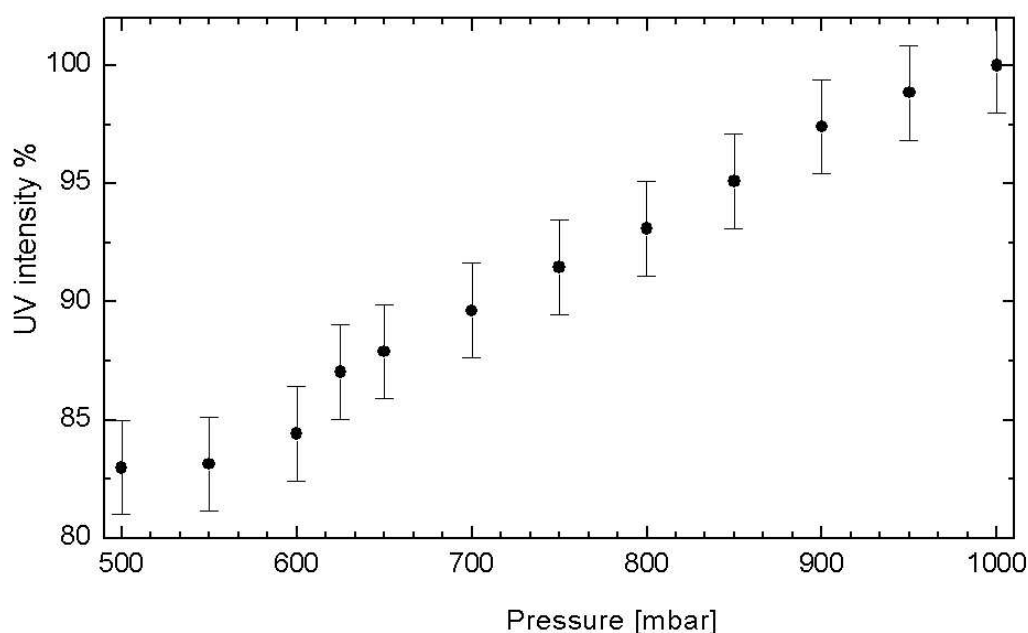
Figure 5.20: Lamp intensity as a function of the filling pressure.

higher xenon pressures. This assumption is in a way intuitive as more xenon atoms imply more excimers and therefore more emitted photons. The limit of 500 mbar at low pressure results from the formation of an electric arc going through the filling tube, between the high voltage electrode and the stainless steel of the filling station. The reason is probably that when the resistance between the electrodes of the lamp increase above a certain threshold value, due to the decreasing pressure in the lamp, the discharge occurs through a "lower resistance" path. The final selected filling pressure was 750 mbar for the following reasons. First, as the lamp will be operated in vacuum we wanted to limit the overpressure in the lamp which could lead to an explosion of the quartz envelope in conjunction with an

increased temperature and electrical breakdowns. The second reason is that the lamp is sealed by heating the filling tube at its junction with the outer quartz tube of the envelope with a blowtorch. As the junction is heated, the quartz softens and retracts due to the vacuum in the lamp, which is therefore required for this operation. This limitation can be circumvented by liquifying some xenon in the lamp with liquid nitrogen during the sealing procedure. In our case however, this operation is technically challenging because of the very limited size of our lamp. The emittance obtained with a xenon pressure of 750 mbar is in addition sufficient for the planed experiments.

5.3.3 Influence of the lamp temperature

The necessity for an efficient cooling in order to avoid extreme conditions as the one mentioned in section 5.2.4.1 is evident. However, the influence of the lamp temperature on the VUV output was investigated to quantify this effect. In order to do that, a thin thermocouple was placed between the outer electrode and the quartz envelope. The lamp was successively switched on for short time periods and then off to measure its temperature. It was not possible to measure the temperature while the lamp was in operation as the thermocouple indicated inconsistent values probably due to the influence of the applied high alternating voltage. This experiment was carried out in the small polycarbonate chamber described in section 5.2.2. The temperature increase of the lamp resulted from the heat produced by the lamp itself, therefore no heating device was necessary. As shown in figure 5.21, the lamp intensity decreases with the increasing temperature. The mechanism responsible for this process is uncertain but the involvement of some quenching processes of the excited species responsible for the VUV emission is a probable reason. An efficient cooling is therefore not only necessary to avoid overheating of the lamp but also to maintain a high and constant VUV output. On the basis of the observation of the lamp temperature at different voltages, it was decided to operate the system at 3 kV. Experiments have shown that higher voltages increase slightly the VUV output but induce a much more intense heat production. In addition, a high voltage enhances the risk of breakdowns in the UHV chamber. 3 kV constitutes therefore a fair compromise between VUV intensity and operation safety.
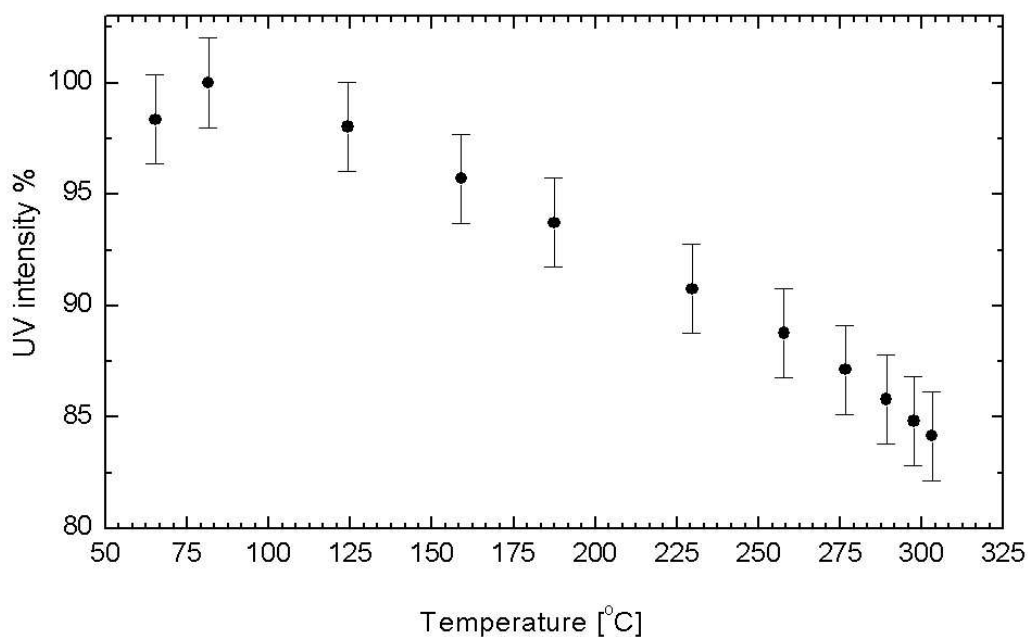
Figure 5.21: Lamp intensity as a function of the temperature

5.3.4   Influence of the voltage frequency

The influence of the voltage frequency was determined in a range from 125 to 375 kHz at a voltage of 3 kV. It was however not possible to operate the lamp below 265 kHz or above 370 kHz. As shown in figure 5.22, a maximum exists where the lamp intensity is the highest. In our case, this maximum is located at 305 kHz. This optimum frequency should in principle be determined on every system as it depends on experimental parameters like the gas pressure, the voltage applied, the width of the discharge gap or the thickness of the dielectric. The determination of all parameters influencing the voltage frequency was beyond the scope of this work and was therefore not studied in more detail. The existence of an optimum frequency is however "intuitive". In fact, the latter should not be too fast to allow the charge transfer process between the walls of the dielectric to take place and it should not be too slow to avoid the "extinction" of the plasma between consecutive discharges.
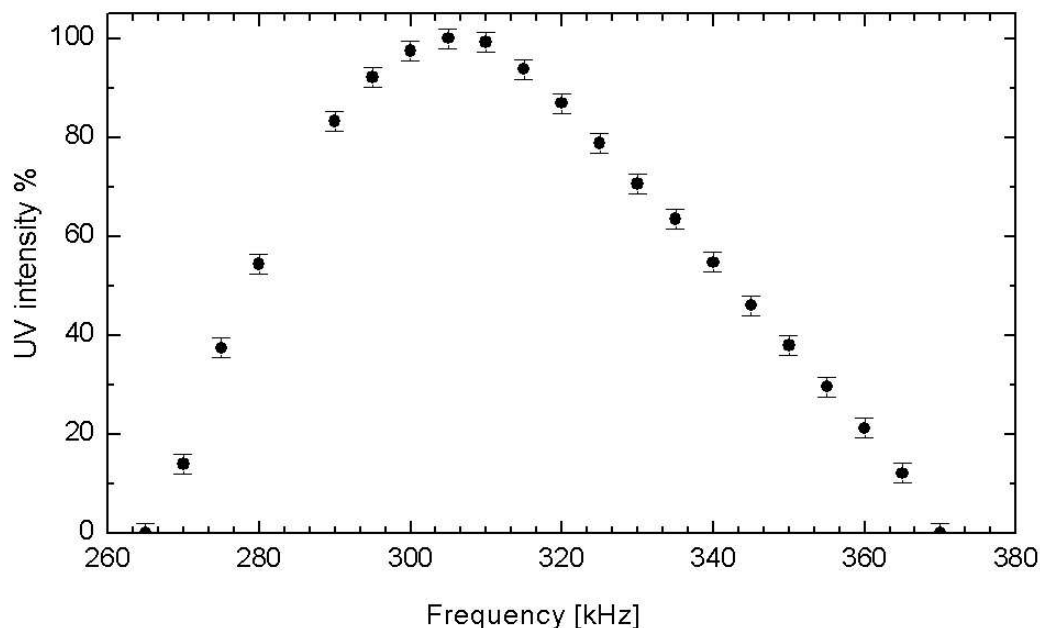
Figure 5.22: Lamp intensity as a function of the voltage frequency.

5.3.5   Stability test

The stability of the VUV output of our lamp has been studied in the UHV setup described in section 5.2.3 at two different time scales. At intermediate time scale, as it is known from the literature [176] that the VUV intensity of xenon lamps decreases during the first 10-100 hours of operation. Then at short time scale, in order to determine how long the lamp needs to stabilize its emission before starting an experiment, as it is planed to utilize the present system in the frame of catalysis experiments. In figure 5.23, it can be seen that the lamp intensity decreased almost linearly from 100 to 65 % of the original value during the first hours of operation. Very little can be found in the literature concerning this topic but it seems that the plateau reached after the initial intensity decrease is maintained during the lifetime of the lamp. In [176], a long term experiment has been carried out on a xenon lamp which did not show any intensity fluctuation of more than 0.2% during the 4000 hours following the initial drop. We can therefore reasonably assume that our lamp will follow a comparable behavior. The initial loss of VUV intensity can be explained by the creation of color centers in the lamp envelope resulting from the interaction of quartz defects and VUV
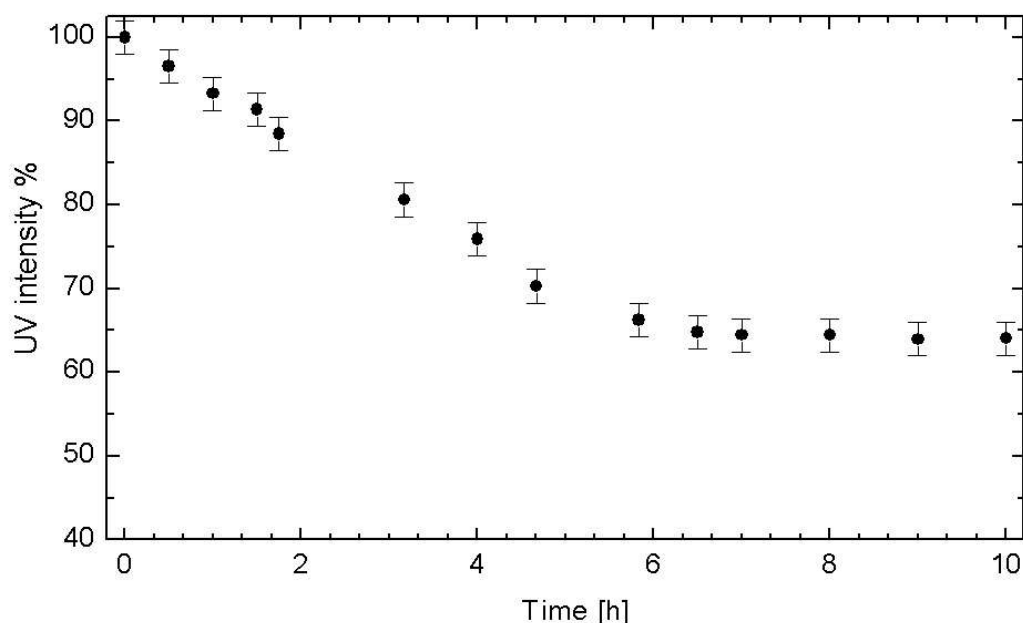
Figure 5.23: Evolution of the lamp intensity during the first 10 hours of operation.

photons. Color center are therefore irradiation induced changes of the quartz matrix. This effect is not observed for 222 nm or 308 nm lamps which means that the photon energy plays a crucial role and that the process involved starts only from a certain photon energy threshold. The absolute intensity corresponding to the 65% at which our lamp stabilized corresponds to a radiant intensity of 3.8 mW/cm² reaching our catalysts in the preparation chamber. Figure 5.24 shows the evolution of the lamp intensity immediately after being switched on. After 3 minutes, the emission intensity is stable. This duration is remarkably short if we compare it for example with mercury lamps which need a warm up period of up to 30 minutes to reach a stable UV output.

5.3.6 Lamp test

After installation of the excimer lamp in the preparation chamber, the final test to check the emission of VUV radiation consisted in detecting the formation of ozone from the interaction of oxygen molecules and VUV photons. Oxygen molecules exposed to UV radiations
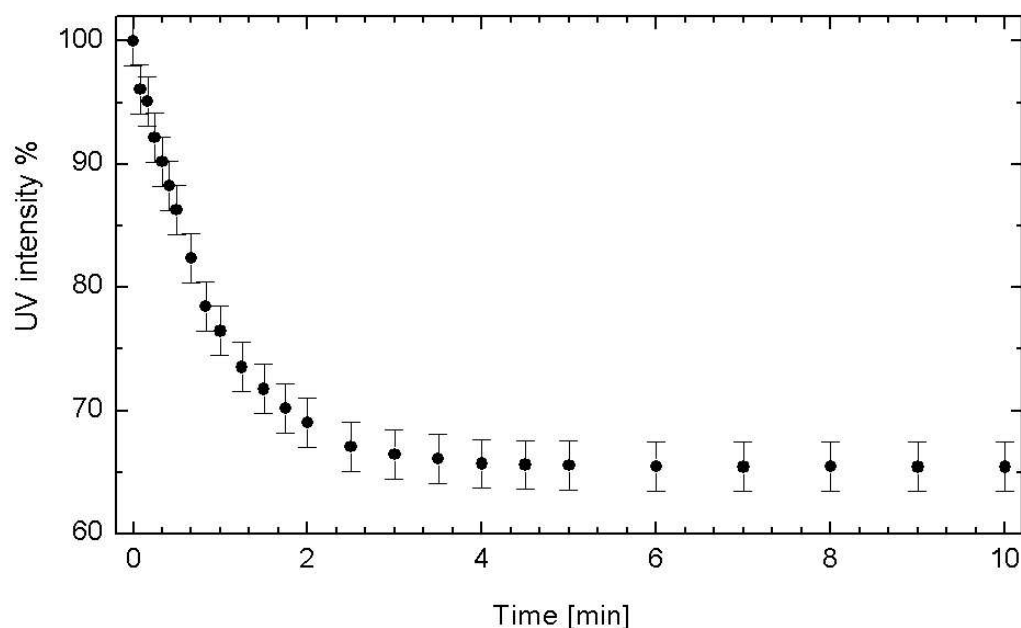
Figure 5.24: Time needed to the lamp to stabilize after being switched on.

below 240 nm are first split by the highly energetic photons according to reaction 5.9:

$$O_2 + h\nu \rightleftharpoons 2O \quad \Delta H_r = +498 \text{ kJ/mol} \tag{5.9}$$
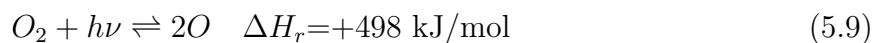
Oxygen atoms will then react with molecular oxygen to produce ozone as illustrated by equation 5.10.

$$O + O_2 \rightleftharpoons O_3 \quad \Delta H_r = -106.5 \text{ kJ/mol} \tag{5.10}$$
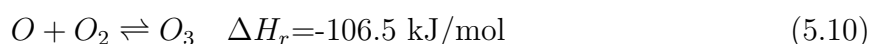
This is the basic principle of an actinometric technique [177] used for the determination of the output of UV lamps [178]. The absorption cross section of oxygen is $6 \cdot 10^{-19}$ cm^2 which means that the penetration depth in oxygen at atmospheric pressure is in the order of 0.1 cm. The output and yield of a UV source with a cylindrical geometry can be determined by placing this source in a cylindrical tube in which an oxygen stream flows. If the gap between the outer cylinder and the UV source located inside is in the order of 5-10 mm, it can be assumed that the totality of the emitted radiation is absorbed by the oxygen flow ($\sim$99% within the first 3 mm). The ozone concentration in the oxygen stream after the lamp can be measured by absorption techniques. Knowing the quantum yield of the ozone formation and the oxygen flow, the UV output and the efficiency of the lamp can be

determined. This procedure is described in details in [162].

In our case, the preparation chamber was filled with $1 \cdot 10^{-6}$ mbar of oxygen and the lamp was consecutively switch on and off for 10 seconds each time. An "on/off" cycle had therefore a total duration of 20 seconds. The signal intensity of masses 16, 32 and 48 in the gas phase of the chamber was measured simultaneously with a mass spectrometer in MID (Multiple Ion Detection) mode. The application of a mass spectrometer is the reason for the low oxygen pressure applied during this experiment. The highest pressure applicable is about $1 \cdot 10^{-4}$ mbar but it was decided to stay reasonably far from this limit. The resulting graph can be seen in figure 5.25, and a clear effect of the lamp is observed. When the lamp is switched on, the intensity of m/q 16 increases while m/q 32 decreases.
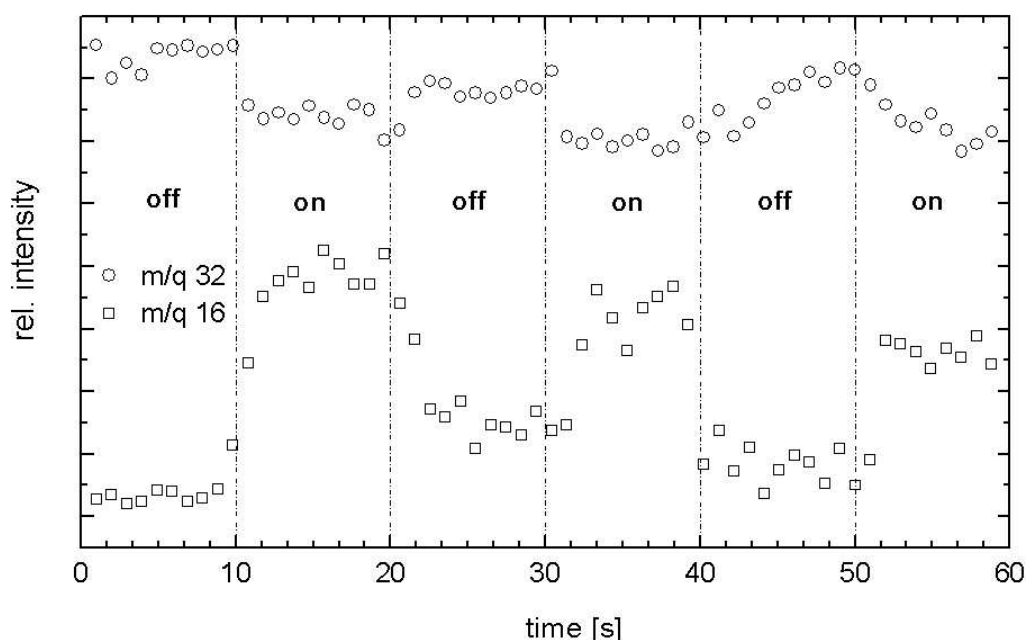
Figure 5.25: Effect of the lamp radiations on m/q=16 and m/q=32 in $1 \cdot 10^{-6}$ mbar of pure oxygen.

The opposite phenomenon takes place when the lamp is switched off. No variation could be detected from the signal corresponding to m/q 48 (ozone) which is not shown in figure 5.25. A possible reason for this behavior could be that the generated ozone decomposes in the ionization chamber of the mass spectrometer into atomic and molecular oxygen.

This would explain the increase of intensity of signal m/q 16 and the corresponding decrease of signal m/q 32. Another possible explanation is the low applied pressure where the oxygen atoms generated do not have time to recombine with oxygen molecules resulting in a marginal ozone formation. The mean free path of gas molecules at $1 \cdot 10^{-6}$ mbar is in fact in the range of few tens of meters making the collision probability in our experimental conditions relatively low. The strong point of this experiment remains that both of the above-mentioned hypotheses imply the splitting of oxygen molecules and therefore the presence of VUV photons.·

5.4   Conclusion

A miniature UHV xenon excimer lamp has been constructed and characterized. This setup is unique and no such system has been reported up to now. The lamp had to be installed in the port of a UHV chamber (DN63CF) imposing stringent requirements with regard to the compactness of the setup. The envelope of the lamp has a cylindrical geometry and is made of a high purity quartz called Suprasil®.

Different devices have been built in order to clean, fill and characterize the in-house fabricated lamps. First a filling station where the lamp can be evacuated, annealed and filled with xenon has been developed. This station includes a mobile tubular oven used to anneal the lamp at 850 ℃ before filling it with xenon.

A small polycarbonate chamber which can be attached to the filling station was built and used to test the emission of the lamp prior to sealing. This chamber, which includes a VUV detector and a high voltage feedthrough, was used to evaluate the effect of the xenon filling pressure.

The lamp was finally tested in a dedicated UHV chamber including a sapphire window through which the intensity of the radiations emitted could be quantified.

It turned out that the emittance of the lamp increases with the filling pressure between 500 and 1000 mbar. Our lamp was filled at 750 mbar, which constitutes a good compromise between VUV intensity and ease of sealing for the glass blower. The voltage frequency was found to have a strong effect on the lamp intensity and the highest emittance was obtained at 305 kHz.

The cooling of the lamp is also of high importance. First to avoid an overheating of the system which was observed during some experiments, and then because an increase of lamp temperature results in a decrease of the lamp emittance. Different cooling techniques have been evaluated and the most efficient and reliable one was found to be an indirect cooling with a water cooled inner electrode. The heat transfer between the envelope and the electrode was improved by filling the gap between them with an indium-silver alloy, which is a very soft material, providing an excellent contact between the different components of the system.

Some of the manufactured lamps emitted a characteristic green photoluminescence whose intensity was influenced by the manufacturing process and the annealing parameters. The origin of this luminescence is not clear yet but probably originates from some defects in the lamp envelope. An oxygen contamination, which also results in the emission of a green light is excluded. The lamp output stabilized after the first 10 hours of operation, probably as a consequence of the formation of color centers in the quartz envelope. After this initial step, the lamp only needs 2 to 3 minutes to reach a constant intensity after being switched on.

Chapter 6

Evaluation of the catalysts reactivity and the lamp influence for the activation of methane

6.1 Introduction

The procedure established in chapter 4 for the preparation of model catalysts will be applied in combination with the excimer lamp in order to evaluate both the influence of the lamp and the catalysts composition. As mentioned in the introduction of this work, a wavelength of 172 nm (7.2 eV) is not sufficient for a direct gas phase activation of CH_4. However, it has been already reported in the literature that the activation of methane could be enhanced on metal surfaces by photons having energies lower than 9 eV, energy at which the cross section of methane starts to be significant. Rizzo et al. showed that the activation of methane can be dramatically enhanced on a Ni(100) single crystal by exciting specifically vibrational modes through irradiation of a molecular beam with an IR laser [179][180]. Gruzdkov et al. came to the conclusion that CH_4 molecules physisorbed on a Pt(111) single crystal at 40 K could be photodissociated with a 193 nm laser [37][181]. Similar experiments have been carried out on Cu(111) at 35 K [182], Pd(111) at 40 K [183] and Pt(111) at 40 K [184] by Watanabe et al. who also reported an enhanced activation of the physisorbed methane molecules. In fact, they could observe the formation of a peak

specific to irradiated samples in the TPD spectra. This peak was attributed to the desorption of ethylene resulting from the recombination of methyl groups formed upon sample irradiation. The processes through which the photoactivation of methane takes place on surfaces is however not yet fully understood.

Heterogeneous photocatalysis is an emerging technique and most of the reported experiments deal with mercury lamps, halogen lamps and lasers [185]. As described in section 5, the intrinsic properties of these light sources make them unsuitable for industrial scale applications. The use of excimer lamps could help to overcome this limitation.

Catalytic processes are usually described in terms of *ensemble effect* or of *ligand effect*. The former is associated to a number of surface atoms needed for the catalytic event to occur and the latter corresponds to the electronic modifications resulting from the interactions between the different components of the system. Additionally, a *bi-site effect* in which different components of a catalyst play a specific role with regard to the partner of a given reaction was suggested. This theory has been applied for explaining the synergetic effect of some bimetallic alloys. As a matter of fact, bimetallic catalysts often exhibit distinctly different properties from those of the pure metals. They offer the opportunity to develop new catalytic materials with enhanced activity, selectivity or deactivation resistance [186]. This area of research started to gain in importance in the 1960's with hydrocarbon reforming catalysts displaying higher activities compared to the traditional monometallic materials [187]. Currently, bimetallic catalysts are extensively investigated and used for many catalytic [188] and electrocatalytic applications [189]. The synergetic effect is most pronounced when the admetal coverage is in the sub-monolayer to monolayer regime [190]. It is however still very difficult to predict the electronic and chemical properties of bimetallic catalysts. This field is presently intensively investigated by many research groups with promising achievements [191][192][193]. The modifications of the electronic and chemical properties of bimetallic catalysts is often understood as resulting from mainly two different factors. The first one results from the formation of hetero-atom bonds which induces changes in the electronic environment of the metal surface. This modified environment provokes modifications in the electronic structure of the metal particles through the so-called *ligand effect*. The second factor is connected with a *geometrical effect*. In fact, the different size, bond length and structure of metals give rise to strains in bimetallic systems.

Such strains alter the electronic structure of the species involved through variations in the orbital overlap, what has a direct influence on the catalytic activity of a material.

The present chapter, is essentially dedicated to the evaluation of the influence of the excimer lamp irradiation on the activation of CH_4 over Ni-Pd/$\gamma - Al_2O_3/Si$ model catalysts which have been developed for this project. The influence of the catalysts composition on the reactivity of the system in the case of different gas mixtures will also be addressed.

6.2 Experimental

All the experiments presented in this chapter have been performed in the preparation chamber. XPS spectra were recorded in the analysis chamber described in section 4.2.

The substrates have been prepared as described in section 4. Evaporation rates of nickel and palladium have been determined with the quartz crystal microbalance. Well defined amounts of metal were deposited on the substrates at 623 K for nickel and 473 K for palladium. The sample-evaporator distance was set equal to the distance between the QCM and the metal evaporator previously applied during the calibration of the evaporation rate. The evaporation rate was set to 0.5 Å/min for nickel and 0.8 Å/min for palladium as defined in section 4.3. Catalysts have been prepared by depositing an amount of metal corresponding always to a total of 1 average monolayer on cleaned $\gamma - Al_2O_3/Si$ substrates. The monometallic catalysts tested consisted of 1 monolayer Pd and 1 monolayer nickel. Bimetallic samples have been prepared by evaporating nickel and palladium in variable proportion on cleaned substrates. The detailed composition of the catalysts investigated is described in table 6.1. The cells of this table contain first a number, 1 or 2, indicating

Table 6.1: Description of the bimetallic catalysts tested.

	0.8Ni/0.2Pd	0.5Ni/0.5Pd	0.2Ni/0.8Pd	0.8Pd/0.2Ni	0.5Pd/0.5Ni	0.2Pd/0.8Ni
Ni	1) 0.8ML	1) 0.5ML	1) 0.2ML	2) 0.2ML	2) 0.5ML	2) 0.8ML
Pd	2) 0.2ML	2) 0.5ML	2) 0.8ML	1) 0.8ML	1) 0.5ML	1) 0.2ML

the order of evaporation and in the second position the amount of metal corresponding to a defined coverage in monolayer, assuming a layer by layer growth. A contraction of these information which will be used to refer to the different samples is given in the horizontal row of labels in table 6.1. For example, the catalyst 0.8Ni/0.2Pd was prepared by evaporating first an amount of nickel corresponding to 0.8 ML and then an amount of palladium equivalent to 0.2 ML.

During the thermal programmed experiments, the sample holder receiving station of the chamber was rotated at an angle of 67.5 degrees with regard to the horizontal, in order to have the catalyst surface oriented between the excimer lamp and the QMS nozzle. The latter was then moved very close to the sample as described in section 3.1.6 for the detection of species desorbing from the catalyst surface. The lamp was also moved in direction of the sample, up to a distance of 55 mm which is the minimum before having an interaction between the QMS nozzle and the upper part of the lamp housing. This interaction can be visualized looking at figure 3.3 where the lamp and the TPR nozzle are labeled with number 2 and 3 respectively. It is noteworthy that the actual setup does not give access to the conversion and selectivity of the catalysts. As a matter of fact, even when the nozzle is moved close to the catalyst surface, as shown in figure 6.1, most of the gas pumped into the nozzle consists of unreacted species coming directly from the chamber's gas phase. The reaction products are therefore strongly diluted when they are detected by the QMS. This allows however to compare different catalysts with regard to their reactivity.

The gas mixtures were prepared in the gas distribution system described in section 3.1.7. The lines were thoroughly flushed before filling them with the reactant gases up to a pressure of 1.5 bar. This pressure was maintained at a stable value by the regulator mentioned in section 3.1.7. A stable pressure in the lines before the PC is essential as variations would inevitably be reflected in the pressure of the preparation chamber. Experiments were carried out with pure methane and mixtures containing 50% CH_4/50% CO_2 and 95% CH_4/5 % O_2. The gas was introduced in the PC with the leak valves shown in figure 3.9 up to a total pressure of $8\text{-}9 \cdot 10^{-5}$ mbar, close to the limit of 10^{-4} mbar allowed by the QMS detector. Some selected m/q signals were recorded in MID mode and after a stabilization time of 5 minutes, the catalyst temperature was raised linearly at a rate of 20 K/min from RT to 773 K. At the end of the ramp, the final temperature was maintained for about
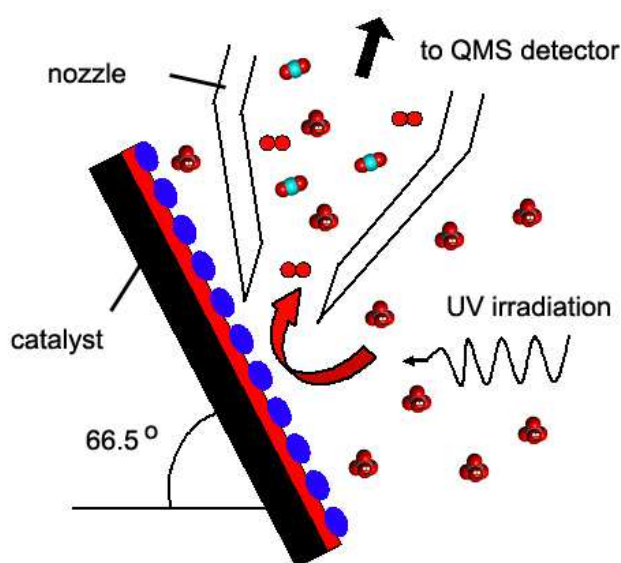
Figure 6.1: Sketch of the setup configuration during a thermal programmed reaction experiment.

15 minutes and then the leak valve was closed. The sample was cooled down to <373 K and transferred to the analysis chamber to be analyzed by XPS. In some cases, the catalysts appeared to be slightly charged during XPS analyses (<2 eV). Due to the low intensity of the carbon signal in some experiments, the spectra could not be reliably charge corrected with regard to the typical carbon binding energy of 284.5 eV. Instead, the aluminum 2p signal was set to 74.2 eV which corresponds the Al2p peak position when C1s is set to 284.5 eV.

The different catalysts described in table 6.1 were tested first without lamp irradiation in experiments called "dark experiments" and then with the lamp irradiating the catalyst surface in so called "bright experiments".

6.3 Results

6.3.1 Carbon uptake of the catalyst surface

6.3.1.1 Methane

In order to evaluate the influence of the lamp on the activation of methane over the different catalysts prepared, the surface concentration of carbon was determined by XPS at the end of each thermal programmed reaction. The experiments were initially carried out with pure methane as described in the previous section. The results obtained are summarized in figure 6.2. The experiments with catalysts 0.8Ni/0.2Pd, 0.2Pd/0.8Ni, 0.2Ni/0.8Pd and
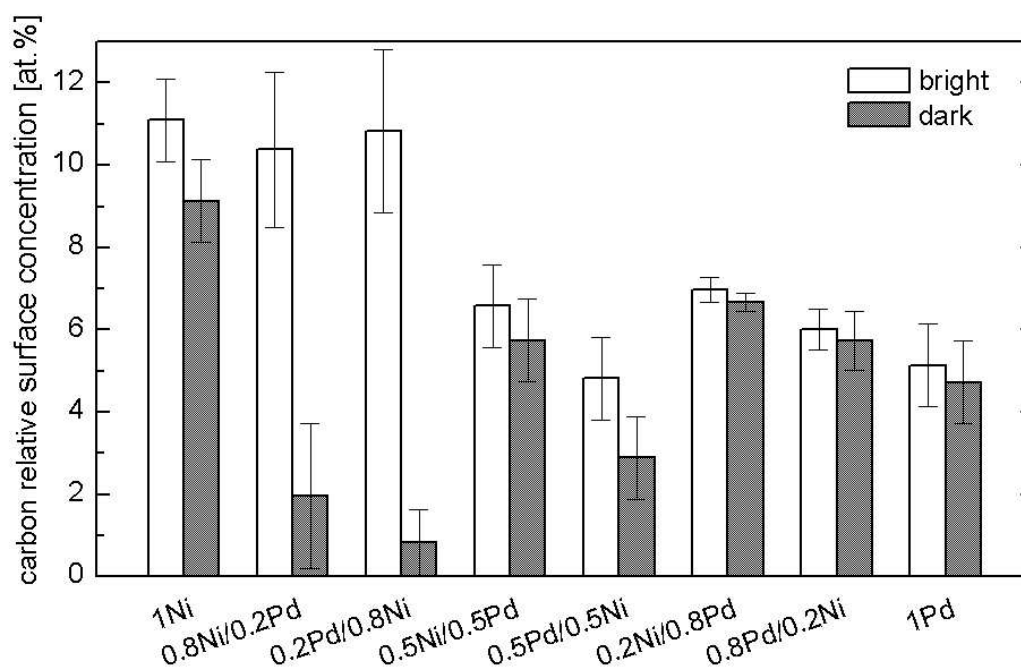
Figure 6.2: Relative carbon concentration in atomic % after TPR experiments with pure methane at $9 \cdot 10^{-5}$ mbar over various catalysts.

0.8Pd/0.2Ni have been repeated twice, with and without lamp irradiation, in order to evaluate the reproducibility of these measurements. The surface concentration of carbon for these catalysts (fig. 6.2) corresponds to the average of the two measurements. The standard deviation of each of the eight pairs of carbon concentration were then calculated

separately with equation 6.1, which is valid for small sets of data [194]:

$$s = \sqrt{\frac{\sum_{i=1}^{N}(x_i - \overline{x})^2}{N-1}} \qquad (6.1)$$

It is scientifically questionable to calculate a standard deviation over only two points. However, if we compare in figure 6.2 the eight standard deviations obtained, it appears that the variations between them is small, which indicates a good reproducibility of the experiments. The error bars of the non repeated values correspond to the average of the standard deviations calculated from the repeated experiments.

In figure 6.2, it is evident that the various prepared catalysts have clear specific reactivities, even if it is difficult to derive a general trend related to their composition. It is noteworthy that the surface concentration of carbon is for each catalyst higher in the bright experiment than in the dark experiment, even if in some cases the difference of concentration lies within the experimental error. This difference is obvious for pure nickel, 0.5Pd/0.5Ni and especially in the case of 0.8Ni/0.2Ni and 0.2Ni/0.8Pd indicating an enhanced methane activation when the catalyst surface is irradiated by 172 nm photons. Such a phenomenon has already been observed however not at the same wavelength and not over Ni and the bimetallic catalysts investigated here. It is remarkable that methane seems to be photodissociated at wavelength above 140-150 nm where there is no appreciable photoabsorption cross section for CH_4 in the gas phase. As shown in figure 6.3, the photoabsorption cross section of methane drops sharply above 130 nm and is equal to 10^{-23} cm^2/molecule at 172 nm. Two mechanisms are usually suggested in order to explain the photodissociation of adsorbates on metal and semi-conductor surfaces. The first one is known as *direct electronic excitation* which becomes possible due to a the red shift of absorption bands of the gas phase molecules resulting from the substrate-adsorbate interaction. The second mechanism is called *surface mediated excitation* or *dissociative electron attachment* (DEA). It concerns the transfer to the adsorbed molecule of a hot electron which is created by a VUV excitation of the substrate. The adsorbate becomes therefore transiently charged and undergoes photochemical processes [196]. Both mechanisms have been proposed to explain the activation of methane on Pt(111) [37][181]. However it has been suggested that based on energetic considerations a direct activation mechanism is more likely over Pt(111) and Pd(111) [183]. It is difficult to say if these considerations based on single crystals can be
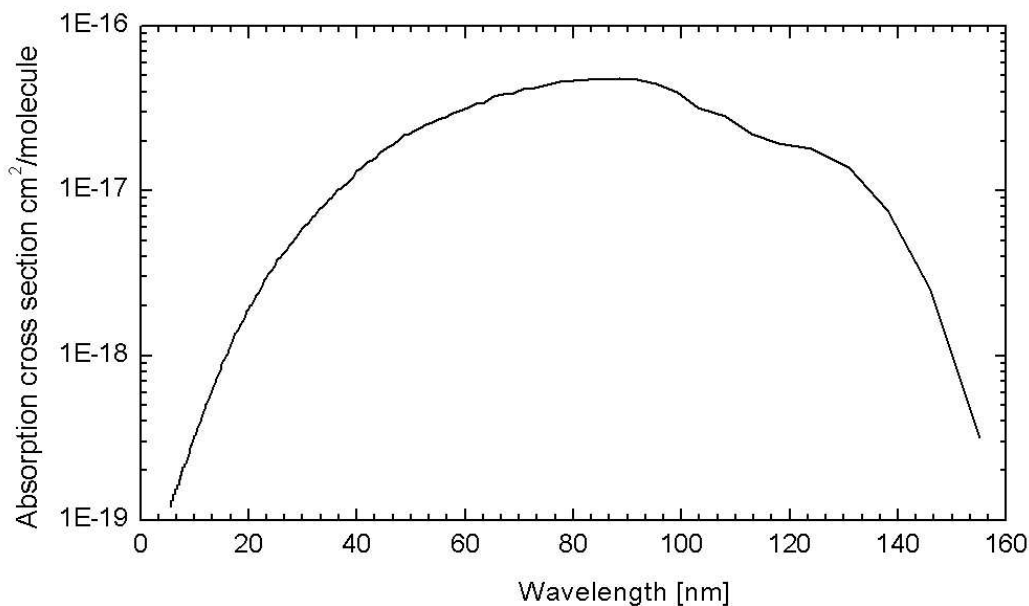
Figure 6.3: Absorption cross section of methane from Au et al. [195].

translated to our system but the elucidation of the mechanism involved in our case would require further investigations.

It is also interesting to notice in figure 6.2 that for the bimetallic samples, the difference of C concentration between the bright and the dark experiments increases with the nickel content. This difference is included within the experimental error for both catalysts made of 80% Pd and 20% Ni, but it is more evident for the 50% Ni-50% Pd samples and is most visible for both 80% Ni-20% Pd catalysts. Finally, each pair of catalysts characterized by a similar absolute composition but differing in the deposition order of the two metallic components, have a comparable reactivity in the bright as well as in the dark experiments. The fact that the evaporation order of Pd and Ni does not seem to play a major role on the catalysts properties indicates that the surface structure and morphology should in principle be similar independently whether Ni or Pd is deposited first. This is only possible if the metals diffuse or the surface reconstructs to reach a situation corresponding to the thermodynamic equilibrium. The resulting surface can then be made of homogeneously alloyed particles (bulk alloy) or clusters containing Ni and Pd but with internal concen-

tration gradients due to segregation phenomena. Both cases have been reported in the literature for different systems.

After the TPR experiments, the surface of the catalysts was analyzed with AES and the ratio of the nickel concentration over the palladium concentration was calculated and is shown in table 6.2. The first row of this table indicates the theoretical concentration ratio

Table 6.2: Concentration ratio of Ni to Pd determined by AES.

	80% Pd-20% Ni	50% Pd-50% Ni	20% Pd-80% Ni
theoretical ratio	0.25	1	4
Ni evap. first	0.037±0.003	0.23±0.02	1.23±0.09
Pd evap. first	0.037±0.003	0.25±0.02	1.11±0.08

corresponding to the amounts of nickel and palladium deposited. The measured concentration ratios of the catalysts characterized by the same absolute composition are shown in the different columns. It is noteworthy that no significant difference can be observed between catalysts on which nickel or palladium was evaporated first. This is in accordance with the observation, that based on the carbon uptake of the catalysts, the reactivity seems to be independent on the metal deposition order. Moreover, it appears that the measured ratios are significantly lower than the theoretical values. This could result from a diffusion of palladium from the bulk to the surface of the clusters, leading to a locally higher concentration of palladium than the average value shown in the first row of table 6.2. Such a phenomenon has already been predicted by theoretical calculations and was reported in the literature [97]. In fact, based on DFT calculations, Christensen et al. suggested that in the case of Ni-Pd alloys, palladium segregates to the surface. This phenomenon was observed by L'Argentiere et al. [186] who noticed a depletion of nickel on Ni-Pd/Al_2O_3 catalysts upon annealing at 773 K [94]. Additionally, Nascente et al. deposited palladium over Ni(111) and reported the formation of a stable surface Ni-Pd alloy upon annealing at 923 K [197]. Carazzolle at al. studied the complementary system, that is nickel deposited over Pd(111) and observed the complete diffusion of nickel into the bulk upon annealing at 873 K. The data obtained in this work support these findings, i.e. the formation of a

palladium shell surrounding a nickel core leading to identical metal clusters, independently whether nickel or palladium was evaporated first. This can therefore explain the similar activity of the catalysts of same average composition which was observed in this work.

6.3.1.2 Methane and carbon dioxide

The experiment described in the previous section was repeated with a mixture of 50% CH_4 and 50% CO_2. Carbon dioxide absorbs weakly at 172 nm with an absorption cross section of 10^{-20} cm²/molecule, it is therefore not expected to react significantly in the gas phase at the pressure applied. Three of the most active catalysts in the case of pure methane have been tested here. However, as shown in figure 6.4, the final carbon concentrations were very low. This indicates a limited reactivity with this gas mixture, which was confirmed during thermal programmed reaction experiments where the QMS signals corresponding to reaction products had a very low intensity. Further investigations were therefore not pursued.

The reason for this low activity could not be clearly established. The catalysts surface was not oxidized after the reactions and no traces of contaminants except carbon could be detected. The position of the C1s peak was around 284.5 eV corresponding to amorphous carbon and the formation of carbonates which could block the active sites on the surface can be excluded. In fact, the C1s binding energy corresponding to carbonates, is around 289 eV, allowing an easy distinction of these species from other carbon containing molecules. The highest carbon concentration was obtained with the catalyst 0.2Ni/0.8Pd which appeared to be more reactive than the others. Even if the difference of carbon concentration between the bright and the dark experiments for the catalyst 0.2Ni/0.8Pd is not negligible, it is difficult to assign it to a real lamp effect as all the values are within the experimental error.

6.3.1.3 Methane and oxygen

As stated previously, the different model catalysts have also been tested with a mixture of 95% methane and 5% oxygen. The carbon uptake of the surface upon reaction was determined and is shown in figure 6.5. The most active catalyst for the dark experiments is by far 0.8Ni/0.2Pd. It is noteworthy that the carbon concentration in figure 6.5 is always

Figure 6.4: Relative carbon concentration in atomic % after TPR experiments with 50% methane and 50% carbon dioxide for various catalysts at $P_{tot}=9\cdot10^{-5}$ mbar.

distinctly lower in the bright experiments than in the dark ones. This however does probably not reflect a lower reactivity. As it has been shown in section 5.3.6, oxygen absorbs moderately 172 nm photons with a photoabsorption cross section of $6\cdot10^{-19}$ cm^2/molecule. Upon VUV irradiation, oxygen molecules are split into radicals which possibly recombine into ozone. It is therefore likely that the oxygen species formed in the gas phase oxidized the carbon deposits on the catalysts. This assumption is supported by temperature programmed reaction experiments where many reaction products could be observed, which was not the case for methane and carbon dioxide. It is finally interesting to notice that in the dark experiments, based on the carbon uptake of figure 6.5, the bimetallic catalysts seem to exhibit a higher reactivity than the pure nickel and palladium samples.
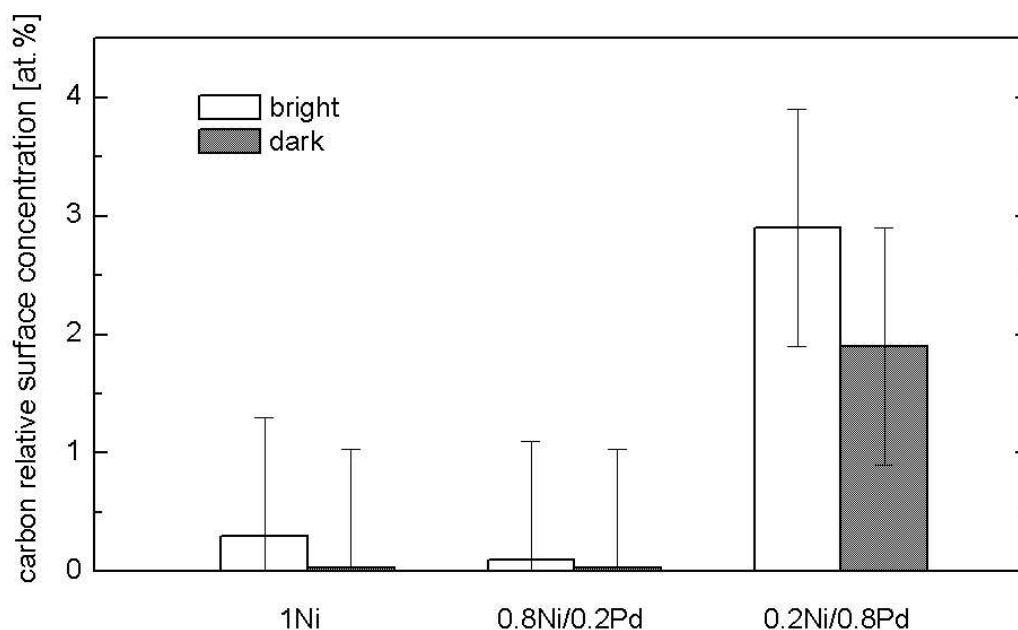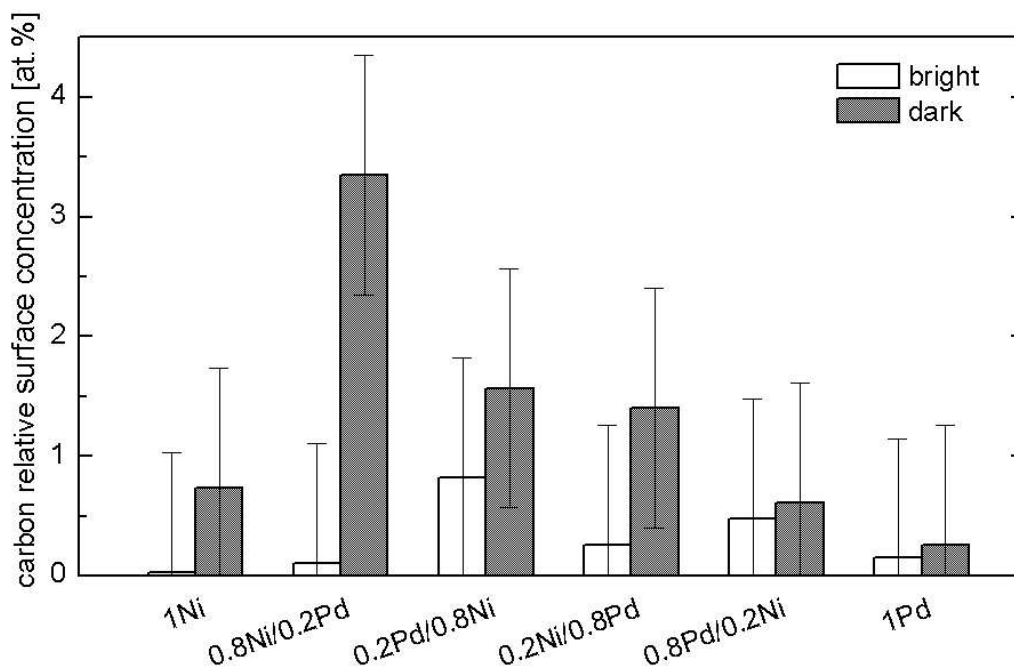
Figure 6.5: Relative carbon concentration in atomic % after TPR experiments with 95% methane and 5% oxygen for various catalysts at P_{tot}=9·10^{-5} mbar.

6.3.2 Thermal programmed reaction experiments

6.3.2.1 Methane

The reactivity of the different catalysts was evaluated through thermal programmed reaction experiments as illustrated in figure 6.1. A selection of m/q signals was recorded in MID mode while ramping the catalysts from RT to 773 K. As the gas mixtures contained a large variety of highly diluted hydrocarbons, it was not possible to identify and quantify each of them. The experiments were therefore focused on some m/q signals specific to different families of compounds. These signals were then quantified by measuring the variation of intensity between the beginning of the temperature ramp and the end of the experiment. A blank TPR experiment was carried out and the corresponding signals were subtracted from the signals obtain with catalysts. This allows to cancel the influence of factors not related to the catalysts like gas contaminants or reactions taking place in the QMS itself. A typical signal obtained during one of the TPR experiments is shown in
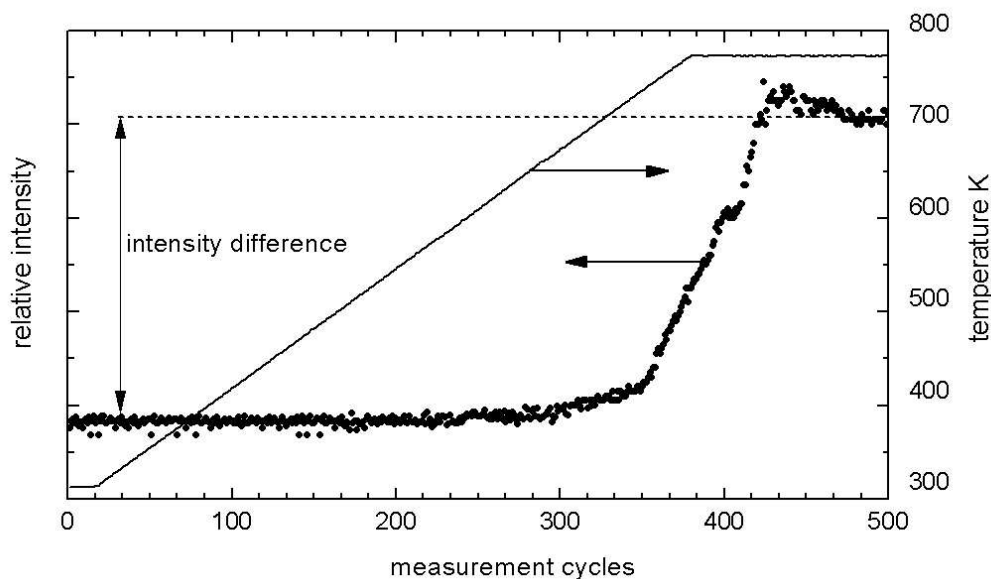
Figure 6.6: Illustration of the procedure applied for the determination of the signal intensity difference between the beginning and the end of thermal programmed reaction experiments.

figure 6.6 where the quantification procedure is illustrated. The initial and final values of the signal intensity were determined from an average of 10 to 20 points.

In the case of pure methane, the main reaction products detected were hydrogen, corresponding to mass 2, C2 hydrocarbons identified with mass 30 and small amounts of C3 hydrocarbons characterized by a signal at mass 39. In fact, the only products which could be formed from pure methane in our system exhibiting a signal at m/q=30 are ethane and propane. However, mass 30 has a relative intensity of 26% compared to the parent peak in the case of ethane and only 2% in the case of propane. Therefore, as ethane is expected to be produced in larger amount than propane, mass 30 is considered as coming exclusively from ethane. Similarly, mass 39 may originate from propane, propene and butane. However, butane is not expected to be formed in significant amounts in our system and was therefore neglected. The values obtained for masses 2, 30 and 39 are shown in figures 6.7, 6.8 and 6.9 respectively. In order to evaluate the error on these measurements, 8 TPR experiments have been repeated twice. They concerned the same catalysts as in section 6.3.1.1, i.e. 0.8Ni/0.2Pd, 0.2Pd/0.8Ni, 0.2Ni/0.8Pd and 0.8Pd/0.2Ni in each case with

Figure 6.7: Variation of the intensity of m/q=2 during TPR experiments with pure methane in the case of different catalysts at P_{tot}=9·10^{-5} mbar.

Figure 6.8: Variation of the intensity of m/q=30 during TPR experiments with pure methane in the case of different catalysts at P_{tot}=9·10^{-5} mbar.
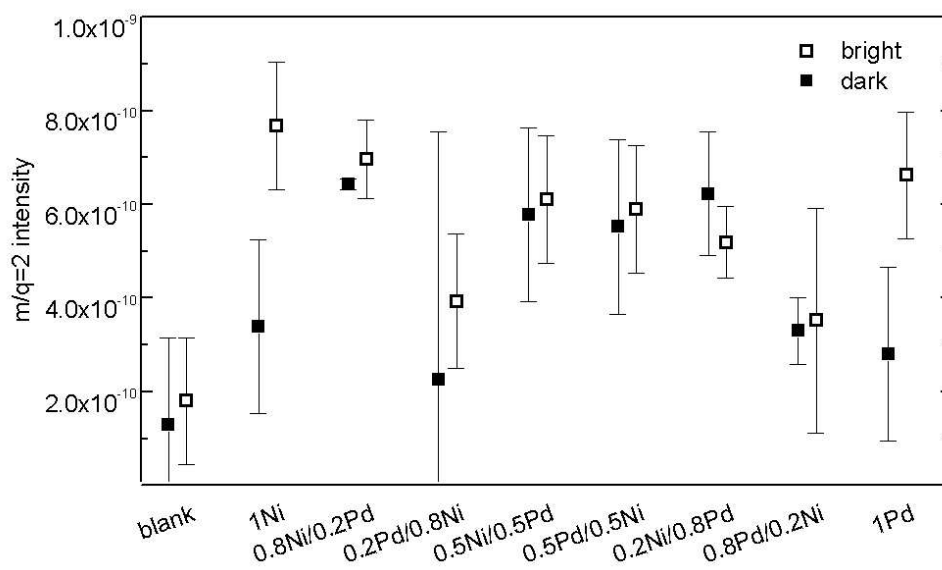
Figure 6.9: Variation of the intensity of m/q=39 during TPR experiments with pure methane in the case of different catalysts at P_{tot}=9·10^{-5} mbar.

and without VUV irradiation. As shown in figure 6.6, the determination of the intensity change itself is accurate due to the low signal to noise ratio of the QMS signals. This is also valid for low intensity QMS signals which were measured with a higher "sampling time" in order to maintain a constant signal to noise ratio. The large standard deviation shown in figure 6.7 is therefore originating from the reproducibility of the experiments. Many experimental parameters have a crucial influence on the final data. It is for example possible that the energy scale of the mass spectrometer drifts with time or with the lab temperature which varies by more than 10 degrees between day and night. The position of the TPR nozzle has also a major influence. It was observed during experiments that moving the TPR nozzle slightly away from the catalyst resulted in an increase of the methane signal together with a drop of the signals corresponding to the formed products. The positioning of the nozzle is in principle well reproducible due to the design of the system described in section 3.1.6. However, it is possible that the position of the sample holder receiving station varies slightly during experiments. This receiving station is rotatable and contains different movable parts which could cause some variations of the sample holder position. Finally, a drift of the gas pressure has been observed during some experiments. This drift

can result from small changes of the pressure in the gas lines before the chamber or directly from the leak valve which regulates the pressure in the chamber. Due to the significant errors related to the experiments presented here, the corresponding results must be considered with caution.

A common trend to all three sets of data shown in figures 6.7, 6.8 and 6.9 is that the intensity of signals corresponding to the bright experiments are almost always higher than the corresponding dark experiment signals. This fact supports the photo-enhanced methane activation, even if in some cases the difference of intensity is not significant considering the error bars. It seems that the lamp especially enhances the production of hydrogen over nickel and palladium (fig. 6.7) while the formation of C2 and C3 hydrocarbons is favored over Ni, γ-Al$_2$O$_3$ and the bimetallic catalysts containing 80% Ni and 20% Pd (fig. 6.8 and 6.9). From signals 30 and 39, it is also noteworthy that there is a tendency for a more pronounced difference of intensity between dark and bright experiments for catalysts with an increasing nickel content. This fact is in agreement with the surface carbon uptake results presented in section 6.3.1.1.

6.3.2.2 Methane and oxygen

The different catalysts have also been tested with a mixture of 95% methane and 5% oxygen. The main products observed in this case were hydrogen, water, CO, CO$_2$ and some C2 hydrocarbons. No C3 hydrocarbons could be detected as in the case of pure methane. Mass 2 was as previously described assigned to hydrogen. Mass 28 was attributed to carbon monoxide even if several hydrocarbons also contribute to the intensity of this signal. These hydrocarbons are mainly ethane, ethylene and propane. As already pointed out, no C3 hydrocarbons could be detected and the amount of C2 hydrocarbons appeared to be much lower than carbon monoxide, which supports the validity of the assignment of mass 28 to CO. C2 hydrocarbons were again related to the intensity of mass 30, for the same reasons as described previously. The data obtained for signals 2, 28 and 30 are shown in figure 6.10, 6.11 and 6.12 respectively. The large error bars make the interpretation of the data complicated. For all three analyzed masses, palladium seems to be the most active catalyst in the bright experiments. A possible reason for this higher activity is the
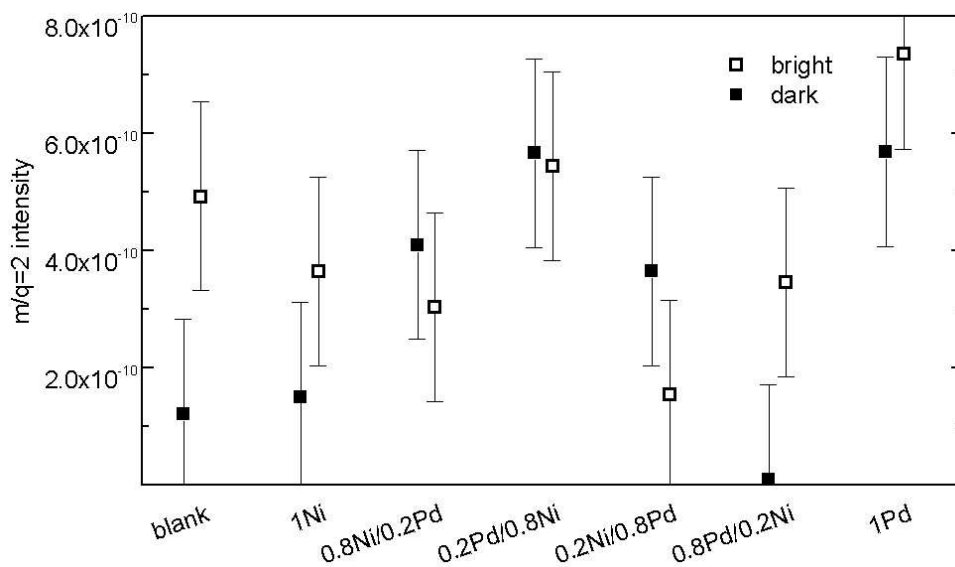
Figure 6.10: Variation of the intensity of m/q=2 during TPR experiments with 95% methane and 5% oxygen in the case of different catalysts at P_{tot}=9·10^{-5} mbar.
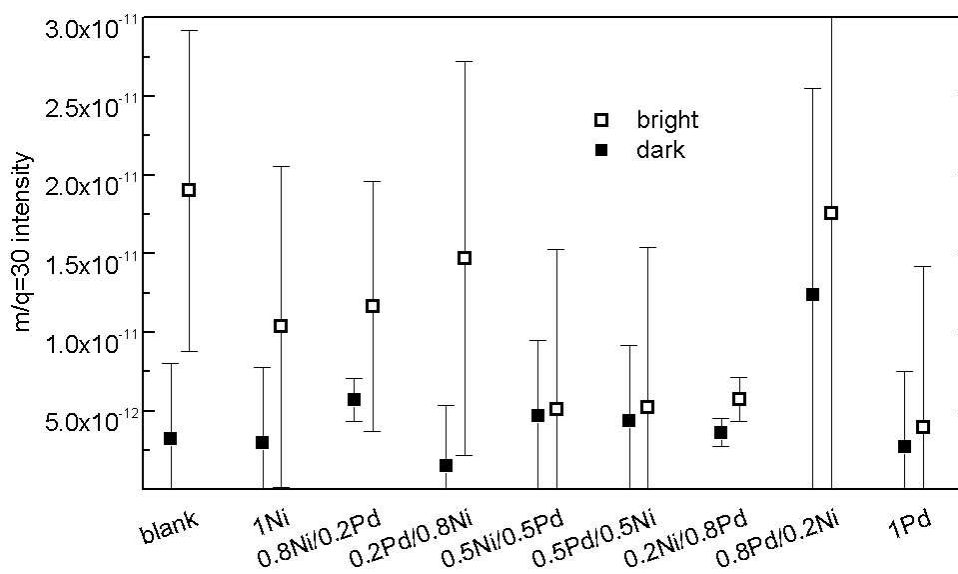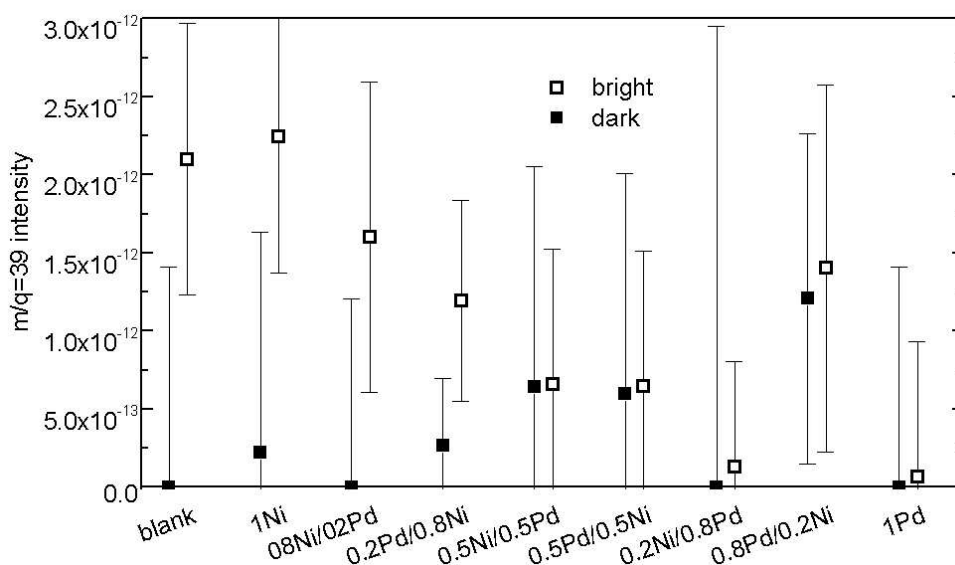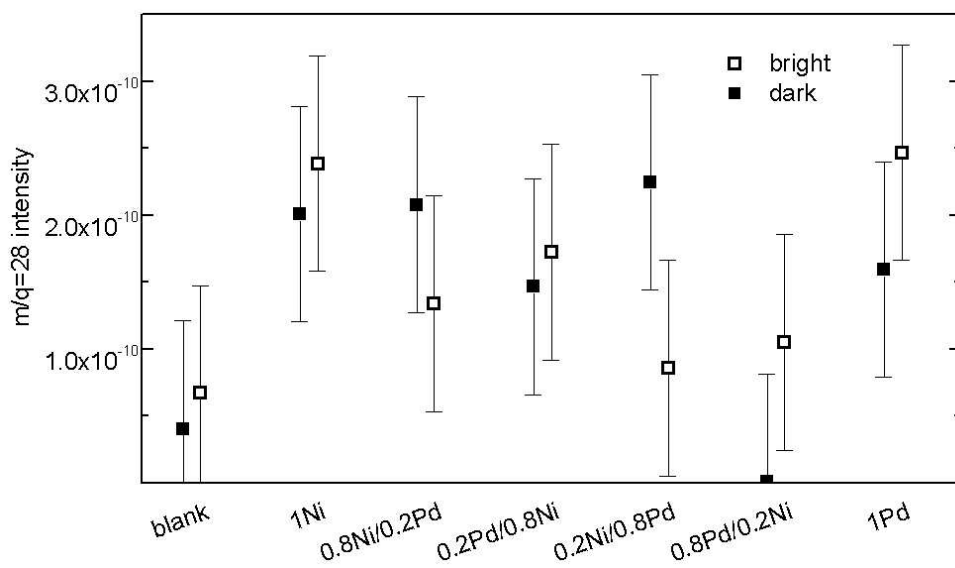

Figure 6.11: Variation of the intensity of m/q=28 during TPR experiments with 95% methane and 5% oxygen in the case of different catalysts at P_{tot}=9·10^{-5} mbar.
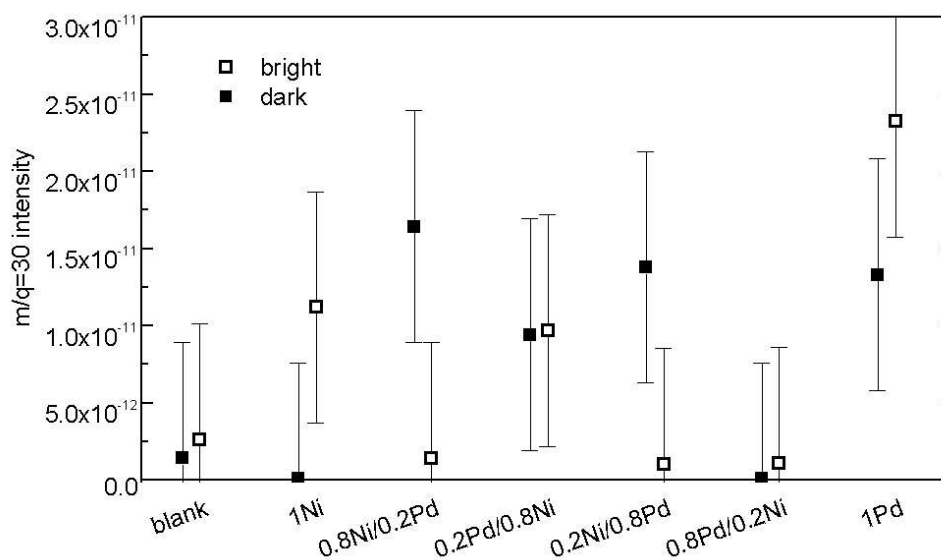
Figure 6.12: Variation of the intensity of m/q=30 during TPR experiments with 95% methane and 5% oxygen in the case of different catalysts at $P_{tot}=9{\cdot}10^{-5}$ mbar.

oxidation resistance of palladium with regard to the oxidizing atmosphere applied in this experiment. The formation of oxygen radicals induced by VUV irradiation in an oxygen atmosphere has in fact been observed in section 5.3.6. For all catalysts, nickel appeared to be partly oxidized during the reaction. For samples composed of 80% Pd and 20% Ni, an important part of the nickel, corresponding to 80% of the total evaporated amount on the substrate, was oxidized to $Ni(OH)_2$. In catalysts containing 20% Pd and 80% Ni, the proportion of oxidized nickel decreased to 50% while interestingly, the pure nickel catalyst used for the bright experiment was completely oxidized. The nickel region corresponding to these different cases is shown in figure 6.13. It is noteworthy that the nickel catalyst was only oxidized in the bright experiment while the bimetallic catalysts did not exhibit any appreciable difference of oxidation level between dark and bright experiments. This fact supports the suggestion that the final cluster "structure" does not depend on the deposition order of the two metals. The partial oxidation observed in the case of the bimetallic catalysts could be explained by the formation of a palladium shell on the clusters due to segregation processes as suggested previously, which would "protect" the inside of the clusters from total oxidation. As suggested by Nascente et al. [197], it is possible
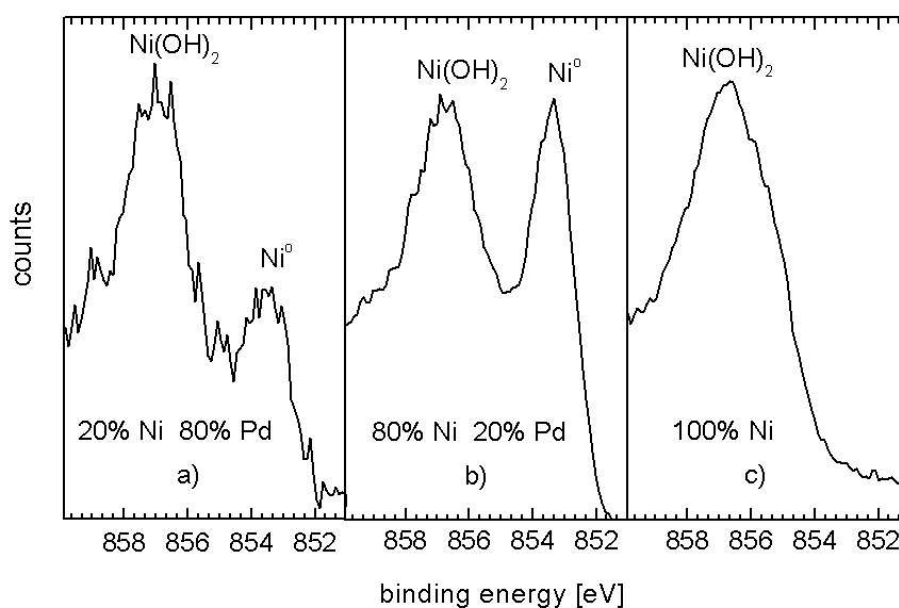
Figure 6.13: Post reaction XPS spectra of the Ni2p$_{3/2}$ region after TPR experiments with 95% methane and 5% oxygen at P$_{tot}$=9·10^{-5} mbar for catalysts composed of a) 20% Ni-80% Pd b) 80%-Ni 20% Pd and c) 100% Ni.

that the palladium layer on the surface of the clusters incorporates also some nickel and corresponds therefore to a Ni-Pd surface alloy. The nickel present on the surface of the clusters could therefore correspond to the nickel hydroxide peak of the XPS spectra shown in figure 6.13.

It is noteworthy that the blank sample exhibited a higher activity than most of the other catalysts for the production of hydrogen in the bright experiment. It is however possible that the bimetallic catalysts as well as nickel were partly deactivated due the oxidation phenomenon described previously. In addition, contrary to what has been suggested earlier, the metal deposition order seems to have an influence in these experiments, as shown in figure 6.10, 6.11 and 6.12 for the bimetallic catalysts. The differences are however always included in the experimental errors and these observations would therefore need to be confirmed.

A more reliable quantification could be obtained by working at higher pressure and by analyzing the exhaust gas with a GC-MS unit. As a matter of fact, due to the very low

sticking coefficient of methane over most surfaces and the connected low reaction rates in vacuum, impurities in the reactant gases like CO and higher hydrocarbons interfere with the detection of the real reaction products. Moreover, the quadrupole mass spectrometer appears not to be sufficient to distinguish between complex mixtures of hydrocarbons and a gas chromatograph would therefore be a major asset to a more detailed evaluation of the reactivity of these catalysts. Some setup modifications are proposed in the outlook in order get access to the conversion and the selectivity of the catalysts investigated.

6.3.3 Photo-enhanced reactivity

An additional support to the suggested photoassisted activation of methane by 172 nm photons was gained from an experiment with pure methane on catalyst 0.8Ni/0.2Pd in which the lamp shutter was successively opened and closed. Methane was introduced in the chamber up to a pressure of $1 \cdot 10^{-4}$ mbar and signals corresponding to m/q=2, 30, 39 and 41 were recorded on-line as a function of time. These signals are presented in figure 6.14.

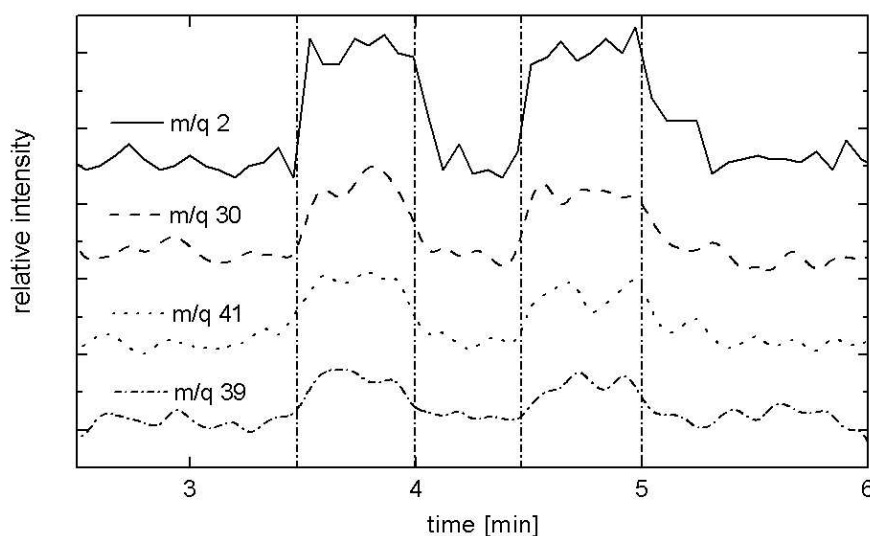Figure 6.14: Variation of intensity of 4 different QMS signals at 773 K with pure methane at $1 \cdot 10^{-4}$ mbar on 0.8Ni/0.2Pd upon opening and closing the excimer lamp shutter.

For the same reasons as pointed out in the previous sections, mass 2 was attributed to hydrogen, mass 30 to C2 hydrocarbons and masses 39 and 41 to C3 hydrocarbons. For our

system, 39 and 41 are specific to propane and propene. At the beginning of the experiment, the shutter of the lamp was closed. It was opened after 3.5 minutes, closed 30 seconds later, reopened at 4.5 minutes and finally closed at 5 minutes. It appears clearly in figure 6.14 that all four signals increase immediately upon irradiation of the catalyst with VUV photons in the presence of methane. The observed behavior corresponds to an enhanced generation of hydrogen, C2 as well as C3 hydrocarbons upon VUV irradiation. This experiment supports the previous suggestion of the existence of a photoassisted activation reaction of methane with a xenon excimer lamp.

6.4   Conclusion

The influence of the irradiation of some selected mono and bimetallic model catalysts with a xenon excimer lamp was investigated with CH_4, 95% CH_4/5% O_2 and 50% CH_4/50% CO_2. In addition, the reactivity and surface composition of the different catalysts tested were evaluated based on AES, XPS and TPR measurements.

The carbon surface uptake during TPR experiments was measured for each model catalyst, with and without VUV irradiation. The amount of carbon formed during the reactions was considered as a catalyst reactivity indicator. In the case of all three gas mixtures applied, the different catalysts exhibit clear different reactivities. The final surface carbon concentration appeared always to be higher in the bright experiments. Moreover, the difference of carbon concentration between bright and dark experiments seemed to increase with the nickel content of the bimetallic catalysts. This suggests a photoassisted methane activation, which is remarkable, as the emission of the xenon excimer lamp is centered at 172 nm, while methane in the gas phase does not absorbs above 140 nm. It was also observed that each pair of bimetallic catalysts characterized by the same average composition exhibit a comparable reactivity, which seemed not to depend on which metal was deposited first on the substrate. A possible reason for this behavior was deduced from AES data which yielded an almost identical surface composition for each pair of bimetallic catalysts with the same average composition. In addition, AES measurements suggested a possible palladium surface enrichment of the metal clusters present on the different catalysts. This phenomenon is in agreement with literature data.

The carbon surface uptake in the case of 50% CH_4/50% CO_2 was very low and confirmed the weak reactivity observed during TPR experiments. The origin of this behavior could not be identified precisely.

In the case of methane and oxygen, contrary to what was observed with pure methane, the concentration of carbon on the surface appeared to be significantly lower in the bright experiments. This could be explained by the formation of ozone or oxygen radicals from the splitting of oxygen molecules by the VUV photons, which can then oxidize the carbon formed on the catalyst surface.

TPR experiments with methane indicated the formation of hydrogen, C2 and some C3 hydrocarbons. The intensities of the QMS signals corresponding to these species were in general higher in the bright experiments. The formation of hydrogen seems to be enhanced over nickel and palladium, while the production of C2 and C3 hydrocarbons is higher over γ-Al_2O_3, nickel and the bimetallic catalysts containing 80% nickel and 20% palladium.

In the case of methane and oxygen, the formation of hydrogen, water, carbon monoxide, carbon dioxide and C2 hydrocarbons was detected. Palladium was the most active catalyst in this case, possibly due to its oxidation resistance. In general, the interpretation of the TPR data was difficult due to a large scatter in the data and require confirmation.

In all bimetallic catalysts, nickel was partly oxidized to what seems to be $Ni(OH)_2$. It was observed that pure nickel was completely oxidized in the bright experiment while it remained unoxidized in the dark experiment. No significant difference of oxidation level could be observed in the bimetallic catalysts between bright and dark experiments. This fact supports the suggestion that the final catalyst structure does not depend on the deposition sequence of nickel and palladium. The addition of palladium seems to form a palladium rich shell over the metal clusters protecting the catalyst against total oxidation. The QMS signals corresponding to hydrogen, C2 and C3 hydrocarbons have been measured on-line while the lamp shutter was successively opened and closed in order to evaluation in a "direct way" the influence of the VUV photons on the reaction. A clear step up of the different signals indicating an enhanced formation of the corresponding products was detected when the lamp shutter was opened, while a step down could be observed when the shutter was closed. This experiment also supports the suggested photoassisted activation of methane.

Chapter 7

Outlook

A great part of the present work concerned the development of several technical systems which are requested to study the activation of methane in a UHV chamber. The design of each device described in this project has been focused on the evolutive aspect in order to allow a wide range of future studies to be performed as convenient and fast as possible. The metal evaporator can for example be equipped very easily with other metals in order to be able to investigate different catalytic systems. Spare lamp envelopes are also ready to be installed on the excimer lamp. In fact, the indium-silver connection developed in this project permits a very convenient change of the envelope. The lamp has to be removed from the UHV system and placed in an oven at about 150 ^{o}C. The envelope can be exchanged in a "plug and play" way. This constitutes an advantage in the case of a breakage or in order to produce other wavelengths than 172 nm. As shown in figure 7.1, two spare xenon lamps have already been filled and sealed, and three others are ready to be installed on the filling station for cleaning, filling and sealing. The unsealed envelopes can for instance be filled with other gases or gas mixtures than xenon, in order to produce different wavelength. The filling station described in section 5.2.2 is already equipped with two different gas inlets, which allows to fabricate in principal most of the excimer lamps listed in table 5.1. This could be achieved in a very limited time period following the procedures described in this thesis. The combination of the wavelengths listed in table 5.1 with the bimetallic evaporator offers the opportunity to investigate a basically unlimited number of photo- and non-photocatalytic systems.

Figure 7.1: Spare lamp envelopes.

Interesting experiments would concern the influence of the photon energy towards the activation of methane. Lamp envelopes producing different wavelength could be tested on a selection of catalysts in order to compare the effectiveness of the different radiations. These experiments could bring some hints to support one of the mechanisms debated in the literature. It would for example be interesting to know if there is threshold energy above which methane is not anymore activated or if the activation effectiveness depends on the photon energy and what is the nature of this dependence.

A possible improvement of the actual system would concern the access to the conversion and selectivity of the investigated reactions and the application of high pressures. This could be achieved by modifying the sample holder and implementing a small excimer lamp in the high pressure reactor.

The installation of an excimer lamp in the HPR would be technically less challenging than the implementation in UHV described in the present work as no cooling would be necessary any more. In fact, as mentioned in section 5.2.4.1, at or above atmospheric pressure, the limited amount of heat produced by a lamp can be evacuated by the convection of the surrounding gas. The HPR contains two funnels which can be pressed against the periphery of the top and bottom of the sample holder housing. This operation separates the inner part of the sample holder containing the catalyst from the rest of the UHV chamber and the sealing is achieved via knife edges on the sample holder which are pressed into copper

gaskets in the top and bottom funnels. The knife edges are shown in figure 7.2. This allows, as described in section 3.1.6, to study reactions at high pressures (10 bars) on model catalysts without exposing the samples to air between the preparation, experiment and surface analysis steps. The gas mixture enters the system by an inlet located in the upper funnel, goes through the sample holder and is finally evacuated by an exhaust located in the bottom funnel below the sample holder which can be directed to a gas analysis unit. In order to be able to determine the conversion and selectivity of a reaction, the sample holder could be implemented with a "gas inlet guide", in order to force the reactant mixture to flow over the catalyst. Such a sample holder has been developed during this work and can be seen in figure 7.2. The construction has however not been possible due to time limitations.

During an experiment, the reactants would be forced to enter in the small slice between

(a)   (b)
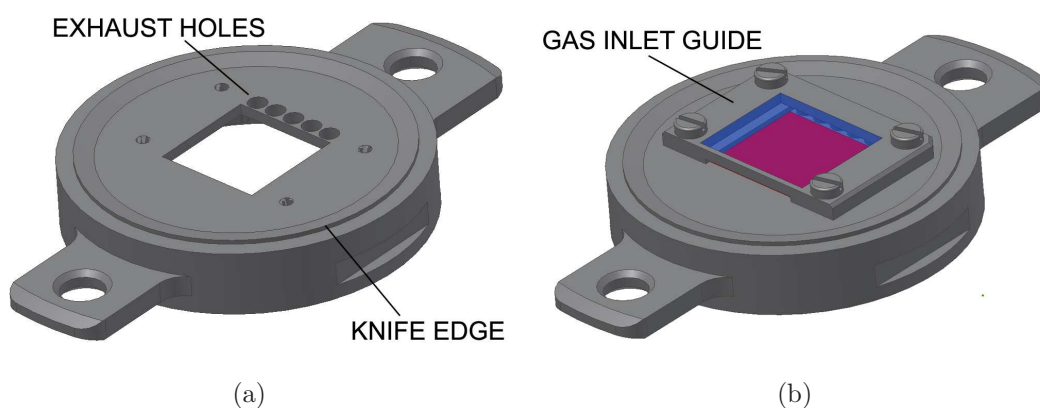
Figure 7.2: (a) Modified sample holder housing (b) Modified sample holder for the determination of the conversion and selectivity.

the catalyst and the inlet guide, to flow over the model catalyst and finally to leave by the exhaust holes through the sample holder. The exhaust gas could then be collected and directed to a GC-MS for analyses. For photocatalytic experiments, the gas inlet guide is fitted with a small suprasil window in order to allow photons to reach the catalyst surface. This process is illustrated in figure 7.3 by a sliced view of the improved sample holder. The realization of this system would open new opportunities of investigation. There are many mono- and bimetallic systems reported in the literature which could potentially be interesting for the photoassisted activation of methane, like for example copper [198], platinum
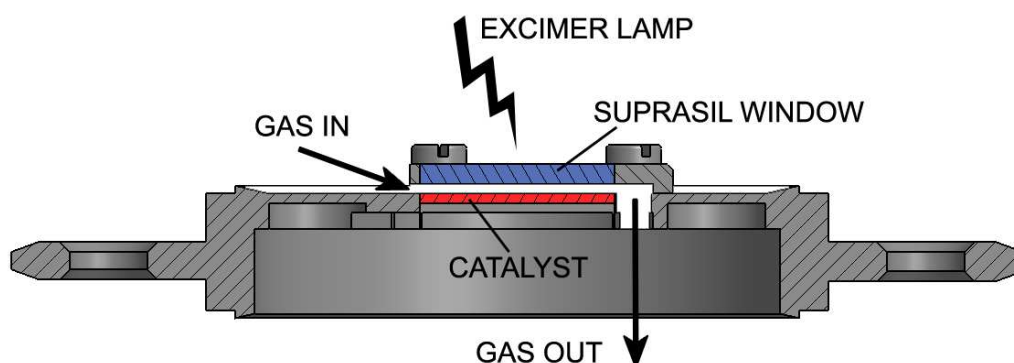
Figure 7.3: Sliced view of a possible improvement of the actual sample holder.

[196] or copper/cobalt catalysts [199]. Other experiments dealing with the photodissociation of water on heterogeneous catalysts would also be highly interesting. As a matter of fact, -OH groups photochemically generated on various photocatalysts (TiO_2, WO_3, NiO) with wavelengths going from the UV up to the visible range, have been reported to react with methane to form methanol [200][201][202]. All the above mentioned experiments have however been carried out with lasers or mercury lamps. Because of its scalability potential and high efficiency, the use of excimer lamps for further investigations would be of high interest.

The setup proposed could also be applied to other fields like the investigation in realistic conditions (10 bars) of the methane activation in gas turbines based on lean premixed combustion. The lamp could be used in order to facilitate the starting procedure of the turbines or to convert a part of the methane into different products which may to improve the flame stability in lean conditions.

The unique combination of an excimer lamp, thin film model catalysts, UHV surface spectroscopic techniques and the possibility to carry out high pressure experiments would provide a highly powerful tool in the field of catalysis research.

A key feature of this setup is to gain access to the conversion and selectivity of reactions on model catalysts. This could be achieved through the modifications of the sample holder and implementation of analytical techniques capable of a high sensitivity and specificity as for instance a GC-MS unit.

Appendix A

Abbreviations

AES	Auger Electron Spectroscopy
ARAES	Angle Resolved Auger Electron Spectroscopy
ARXPS	Angle Resolved X-ray Electron Spectroscopy
DBD	Dielectric Barrier Discharge
DEA	Dissociative Electron Attachment
DFT	Density Functional Theory
EAL	Electron Attenuation Length
FEAL	Fast Entry Air Lock
GTL	Gas To Liquid
GWP	Global Warming Potential
HPR	High Pressure Reactor
IMFP	Inelastic Mean Free Path
IR	Infra Red
LASER	Light Amplification by Stimulated Emission Radiation
LEED	Low Energy Electron Diffraction
NBOH	Non Bridging Oxygen Hole
ODC	Oxygen Deficiency
PC	Preparation Chamber
PDP	Plasma Display Panel
QCM	Quartz Crystal Microbalance

TSP	Titanium Sublimation Pump
UHV	Ultra High Vacuum
UV	Ultraviolet
VUV	Vacuum Ultraviolet
XPS	X-ray Electron Spectroscopy

Curriculum Vitae

LOVIAT Francois

Born on Mai 31, 1979, Delémont, Jura

Swiss citizen

Education

2004–2008: **PhD thesis at the Paul Scherrer Institut, Villigen (PSI)**
Photoassisted activation of methane over supported catalysts with a xenon excimer lamp

2002–2003 **Diploma work at the Serono Biotech Centre, Vevey**
Characterization of axial-flow packed bed bioreactors for the culture of CHO cells

1998–2003: **Swiss Federal Institute of Technology, Lausanne (EPFL)**
Bachelor and Master degree in **Chemical Engineering**

1995–1998: **Gymnase Cantonal (high school), Porrentruy (JU)**

Languages

- **French**, mother tongue

- **English**, fluent

- **German**, fluent

- **Italian**, good knowledge

List of Publications

F. Loviat, I. Czekaj, J. Wambach, and A. Wokaun
Nickel deposition on γ-Al_2O_3 model catalysts: An experimental and theoretical investigation, Surface Science. 603(14):2210-2217, 2009.

F. Loviat, H.M. Rønnow, Ch. Renner, T. Kimura and Y. Tokura
The surface layer of cleaved bilayer manganites, Nanotechnology, 18(4):44020, 2007.

J. Wambach, F. Loviat, I. Czekaj, A. Wokaun
Photoassited activation and reaction of methane over supported catalysts, Surface Science (to be published).

J. Wambach, F. Loviat, I. Czekaj, A. Wokaun
Construction and characterization of a UHV compatible xenon excimer lamp, Journal of Vacuum Science and Technology A (to be published).

I. Czekaj, F. Loviat, J. Wambach, A. Wokaun
Nickel deposition on gamma-Al_2O_3: modelling of metal particles behaviour at the support, Chimia (to be published).

I. Czekaj, F. Loviat, F. Raimondi, J. Wambach, S. Biollaz, A. Wokaun
Characterization of surface processes at the Ni-based catalyst during the methanation of biomass-derived synthesis gas: X-ray photoelectron spectroscopy (XPS) Applied Catalysis A: General, 329:68–78, 2007.

F Meuwly , F Loviat , P-A Ruffieux , A R Bernard , A Kadouri , U von Stockar
Oxygen supply for CHO cells immobilized on a packed-bed of Fibra-Cel(R) disks, Biotechnology & Bioengineering, 93(4):791-801, 2006.

C. N. Borca, S. Canulescu, F. Loviat, D. Grolimund, T. Lippert, A. Wokaun
Analysis of the electronic configuration of the pulsed laser deposited $La_{0.7}Ca_{0.3}MnO_3$ thin films, Applied Surface Science, 254(4):1352-1355, 2007.

Bibliography

[1] P.P. Knops-Gerrits and W.A. Goddard. Methane partial oxidation in iron zeolites: theory versus experiment. *Journal of Molecular Catalysis A*, 166(1):135–145, 2001.

[2] *BP statistical review of world energy.* BBC Horizon, June 2008.

[3] G. A. Olah, A. Goeppert, and G. K. S. Prakash. *Beyond oil and gas: the methanol economy.* Wiley, 2006.

[4] James E. Mielke. *Methane hydrates: Energy prospect or natural hazard ?* CRS report for congress, 2000.

[5] Lara S. Escandon, Salvador Ordonez, Aurelio Vega, and Fernando V. Diez. Oxidation of methane over palladium catalysts: effect of the support. *Chemosphere*, 58(1):9–17, 2005.

[6] D. J. Hofmann. *The NOAA Annual Greenhouse Gas Index (AGGI).* Earth System Research Laboratory, 2008.

[7] Techsum 2001. *Technical summary: Climate Change 2001.* United Nations Environment Programme, 2001.

[8] *The Day The Earth Nearly Died.* BBC Horizon, 5 December 2002.

[9] Bruce Denardo, Leonard Pringle, and Carl DeGrace. When do bubbles cause a floating body to sink? *American Journal of Physics*, 69:1064–1072, 2001.

[10] J. P. Kennett, K. G. Cannariato, I. L. Hendy, and R. J. Behl. *Methane Hydrates in Quaternary Climate Change: The Clathrate Gun Hypothesis.* Washington, DC: American Geophysical Union, 2003.

[11] Steve Connor. The methane time bomb. *The Independent*, 23 September, 2008.

[12] M. A. Delucchi. *A Lifecycle Emissions Model (LEM): Lifecycle Emissions From Transportation Fuels, Motor Vehicles, Transportation Modes, Electricity Use, Heating and Cooking Fuels, and Materials: Appendix E.* Institute of Transportation Studies University of California, Davis, CA 95616, USA, 2003.

[13] S. Dannenberg and R. Conrad. Effect of rice plants on methane production and rhizospheric metabolism in paddy soil. *Biogeochemistry*, 45:53–71, 1999.

[14] Elmar Uherek. Methane / Energie. *ACCENT magazine*, (3), 2005.

[15] J. Lelieveld, S. Lechtenböhmer, and S. S. Assonov. Greenhouse gases: low methane leakage from gas pipelines. *Nature*, 434:841–842, 2005.

[16] *US Environmental Protection Agency Inventory of US Greenhouse Gas Sources and Sinks: 1990-2002.*

[17] A. I. Reshetnikov, N. N. Paramonova, and A. A. Shashkov. An evaluation of historical methane emissions from the soviet gas industry. *Journal of Geophysical Research*, 105(3):3517–3529, 2000.

[18] Jack H. Lunsford. Catalytic conversion of methane to more useful chemicals and fuels: a challenge for the 21st century. *Catalysis Today*, 63(2-4):165–174, 2000.

[19] B. Ellis. *Methane.* Cyprus Environment and Energy, 2008.

[20] T. A. Semelsberger, R. L. Borup, and H. L. Greene. Dimethyl ether (DME) as an alternative fuel. *Journal of Power Sources*, 156(2):497–511, 2006.

[21] M. Müller and U. Hübsch. *"Dimethyl Ether" in Ullmann's Encyclopedia of Industrial Chemistry.* Wiley-VCH, Weinheim, 2005.

[22] International Energy Annual. *Annual Energy Outlook*. USA.gov - Dept. of Energy, 2007.

[23] J. R. Rostrup-Nielsen. Production of synthesis gas. *Catalysis today*, 18:305, 1993.

[24] P.L. Spath and D.C. Dayton. *Preliminary Screening – Technical and Economic Assessment of Synthesis Gas to Fuels and Chemicals with Emphasis on the Potential for Biomass-Derived Syngas.* National Renewable Energy Laboratory, USA, 2003.

[25] R. Larciprete, A. Goldoni, A. Groso, S. Lizzit, and G. Paolucci. The photochemistry of CH_4 adsorbed on Pt(111) studied by high resolution fast XPS. *Surface Science*, 482-485(1):134–140, 2001.

[26] V. Choudhary Tushar, E. Aksoylu, and D. Wayne Goodman. Nonoxidative activation of methane. *Catalysis reviews. Science and engineering*, 45(1):151–203, 2003.

[27] W. J. Stark. *Catalytic Reaction Engineering.* ETH Zurich.

[28] Christophe Gueret, Michel Daroux, and Francis Billaud. Methane pyrolysis: thermodynamics. *Chemical Engineering Science*, 52(5):815–827, 1997.

[29] K. Tabata, Y. Teng, T. Takemoto, E. Suzuki, M. A. Bantildeares, M. A. Pentildea, and J. L. G. Fierro. Activation of methane by oxygen and nitrogen oxides. *Catalysis Reviews*, 44(1):58, 2002.

[30] A. W. Sexton, E. Mac Giolla Coda, and B. K. Hodnett. A comparison of the performances of selected catalysts for the partial oxidation of methane to formaldehyde at elevated pressures. *Catalysis Today*, 46(2-3):127–136, 1998.

[31] Sergei Pak, Ping Qiu, and Jack H. Lunsford. Elementary reactions in the oxidative coupling of methane over $Mn/Na_2WO_4/SiO_2$ and $Mn/Na_2WO_4/MgO$ catalysts. *Journal of Catalysis*, 179(1):222–230, 1998.

[32] D. Schweer, L. Meeczko, and M. Baerns. OCM in a fixed-bed reactor: limits and perspectives. *Catalysis Today*, 21(2-3):357–369, 1994.

[33] A. C. Rosenzwieg, C. A. Frederick, S. J. Lippard, and P. R. Nordlund. Crystal structure of bacterial non-haem iron hydroxylase that catalyses the biological oxidation of methane. *Nature*, 366:537–543, 1993.

[34] N. Osterwalder and W. J. Stark. Direct coupling of bromine-mediated methane activation and carbon-deposit gasification. *ChemPhysChem*, 8(2):297–303, 2007.

[35] A. K. Richards. *Anhydrous processing of methane into methane-sulfonic acid, methanol, and other compounds.* United States Patent 7282603, 2005.

[36] B. R. Wood, J. A. Reimer, A. T. Bell, M. T. Janicke, and K. C. Ott. Methanol formation on Fe/Al-MFI via the oxidation of methane by nitrous oxide. *Journal of Catalysis*, 225(2):300–306, 2004.

[37] Y. A. Gruzdkov, K. Watanabe, K. Sawabe, and Y. Matsumoto. Photochemical C-H bond activation of methane on a Pt(111) surface. *Chemical Physics Letters*, 227(3):243–247, 1994.

[38] David Briggs and John T. Grant. *Surface analysis by Auger and X-ray photoelectron spectroscopy.* IM Publications and Surface Spectra Limited, 2003.

[39] D. Briggs and M. P. Seah. *Practical Surface Analysis.* Wiley-Second Edition, 1990.

[40] J.F. Watts and J. Wolstenholme. *An Introduction to Surface Analysis by* XPS *and* AES. Wiley, 2003.

[41] A. Zangwill. *Physics at Surfaces.* Cambridge University Press, 1988.

[42] M.P. Seah and W.A. Dench. Quantitative electron spectroscopy of surfaces: A standard data base for electron inelastic mean free paths in solids. *Surface and Interface Analysis*, 1:2–11, 1979.

[43] T.S. Lassen, S. Tougaard, and A. Jablonski. Practical correction procedures for elastic electron scattering effects in ARXPS. *Surface science*, 481:150–162, 2001.

[44] P.J. Cumpson and M.P. Seah. Elastic scattering corrections in AES and XPS. II. Estimating attenuation lengths and conditions required for their valid use in over-layer/substrate experiments. *Surface and Interface Analysis*, 25:430, 1997.

[45] J.H. Scofield. Hartree-Slater subshell photoionization cross-sections at 1254 and 1487 eV. *Journal of Electron Spectroscopy and Related Phenomena*, 8:129–137, 1976.

[46] C. D. Wagner, L. E. Davies, M. V. Zeller, J. A. Taylor, R. M. Richmond, and L. H. Gale. Empirical atomic sensitivity factors for chemical analysis by electron spectroscopy for chemical analysis. *Surface and Interface Analysis*, 3:211, 1981.

[47] Frank A. Settle. *Handbook of Instrumental Techniques for Analytical Chemistry*. Prentice Hall, 1997.

[48] Roland Benoit. *Spectroscopie d'électrons - XPS*. SFV, 2003.

[49] L. Meitner. Das beta-Strahlenspektrum von UX1 und seine Deutung. *Zeitschrift für Physik*, 17:54–66, 1923.

[50] P. Auger. Effet photoélectrique composé. *J. Physique Radium*, 6:205, 1925.

[51] D. Briggs and M.P. Seah. *Practical Surface analysis:Auger and x-ray photoelectron spectroscopy*. Wiley, 1990.

[52] T. Sekin, Y. Nagadawa, M. Kudoh, Y. Sakai, A. S. Parkes, J. D. Geller, A. Mogami, and K. Hirata. *Handbook of Auger Electron Sectroscopy*. JEOL, 1982.

[53] Lawrence E. Davis. *Handbook of Auger electron spectroscopy*. Physical Electronics Industries, 1976.

[54] P. Drude. *Annual Review of Physical Chemistry*, 36:532, 1889.

[55] D. E. Aspnes. Interface ellipsometry: An overview. *Surface Science*, 101(1-3):84–98, 1980.

[56] Max Born and Emil Wolf. *Principles of optics: electromagnetic theory of propagation, interference and diffraction of light*. 7th expanded ed. - Cambridge, 1999.

[57] Hiroyuki Fujiwara. *Spectroscopic ellipsometry : principles and applications*. Chichester : Wiley, 2007.

[58] D. E. Aspnes. Optical properties of thin films. *Thin Solid Films*, 89(3):249–262, 1982.

[59] N. John DiNardo. *Nanoscale characterization of surfaces and interfaces*. Weinheim : Wiley-VCH, 1994.

[60] J.W. Niemantsverdriet. *Spectroscopy in catalysis : an introduction*. 3rd, compl. rev. and enlarged ed. - Weinheim : Wiley-VCH, 2007.

[61] J. Curie and P. Curie. Developpment par compession de l'electricite polaire dans les cristaux hemiedres a faces inclinees. *Bulletin de la Societe Mineralogie de France*, 3:90, 1880.

[62] GZ. Sauerbrey. Verwendung von Schwingquarzen zur Wägung dünner Schichten und zur Mikrowägung. *Zeitschrift für Physik*, 155:206–222, 1959.

[63] J Villalobos, R Glosser, and H Edelson. A quartz crystal-controlled evaporator for the study of metal film alloy hydrides. *Measurement Science and Technology*, 1(4):365–370, 1990.

[64] W.H. King Jr. Piezoelectric sorption detector. *Analytical Chemistry*, 36(9):1735–1739, 1964.

[65] S. Küper, J. Brannon, and K. Brannon. Threshold behavior in polyimide photoablation: Single-shot rate measurements and surface-temperature modeling. *Applied Physics A*, 56:43–50, 1993.

[66] T. Dumont. Laser interaction with materials: From transparent materials to thin films. *Swiss Federal Institut of Technology: Zurich*, DISS. ETH NO. 16620, 2006.

[67] Ron F. Schmitt, John W. Allen, John F. Vetelino, Jesse Parks, and Chao Zhang. Bulk acoustic wave modes in quartz for sensing measurand-induced mechanical and electrical property changes. *Sensors and Actuators B*, 76(1-3):95–102, 2001.

[68] C. Lu and A.W. Czanderna. Applications of piezolelctric quartz crystal microbalances. *Methods and phenomena; their applications in science and technology*, 7, 1984, Amsterdam: Elsevier.

[69] J.J. Thomson. Cathode rays. *Philosophical Magazine*, 44:295, 1897.

[70] J.J. Thomson. *Rays of positive electricity and the application to chemical analyses.* Longmans, Green & Co, London, 1913.

[71] F.W. Aston. A second-order focusing mass spectrograph and isotopic weights by the doublet method. *Proceedings of the Royal Society of London. Series A*, 163:391–404, 1937.

[72] Stone D.-H. Shi, Christopher L. Hendrickson, and Alan G. Marshall. Counting individual sulfur atoms in a protein by ultrahighresolution Fourier transform ion cyclotron resonance mass spectrometry: Experimental resolution of isotopic fine structure in proteins. *Proceedings of the National Academy of Sciences of the United States of America*, 95(20):11532–11537, 1998.

[73] S.A. Trauger, E.P. Go, Z. Shen, J.V. Apon, B.J. Compton, E.S.P. Bouvier, M.G. Finn, and G. Siuzdak. High sensitivity and analyte capture with desorption/ionization mass spectrometry on silylated porous silicon. *Analytical Chemistry*, 76(15):4484–4489, 2004.

[74] Chhabil Dass. *Fundamentals of contemporary mass spectrometry.* Wiley, 2007.

[75] R.G. Cooks and A.L. Rockwood. The 'Thomson'. a suggested unit for mass spectroscopists. *Rapid Communications in Mass Spectrometry*, 5:93, 1991.

[76] Irma Lavagnini, Franco Magno, Roberta Seraglia, and Pietro Traldi. *Quantitative applications of mass spectrometry.* Wiley, 2006.

[77] Edmond de Hoffmann and Vincent Stroomant. *Mass spectrometry: principles and applications.* Wiley, 2007.

[78] M. E. Gross, G. J. Fisanick, P. K. Gallagher, K. J. Schnoes, and M. D. Fennell. Laser-initiated deposition reactions: Microchemistry in organogold polymer films. *Applied Physics Letters*, 47(9):923–925, 1985.

[79] F. Raimondi. Structural modifications of Cu/ZnO-based commercial and model catalysts during methanol reforming. *Swiss Federal Institut of Technology: Zurich*, DISS. ETH NO. 14963, 2003.

[80] Malgosia M. Pakulska, Catherine M. Grgicak, and Javier B. Giorgi. The effect of metal and support particle size on NiO/CeO₂ and NiO/ZrO₂ catalyst activity in complete methane oxidation. *Applied Catalysis A: General*, 332(1):124–129, 2007.

[81] Michel Chea and Carroll O. Bennett. The influence of particle size on the catalytic properties of supported metals. *Advances in Catalysis*, 36(1989):55–172, 1989.

[82] Yanjun Zhao, Arthur Mpela, Dan I. Enache, Stuart H. Taylor, Diane Hildebrandt, David Glasser, Graham J. Hutchings, Martin P. Atkins, and Michael S. Scurrell. Study of carbon monoxide hydrogenation over supported Au catalysts. *Studies in Surface Science and Catalysis*, 163:141–151, 2007.

[83] A. M. Doyle, Sh. K. Shaikhutdinov, and H. J. Freund. Alkene chemistry on the palladium surface: nanoparticles vs single crystals. *Journal of Catalysis*, 223(2):2004, 444-453.

[84] V. Ponec and G.C. Bond. *Catalysis by Metals and Alloys*. Elsevier, Amsterdam, 1995.

[85] X. Xu and D. W. Goodman. *Handbook of Surface Imaging and Visualization*. CRC Press, Boca Raton, FL, 1995.

[86] Helmut Poppa. Model studies in catalysis with UHV-deposited metal particles and clusters. *Vacuum*, 34(12):1081–1095, 1984.

[87] Darrell R. Rainer, Chen Xu, and D. Wayne Goodman. Characterization and catalysis studies of small metal particles on planar model oxide supports. *Journal of Molecular*

Catalysis A, 119(1-3):307–325, International Conference on Theoretical Aspects of Heterogeneous Catalysis, 23 May 1997.

[88] H Poppa, D Fargues, L Kieken, D Neiman, and R Savoy. The sticking coefficient of Pd on planar alumina supports. *Vacuum*, 41(1-3):485–488, Surface Science Section, 1990.

[89] D.W. Goodman, D.A. King, and D.P. Woodruff (Eds.). Growth and properties of ultrathin epitaxial layers. *The Chemical Physics of Solid Surfaces and Heterogeneous Catalysis*, 8:375, 1997.

[90] Marcus Baumer and Hans-Joachim Freund. Metal deposits on well-ordered oxide films. *Progress in Surface Science*, 61(7-8):127–198, 1999.

[91] H.J. Freund. Oxide surfaces. *Faraday Discussion*, 114:1–31, 1999.

[92] G. Buelna and Y. S. Lin. Sol-gel-derived mesoporous γ-alumina granules. *Microporous and Mesoporous Materials*, 30(2-3):359–369, 1999.

[93] G. Groen, J. Ferment, M.J. Groeneveld, J. Decleer, and A. Delva. Scaling down of the calcination process for industrial catalyst manufacturing. *Advances in Pharmacology, Academic Press*, 63:185–203, 1991.

[94] Pablo C. L'Argentiere, Maria M. Canon, Nora S. Figoli, and Julio Ferron. AES and XPS studies of the influence of Ni addition on Pd/Al_2O_3 catalytic activity and sulfur resistance. *Applied Surface Science*, 68(1):41–47, 1993.

[95] M. Sittig. *Handbook of Catalyst Manufacture*. Noyer Data Corporation, 1978.

[96] R. F. Peterson. *Hydrogenation Catalysts*. Noyes Data Corporation, 1977.

[97] A. Christensen, A. V. Ruban, P. Stoltze, K. W. Jacobsen, H. L. Skriver, J. K. Nørskov, and F. Besenbacher. Phase diagrams for surface alloys. *Physical Review B*, 56(10):5822–5834, Sep 1997.

[98] A. V. Ruban, H. L. Skriver, and J. K. Nørskov. Surface segregation energies in transition-metal alloys. *Physical Review B*, 59(24):15990–16000, Jun 1999.

[99] C. Merckling, M. El-Kazzi, V. Favre-Nicolin, M. Gendry, Y. Robach, G. Grenet, and G. Hollinger. Epitaxial growth and relaxation of $\gamma - Al_2O_3$ on silicon. *Thin Solid Films*, 515:6479–6483, 2007.

[100] K. Reszka, J. Rakoczy, Z. Z. urek, A. Czyzyniewski, A. Gilewicz, and M. Homa. Catalytic properties of Al_2O_3 deposited by ion sputtering using DC and RF sources. *Vacuum*, 78:149–155, 2005.

[101] A. Bender and E. Schippel. X-ray reflectivity study of reactice DC sputter deposited Al_2O_3 thin films. *Active and Passive Electronic Components*, 16:35–40, 1993.

[102] M.D. Groner, J.W. Elam, F.H. Fabreguette, and S.M. George. Electrical characterization of thin Al_2O_3 films grown by atomic layer deposition on silicon and various metal substrates. *Thin Solid Films*, 413:186–197, 2002.

[103] S. Neralla, D. Kumar, S. Yarmolenko, and J. Sankar. Mechanical properties of nanocomposite metal-ceramic thin films. *Composites Part B: Engineering*, 35(2):157–162, 2004.

[104] C. Krug, E. B. O. da Rosa, R. M. C. de Almeida, J. Morais, I. J. R. Baumvol, T. D. M. Salgado, and F. C. Stedile. Atomic transport and chemical stability during annealing of ultrathin Al_2O_3 films on Si. *Physical Review Letters*, 85(19), 2000.

[105] X. Multone and P. Hoffmann Y. Luo. Er-doped Al_2O_3 thin films deposited by high-vacuum chemical vapor deposition (HV-CVD). *Materials Science and Engineering*, 146(1-3), 2007.

[106] W.J. DeSisto, Y-T. Qian, C. Hannigan, J.O. Edwards, R. Kershaw, K. Dwight, and A. Wold. Preparation and characterization of alumina films prepared by a novel spray pyrolysis method. *Materials Research Bulletin*, 25(2):183–189, 1990.

[107] M. Sridharan, M. Sillassen, J. Bottiger, J. Chevallier, and H. Birkedal. Pulsed DC magnetron sputtered Al_2O_3 films and their hardness. *Surface and Coatings Technology*, 202:920–924, 2007.

[108] R. Cremer, M. Witthaut, D. Neuschütz, G. Erkens, T. Leyendecker, and M. Feldhege. Comparative characterization of alumina coatings deposited by RF, DC and pulsed reactive magnetron sputtering. *Surface and Coatings Technology*, 120-121:213–218, 1999.

[109] Brian Chapman. *Glow Discharge Processes: Sputtering and Plasma Etching*. Wiley, 1980.

[110] John F. Moulder, William F. Stickle, and Peter E. Sobol. *Handbook of X-Ray Photoelectron Spectroscopy*. Perkin-Elmer, Physical Electronics Division, 1992.

[111] Q.-Y. Tong, Q. Gan, G. Fountain, P. Enquist, R. Scholz, and U. Gösele. Fluorine-enhanced low-temperature wafer bonding of native-oxide covered. *Applied Physics Letters*, 85(17), 2004.

[112] D. E. Aspnes and J. B. Theeten. Optical properties of the interface between Si and its thermally grown oxide. *Physical Review Letters*, 43(14):1046–1050, 1979.

[113] D. Gopireddy and C. G. Takoudis. Diffusion-reaction modeling of silicon oxide interlayer growth during thermal annealing of high dielectric constant materials on silicon. *Physical Review B*, 77:205304, 2008.

[114] Pasquarello A., Hybertsen M. S., and Car R. Interface structure between silicon and its oxide by first-principles molecular dynamics. *Nature*, 396:58, 1998.

[115] R. E. Walkup and S. I. Raider. In situ measurements of SiO(g) production during dry oxidation of crystalline silicon. *Applied Physics Letters*, 53(10):888–890, 1988.

[116] C. Krug, E. B. O. da Rosa, R. M. C. de Almeida, J. Morais, I. J. R. Baumvol, T. D. M. Salgado, and F. C. Stedile. Atomic transport and chemical stability during annealing of ultrathin Al_2O_3 films on Si. *Physical Review Letters*, 85(19):4120–4123, 2000.

[117] C. S. Shern, J. S. Tsay, and Tsu yi Fu. Growth mechanism of Ni on Pt(110) at low temperature. *Applied Surface Science*, 92:74–78, 1996.

[118] R. E. Tanner, I. Goldfarb, M. R. Castell, and G. A. D. Briggs. The evolution of Ni nanoislands on the rutile TiO$_2$(110) surface with coverage, heating and oxygen treatment. *Surface Science*, 486(3):167–184, 2001.

[119] D. J. Eaglesham and M. Cerullo. Dislocation-free stranski-krastanow growth of Ge on Si(100). *Physical Review Letters*, 64(16):1943–1946, 1990.

[120] J.P. Jacobs, L.P. Lindfors, J.G.H. Reintjes, O. Jylhä, and H.H. Brongersma. The growth mechanism of nickel in the preparation of Ni/Al$_2$O$_3$ catalysts studied by LEIS, XPS and catalytic activity. *Catalysis Letters*, 25:1994, 315.

[121] Eckhard Bauer. Epitaxy of metals on metals. *Applications of surface science*, 11/12:479–494, 1982.

[122] C. Argile and G.E. Rhead. Adsorbed layer and thin film growth modes monitored by Auger electron spectroscopy. *Surface Science Reports*, page 279–356, 1989.

[123] T. Campbell. Ultrathin metal films and particles on oxide surfaces: structural, electronic and chemisorptive properties. *Surface Science Reports*, 27(1-3):1–111, 1997.

[124] S. H. Overbury, P. A. Bertrand, and G. A. Somorjai. Surface composition of binary systems. Prediction of surface phase diagrams of solid solutions. *Chemical Reviews*, 75(5):547 – 560, 1975.

[125] C. J. Powell and A. Jablonski. *NIST Electron Effective Attenuation Length Database*. U.S. Department of Commerce, 2001.

[126] F.Loviat, I. Czekaj, J.Wambach, and A. Wokaun. Nickel deposition on $\gamma - Al_2O_3$ model catalysts: An experimental and theoretical investigation. *Submitted to Applied Catalysis A: General*, 2009.

[127] Marcus Baumer and Hans-Joachim Freund. Metal deposits on well-ordered oxide films. *Progress in Surface Science*, 61(7-8):127–198, 1999.

[128] E. Gillet, M. H. El Yakhloufi, J. P. Disalvo, and F. Ben Abdelouahab. In situ characterization of ultra-thin palladium deposits on α- and γ-alumina. *Surface Science*, 419(2-3):216–225, 1999.

[129] P. Atanasova, J. Wise, M. Fallbach, T. Kodas, and M. Hampden-Smith. Chemical vapor deposition of palladium on silica and alumina supports. *Preparation of catalysis VII*, page 73–82, 1998.

[130] M. Baumer, M. Frank, M. Heemeier, R. Kuhnemuth, S. Stempel, and H. J. Freund. Nucleation and growth of transition metals on a thin alumina film. *Surface Science*, 454-456:957–962, 2000.

[131] J.W. Elam, A. Zinovev, C.Y. Han, H.H. Wang, U. Welp, J.N. Hryn, and M.J. Pellin. Atomic layer deposition of palladium films on Al_2O_3 surfaces. *Thin Solid Films Volume*, 515(4):1664–1673, 2006.

[132] V. Moroz, Y. Lykhach, and M. Yoshitake. RHEED study of Pd film growth on $Al_2O_3(111)$/NiAl(110). *Thin Solid Films*, 464-465:136–140, 2004.

[133] A. Bogicevic and D.R. Jennison. Variations in the nature of metal adsorption on ultrathin Al_2O_3 films. *Physical review letters*, 82(20):4050–4053, 1999.

[134] P. Legare and B. R. Bilwes. Electronic structure of palladium deposits on alumina. *Surface Science*, 279(1-2):159–164, 1992.

[135] Zdenek Bastl. X-ray photoelectron spectroscopy of supported metal particles. *Vacuum*, 36(7-9):447–448, 1986.

[136] V. Nehasil, S. Zafeiratos, V. Matolin, and S. Ladas. XPS study of Pd particle growth on different alumina surfaces. *Vacuum*, 50(1-2):143–145, 1998.

[137] Thomas Oppenlander, Carsten Walddorfer, Jens Burgbacher, Martin Kiermeier, Klaus Lachner, and Helga Weinschrott. Improved vacuum-UV VUV-initiated photomineralization of organic compounds in water with a xenon excimer flow-through photoreactor (Xe_2 lamp, 172 nm) containing an axially centered ceramic oxygenator. *Chemosphere*, 60(3):302–309, 2005.

[138] Edward A. Sosnin, Thomas Oppenlander, and Victor F. Tarasenko. Applications of capacitive and barrier discharge excilamps in photoscience. *Journal of Photochemistry and Photobiology C: Photochemistry Reviews*, 7(4):145–163, 2006.

[139] G. J. Fisanick, M. E. Gross, J. B. Hopkins, M. D. Fennell, K. J. Schnoes, and A. Katzir. Laser-initiated microchemistry in thin films: Development of new types of periodic structure. *Journal of Applied Physics*, 57(4):1139–1142, 1985.

[140] M. E. Gross, A. Appelbaum, and P. K. Gallagher. Laser direct-write metallization in thin palladium acetate films. *Journal of Applied Physics*, 61(4):1628–1632, 1987.

[141] Jun-Ying Zhang, Hilmar Esrom, and Ian W. Boyd. Decomposition mechanisms of thin palladium acetate film with excimer UV radiation. *Applied Surface Science*, 96-98:399–404, 1996.

[142] Philippe Bergonzo and Ian W. Boyd. Rapid photochemical deposition of silicon dioxide films using an excimer lamp. *Journal of Applied Physics*, 76(7):4372–4376, 1994.

[143] R.S. Nohr and J.G. Macdonald. Incoherent excimer UV radiation and matched photochemistry as a new tool for resin curing. *Radiation Physics and Chemistry*, 46(4-6, Part 2):983–986, 1995.

[144] J. Zhang, H. Esrom, U. Kogelschatz, and G. Emig. Modification of polymers with UV excimer radiation from lasers and lamps. *Journal of Adhesion Science and Technology*, 8(32):1179–1210, 1994.

[145] Jun Ying Zhang, Hilmar Esrom, Ulrich Kogelschatz, and Gerhard Emig. Large area photochemical dry etching of polyimide with excimer UV lamps. *Applied Surface Science*, 69(1-4):299–304, 1993.

[146] Ian W. Boyd and J. Y. Zhang. New large area ultraviolet lamp sources and their applications. *Nuclear Instruments and Methods in Physics Research Section B: Beam Interactions with Materials and Atoms*, 121(1-4):349–356, 1997.

[147] U. Kogelschatz. Silent discharges for the generation of ultraviolet and vacuum ultraviolet excimer radiation. *Pure and Applied Chemistry*, 62(9):1667–1674, 1990.

[148] O. Dutuit, R. A. Gutcheck, and J. Le Calve. Spectral and kinetic studies of the second continuum fluorescence of xenon excited by synchrotron radiation. *Chemical Physics Letters*, 58(1):66–72, 1978.

[149] B. Gellert and U. Kogelschatz. Generation of excimer emission in dielectric barrier discharges. *Applied Physics B: Lasers and Optics*, 52(1):14–21, 1991.

[150] Hilmar Esrom and Ulrich Kogelschatz. Modification of surfaces with new excimer UV sources. *Thin Solid Films*, 218(1-2):231–246, 1992.

[151] P. G. Wilkinson and E. T. Byram. Rare gas light sources for the vacuum ultraviolet. *Applied Optics*, 4(5):581–588, 1965.

[152] A. R. Calloway, T. A. Galantowicz, and W. R. Fenner. Vacuum ultraviolet driven chemical vapor deposition of localized aluminum thin films. *The Journal of Vacuum Science and Technology A*, 1:534, 1983.

[153] H. A. Koehler, L. J. Ferderber, D. L. Redhead, and P. J. Ebert. Vacuum-ultraviolet emission from high-pressure xenon and argon excited by high-current relativistic electron beams. *Physical Review A*, 9(2):768–781, Feb 1974.

[154] P. Millet, A. Birot, H. Brunet, J. Galy, B. Pons-Germain, and J. L. Teyssier. Time resolved study of the UV and near UV continuums of xenon. *The Journal of Chemical Physics*, 69(1):92–97, 1978.

[155] Ori Cheshnovsky, Baruch Raz, and Joshua Jortner. Temperature dependence of rare gas molecular emission in the vacuum ultraviolet. *Chemical Physics Letters*, 15(4):475–479, 1972.

[156] T. E. Stewart, G. S. Hurst, T. E. Bortner, J. E. Parks, F. W. Martin, and H. L. Weidner. Proton excitation of continuous emission in the noble gases. *Journal of the Optical Society of America*, 60(10):1290, 1970.

[157] W. Siemens. Ueber die elektrostatische Induction und die Verzögerung des Stroms in Flaschendräten. *Annual Review of Physical Chemistry*, 102(1-4):66, 1857.

[158] Thomas Andrews and Peter G. Tait. On the volumetric relations of ozone, and the action of the electrical discharge on oxygen and other gases. *Philosophical Transactions of the Royal Society of London*, 150:113–131, 1860.

[159] U. Kogelschatz, B. Eliasson, and W. Egli. From ozone generators to flat television screens: history and future potential of dielectric-barrier discharges. *Pure and Applied Chemistry*, 71(10):1819–1828, 1999.

[160] H. Becker. *Wissenschaftliche Veröffentlichungen aus dem Siemens Konzern*, 1:76, 1920.

[161] Y. Tanaka. Continuous emission spectra of rare gases in the vacuum ultraviolet region. *Journal of the Optical Society of America*, 45:710–713, 1955.

[162] B. Eliasson and U. Kogelschatz. UV excimer radiation from dielectric-barrier discharges. *Applied Physics B: Lasers and Optics*, 46(4):299–303, 1988.

[163] David E. Mentley. Flat panel display market. *Stanford Resources/iSuppli*, 2001.

[164] Emily Chuang. PDP module production up nearly 21% in 2007, but sales down 14%, says displaybank. *DIGITIMES*, Thursday 14 February 2008.

[165] U. Kogelschatz, B. Eliasson, and H. Esrom. Industrial applications of excimer ultraviolet sources. *Materials & DesignVolume*, 12(5):251–258, 1991.

[166] K. S. Gochelashvili, A. V. Dem'yanov, I. V. Kochetov, and L. R. Yangurazova. Theory of excimer lamps pumped by pulsed self-sustained discharges. *Laser Physics*, 3(1):140–145, 1993.

[167] V. V. Ivanov, K. S. Klopovski, Yu A. Mankelevich, A. T. Rakhimov, T. V. Rakhimovy, G. B. Rulev, and V. B. Saenko. Experimental and theoretical study of the efficiency of an excimer lamp pumped by a pulse distributed discharge in xenon. *Laser Physics*, 6(4):654–659, 1996.

[168] U. Kogelschatz, H. Esrom, J. Y. Zhang, and I. W. Boyd. High-intensity sources of incoherent UV and VUV excimer radiation for low-temperature materials processing. *Applied Surface Science*, 168(1-4):29–36, 2000.

[169] Ulrich Kogelschatz. Silent-discharge driven excimer UV sources and their applications. *Applied Surface Science*, 54:410–423, 1992.

[170] A Schreiber, B Kühn, E Arnold, F-J Schilling, and H-D Witzke. Radiation resistance of quartz glass for VUV discharge lamps. *Journal of Physics D: Applied Physics*, 38(17):3242–3250, 2005.

[171] J.B. Nee, J.C. Yang, P.C. Lee, X.Y. Wang, and C.T. Kuo. Detection of O^{1}S) produced in the photodissociation of N_2O. *Journal of Physics B: Atomic, Molecular and Optical Physics*, 31(23):5175–5181, 1998.

[172] N. Leclerc, C. Pfleiderer, H. Hitzler, J. Wolfrum, K. O. Greulich, S. Thomas, and W. Englisch. Luminescence and transient absorption bands in fused SiO_2 induced by KrF laser radiation at various temperatures. *Journal of Non-Crystalline Solids*, 149(1-2):115–121, 1992.

[173] Nobu Kuzuu and Masataka Murahara. Excimer-laser-induced emission bands in fused quartz. *Physical Review B*, 47(6):3083–3088, 1993.

[174] Erich Arnold. Lamps for technical applications. *Heraeus Noblelight GmbH*, 1991.

[175] K. Arai, H. Imai, H. Hosono, Y. Abe, and H. Imagawa. Two-photon processes in defect formation by excimer lasers in synthetic silica glass. *Applied Physics Letters*, 53(20):1891, 1988.

[176] Jun-Ying Zhang and Ian W. Boyd. Lifetime investigation of excimer UV sources. *Applied Surface Science*, 168(1-4):296–299, 2000.

[177] G. Heit, A. Neuner, P.-Y. Saugy, and A.M. Braun. Vacuum-UV (172 nm) actinometry. the quantum yield of the photolysis of water. *Journal of Physical Chemistry A*, 102(28):5551–5561, 1998.

[178] D. Pagnon, J. Amorim, J. Nahorny, M. Touzeau, and M. Vialle. On the use of actinometry to measure the dissociation in 0_2 DC glow discharges: determination of the wall recombination probability. *Journal of Physics D: Applied Physics*, 28:1856–1968, 1995.

[179] R. D. Beck, P. Maroni, D. C. Papageorgopoulos, T. T. Dang, M. P. Schmid, and T. R. Rizzo. Vibrational mode-specific reaction of methane on a nickel surface. *Science*, 302(5642):98 – 100, 2003.

[180] Mathieu P. Schmid, Plinio Maroni, Rainer D. Beck, and Thomas R. Rizzo. Surface reactivity of highly vibrationally excited molecules prepared by pulsed laser excitation: CH$_4$ (2 nu$_3$) on Ni(100). *The Journal of Chemical Physics*, 117(19):8603–8606, 2002.

[181] J. Yoshinobu, H. Ogasawara, and M. Kawai. Symmetry controlled surface photochemistry of methane on Pt(111). *Physical Review Letters*, 75(11):2176–2179, 1995.

[182] K. Watanabe and Y. Matsumoto. Photochemistry of methane on Cu(111). *Surface Science*, 454-456:262–266, 2000.

[183] K. Watanabe and Y. Matsumoto. Comparative study of photochemistry of methane on Pt(111) and Pd(111) surfaces. *Surface Science*, 390(1-3):250–255, 1997.

[184] K. Watanabe, K. Sawabe, and Y. Matsumoto. Adsorbate-localized excitation in surface photochemistry: Methane on Pt(111). *Physical Review Letters*, 76(10):1751–1754, 1996.

[185] Xihui Chen and Shuben Li. Photooxidation of methane to methanol by molecular oxygen on water-preadsorbed porous TiO$_2$-based catalysts. *Chemistry Letters*, 29(4):314, 2000.

[186] P. C. L'Argentiere, M. M. Canon, N. S. Figoli, and J. Ferron. AES and XPS studies of the influence of Ni addition on Pd/Al$_2$O$_3$ catalytic activity and sulfur resistance. *Applied Surface Science*, 68(1):41–47, 1993.

[187] John H. Sinfelt. *Bimetallic catalysts : discoveries, concepts, and applications*. Wiley, 1983.

[188] C. H. Bartholomew and R. J. Farrauto. *Fundamentals of industrial catalytic processes, 2nd ed.* Wiley-Interscience, 2006.

[189] V. R. Stamenkovic, B. Fowler, Bongjin S. Mun, G. Wang, P. N. Ross, C. A. Lucas, and N. M. Markovic'. Improved oxygen reduction activity on $Pt_3Ni(111)$ via increased surface site availability. *Science*, 315:493 – 497, 2007.

[190] J. G. Chen, C. A. Menning, and M. B. Zellner. Monolayer bimetallic surfaces: Experimental and theoretical studies of trends in electronic and chemical properties. *Surface Science Reports*, 63(5):201–254, 2008.

[191] A. Christensen, A. V. Ruban, P. Stoltze, K. W. Jacobsen, H. L. Skriver, J. K. Nørskov, and F. Besenbacher. Phase diagrams for surface alloys. *Physical review. B*, 56(10):5822–5834, 1997.

[192] A. Ruban, B. Hammer, P. Stoltze, H. L. Skriver, and J. K. Nørskov. Surface electronic structure and reactivity of transition and noble metals. *Journal of Molecular Catalysis A: Chemical*, 115(3):421–429, 1997.

[193] A. V. Ruban, H. L. Skriver, and J. K. Nørskov. Surface segregation energies in transition-metal alloys. *Physical review B*, 59(24):15990–16000, 1999.

[194] D. A. Skoog, D. M. West, and F. J. Holler. *Chimie Analytique*. DeBoeck université, 1997.

[195] J.W. Au, G. Cooper, G.R. Burton, T.N. Olney, and C.E. Brion. The valence shell photoabsorption of the linear alkanes. *Chemical Physics*, 173:209–239, 1993.

[196] Y. Matsumoto, Y. A. Gruzdkov, K. Watanabe, and K. Sawabe. Laser-induced photochemistry of methane on Pt(111): Excitation mechanism and dissociation dynamics. *The Journal of chemical physics*, 105(11):4775–4788, 1996.

[197] P.A.P. Nascente, M.F. Carazzolle, A. de Siervo, S.S. Maluf, R. Landers, and G.G. Kleiman. Crystallographic structure of ultra-thin films of Pd on Ni(111) and Ni on Pd(111) studied by photoelectron diffraction. *Journal of Molecular Catalysis A: Chemical*, 281(1-2):3–8, 2008.

[198] K. Watanabe and Y. Matsumoto. Photochemistry of methane on Cu(111). *Surface Science*, 454-456:262–266, 2000.

[199] J. H. Larsen and I. Chorkendorff. Increased dissociation probability of CH$_4$ on Co/Cu(111). *Surface Science*, 405(1):62–73, 1998.

[200] C. E. Taylor and R. P. Noceti. New developments in the photocatalytic conversion of methane to methanol. *Catalysis Today*, 55(3):259–267, 2000.

[201] M. A. Gondal, A. Hameed, Z. H. Yamani, and A. Arfaj. Photocatalytic transformation of methane into methanol under UV laser irradiation over WO$_3$, TiO$_2$ and NiO catalysts. *Chemical Physics Letters*, 392(4-6):372–377, 2004.

[202] Charles E. Taylor. Methane conversion via photocatalytic reactions. *Catalysis Today*, 84(1-2):9–15, 2003.